LA-UR- 94-2627

C.1

Title:

ZONE REFINING OF PLUTONIUM METAL

Author(s):

Michael S. Blau

Submitted to:

University of Idaho for the Partial Fulfillment of the Requirements for the Degree of Master of Science with a Major in Metallurgical Engineering in the College of Mines and Earth Resources.

Los Alamos
NATIONAL LABORATORY

Form No. 836 R5
ST 2629 10/91

ZONE REFINING OF PLUTONIUM METAL

A THESIS

Presented in Partial Fulfillment of the Requirements for the

Degree of Master of Science

with a

Major in Metallurgical Engineering

in the

College of Mines and Earth Resources

University of Idaho

by

Michael S. Blau

August 1994

Major Professors: Gene E. Bobeck and J. David Olivas

AUTHORIZATION TO SUBMIT

THESIS

This thesis of Michael Steven Blau, submitted for the degree of Master of Science with a major in Metallurgical Engineering and titled "Zone Refining of Plutonium Metal," has been reviewed in final form and approved, as indicated by the signatures and dates given below. Permission is now granted to submit final copies to the college of Graduate Studies for approval.

First Major Professor____________________________Date____________
Gene E. Bobeck

Second Major Professor____________________________Date____________
J. David Olivas

Committee Members____________________________Date____________
Sarit Bhaduri

____________________________Date____________
Dennis R. Horn

Department
Administrator ____________________________Date____________
Gene E. Bobeck

College Dean ____________________________Date____________
Robert W. Bartlett

Final Approval and Acceptance by the College of Graduate Studies

____________________________Date____________
Jean'ne M. Shreeve

ABSTRACT OF THE THESIS

The objective of this experiment was to demonstrate the possibility of developing a plutonium metal zone refining process. Thus, the main objective of this paper was to determine whether passing molten zones along a plutonium metal rod in one direction would cause the impurities gallium, aluminum, americium, cobalt, copper, chromium, iron, nickel, neptunium, and uranium to move along the rod. Minor objectives of this experiment were to observe the distribution of gallium behavior during the zone refining process with and without other elements present in plutonium metal, and an examination of the effects of the number of passes, the molten zone speed, and the power settings.

The zone refining process was applied to plutonium metal containing known amounts of impurities. The distribution of these impurities was determined by chemical and x-ray fluorescence analyses. Rod specimens of plutonium metal were melted into and contained in tantalum boats. Each boat was passed horizontally through a three-turn , high-frequency coil in such a manner as to cause a narrow molten zone to pass through the plutonium metal rod 10 times. The impurity elements cobalt, chromium, iron, nickel, neptunium, and uranium were found to move in the same direction as the molten zone as predicted by their respective binary phase diagrams. The elements aluminum, americium, and gallium moved in the opposite direction of the molten zone as predicted by their respective binary phase diagrams. During this experiment it was discovered that as the impurity alloy was zone refined, δ-phase plutonium metal crystals were produced.

The first few zone refining passes were more effective than each later pass because an oxide layer formed on the rod surface. There was no clear evidence of better impurity movement at the slower zone refining speed. Also, constant or variable coil power appeared to have no effect on impurity movement during a single run (10 passes). This experiment was the first step to developing a zone refining process for plutonium metal.

ACKNOWLEDGMENTS

I would like to take this opportunity to express my deep appreciation to Gene E. Bobeck and J. David Olivas for serving as my advisors.

I would like to thank Sarit Bhaduri and Dennis R. Horn for serving on my committee. I would also like to thank Fred W. Schonfeld, Raymond E. Tate, Carol Richter, and George Biggs for reviewing this thesis.

The technical expertise, generous support, and the valuable time of Larry Vaughan on the induction heating used in this experiment made the completion of this paper possible. I would also like to thank Robert Madeira of Fluxtrol Manufacturing who designed and built the induction coil. Also Joe Tubb is gratefully acknowledged for design and drafting of zone refiner.

Others who contributed significantly to this work were Floyd Rodriquez , Daniel Martinez, and Gerald Lucero for much of the hands-on work for this experiment; Pat Montoyta for machining of x-ray fluorescence samples; John Scnover, George Havrilla, and William Hutchinson for all the plutonium metal analysis work; Ramiro Pereyra for the plutonium metallographic work; Jose Archuleta for x-ray analyses; and Tom Bement for help with statistics.

I want to give a very special thanks to my group leader, Michael F. Stevens, who made it possible for me to attend graduate school at University of Idaho.

TABLE OF CONTENTS

LIST OF TABLES

LIST OF FIGURES

CHAPTER 1

INTRODUCTION

About a half a century ago in 1941 A. C. Wahl, J. W. Kennedy and G. T. Seaborg succeeded in oxidizing a minute quantity of a new synthetic element, element 94, which was later named plutonium. Not one of the elements discovered during the last century appeared so surprising as plutonium, which was the first "artificial" element discovered by man, although it was later determined that minute amounts of plutonium do exist in nature. Plutonium was the second transuranium element of the actinide series to be discovered. Since its discovery and its dramatic emergence at Nagasaki, plutonium has altered the course of history, changed the concepts and consequences of war, and paradoxically has become a powerful instrument for peace (1).

Plutonium is a unique metal in that there are at least six equilibrium allotropes (the phases: alpha, beta, gamma, delta, delta-prime, and epsilon), which range in crystallographic structure from complex monoclinic at low temperatures to a simple body-centered-cubic structure just below the melting point. The complexity of plutonium is further illustrated by the fact that many of its physical properties do not vary with temperature in usual ways. For example, plutonium metal has a low melting point of 640 ^{o}C, but a very high boiling point of approximately 3240 ^{o}C when compared to most other metals (1).

The presence of impurities in plutonium is known to influence a number of its physical properties. When beads of plutonium were first produced in 1943 by micrometallurgical techniques at the University of Chicago, it was observed that some beads were malleable and had a density of about 16 g/cm^3, while other beads were brittle and had a density closer to 20 g/cm^3. It was later determined that this apparent discrepancy was the result of impurity elements stabilizing one of the lower density allotropes of plutonium (2). At the present time, many of the basic properties of plutonium are not accurately known because of the inability to produce even a small amount of plutonium metal of extremely high purity. Perhaps a zone refining technique might be capable of producing small amounts of high purity plutonium metal.

Zone refining is a well-proven technology used by the electronics industry to produce highly purified silicon and germanium. The technique for producing ultra-high purity materials has been greatly improved in the past thirty years, based upon the concept of zone melting processes conceived by W. G. Pfann (3). The use of zone refining has made possible the production of some extremely high purity materials. For example, during zone refining of the elements silicon and germanium, the spectacular results were that most impurity elements were reduced to less than 1 in 10^{10} (one part in a ten billion) (3).

The zone refining process is related to a fact that has been known to metallurgists for many years, i.e., the segregation found in alloy castings. Generally, constitutional segregation is considered a troublesome problem that foundrymen have to contend with, rather than a useful tool. Pfann, however, visualized a method of using segregation to move alloying elements about within a rod. The effectiveness of zone refining in reducing the concentration of unwanted impurities depends most importantly upon the way in which the impurity redistributes itself in the solvent during the melting and solidification processes. The zone refining process involves casting a rod of the substance to be purified and then passing a molten zone serially through the rod in one direction. Impurities travel with, or opposite to, the direction of motion of the zones, depending on whether they lower or raise the melting point of the rod metal, respectively. They tend to become concentrated in the ends of the rod, thereby purifying the remainder. The degree of separation (redistribution/purification) approaches a limit as the number of passes becomes infinite (3).

Zone refining of plutonium was investigated in the late 1950s at the Los Alamos National Laboratory (2). That investigation showed the elements cobalt, chromium, iron, manganese, nickel, silicon, and aluminum moved in the directions predicted from the respective binary constitutional diagrams, but the elements beryllium, bismuth, boron, calcium, copper, lanthanum, lead, lithium, magnesium, silver, sodium, tin, and zinc did not move.

However, the two most common elements in plutonium are gallium and americium, were not present in this early study. Thus, it is not known whether these elements are affected by zone melting. The binary phase diagrams for these elements with plutonium indicate that gallium and americium should travel opposite to the motion of the molten zone. Additionally, some of the elements that were found not to be affected by zone melting may evaporate in the high-vacuum environment that should be used for zone refining of plutonium.

The purpose of this study is to investigate the possibility of developing an effective refining process to purify plutonium metal. If zone refining of plutonium metal can be carried out successfully, it may be possible to produce enough plutonium of very high purity to perform fundamental property experiments on plutonium metal that have not yet been done. This is because current methods for purifying plutonium do not produce sufficiently high purity plutonium metal.

One of the most desirable experiments that depends upon a source of high purity plutonium metal is growing large single crystals of gallium-stabilized delta-phase plutonium. This might be essentially a solid-state zone heating process. There have been many attempts at growing single crystals of plutonium, but to date the best result has been to grow large plutonium grains. This is because of crystal structure changes that occur when plutonium metal cools from the molten state to room temperature. With a plutonium alloy of one weight percent gallium, the number of structure changes drops from six down to three, with the delta phase being stable from room temperature to about 550^{O}C. Therefore, for this study to be considered complete, it is desirable to better understand the behavior of gallium in the zone melting process.

CHAPTER 2

THE THEORY OF ZONE REFINING

2.1. The Theory of Solidification

Zone refining is based on the principle that a difference in solute concentration exists between the solid at the liquid-solid interface at the solidifying end of the molten zone and the bulk liquid. This difference is a consequence of the equilibrium that exists between the liquid and solid phases of a binary system. During solidification, equilibrium can be closely approached between the liquid and solid at the liquid-solid interface. However, most metals do not freeze under equilibrium conditions (3).

As an alloy is cooled from the liquid state, it reaches a point at which a solid begins to form. The solid that forms generally has a different composition than the liquid from which it is freezing. This redistribution of the solute produced by solidification is frequently termed segregation (4).

Alloy solidification can take place under four distinct sets of conditions as discussed below. In practice, case 3 solidification with no diffusion in the solid, partial mixing in the liquid, dominates. (3, 4, 5)

2.1.1. Equilibrium Solidification (Case 1)

Consider a hypothetical alloy indicated by the dot-dash line in the eutectic-type phase diagram shown in Figure 1. The way in which such an alloy solidifies in practice depends in rather a complex way on temperature gradients, cooling rates, and growth rates. The alloy whose composition is X_0 begins to solidify at temperature T_1, if no nucleation barrier interferes, with the formation of a small amount of solid of composition X_S or KX_0. It is useful to define the equilibrium distribution coefficient K as the ratio of the composition of the solid to that of the liquid at any temperature of interest:

$$K = \frac{X[solid]}{X[liquid]} = \frac{X_s}{X_o} \tag{1}$$

with values of X_S and X_o taken from the binary phase diagram. The equilibrium distribution coefficient $K < 1$ for systems in which the solute element lowers the melting point such as in Figure 1 and $K > 1$ for systems in which the solute element raises the melting point of the alloy. As the temperature is lowered more solid forms. If cooling is slow enough to allow extensive solid-state diffusion, the solid and liquid will each be homogeneous and in equilibrium with each other with compositions following the solidus and liquidus lines, as in Figure 1. The relative amounts of solid and liquid at any temperature are given by the inverse lever rule. At temperature T_2, the last drop of liquid will have a composition X_o / K and the average composition of the solid will be X_o, the same as that of the original melt (4, 5).

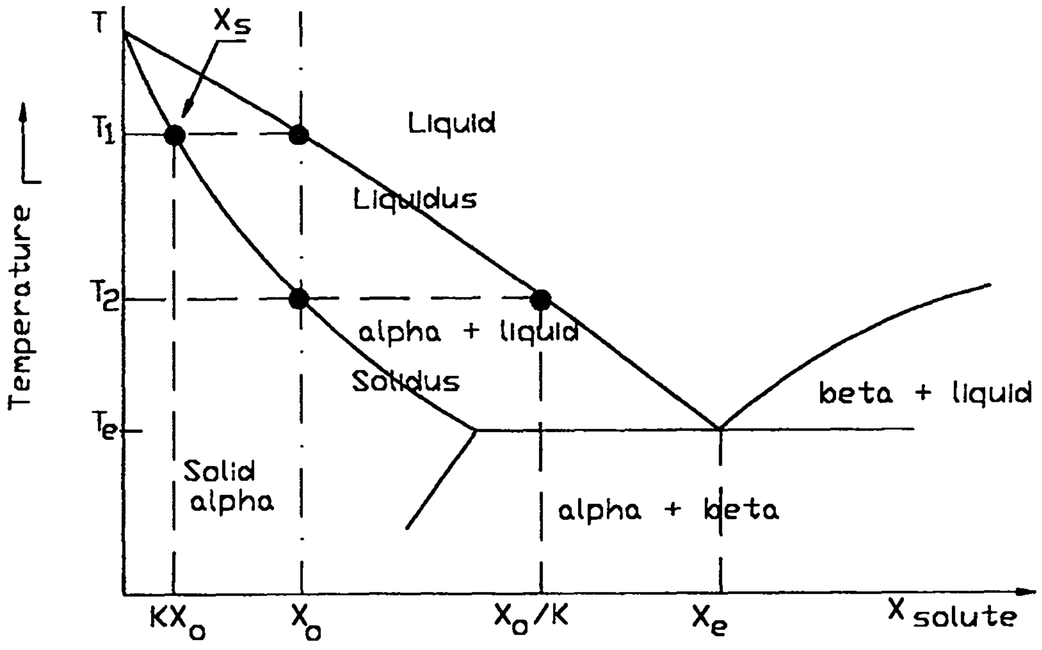

Figure 1. Hypothetical solid-liquid region of a eutectic-type phase diagram.

2.1.2. Solidification with No Diffusion in Solid and Perfect Mixing in Liquid, (Case 2)

If the rate of cooling is rapid enough, no diffusion will take place in the solid. Assuming that the liquid is kept homogeneous during solidification by efficient stirring, then, as in case 1, the first solid to appear when T_1 is reached will have a composition X_s, Figure 2. This first solid contains less solute than the liquid from which it forms. The solute atoms are rejected into the liquid and increase solute concentration above X_o. The temperature must therefore decrease below T_1 before further solidification can occur, and the second layer of solid will be slightly richer in solute than the first. As this sequence of events continues, the liquid becomes progressively richer in solute and solidification takes place at progressively lower temperatures. However, since there is no diffusion in the solid, the separate layers of solid retain their original compositions. Thus, the mean composition of the solid (X_{sm}) is always lower than the composition at the solid/liquid interface, as shown by the marked line that starts at X_s in Figure 2. It follows that the liquid can become much richer in solute than X_o/K and it may even reach a eutectic composition, X_e. Solidification will thus tend to terminate close to T_e with the formation of a eutectic structure. This case begins to show the principle of purifying a metal (removing the solute) by zone refining (5).

2.1.3. Solidification with No Diffusion in Solid, Partial Mixing in Liquid, (Case 3)

As solidification occurs with partial mixing in the liquid, by far the most common case, the liquid is no longer uniform. Again consider the molten alloy in the hypothetical phase diagram shown in Figure 1. When alloy X_o begins to solidify at T_1, the advancing solid rejects solute more rapidly than can mix into the main body of liquid, and hence a layer of liquid enriched with solute builds up ahead of the interface. The solute concentration in this layer, rather than that in the main body of liquid, determines the solute concentration of solid forming at the liquid-solid interface. The solute concentration in the bulk liquid, X_l , can be described by an effective distribution coefficient K_e equal to the ratio X_s/X_l (3).

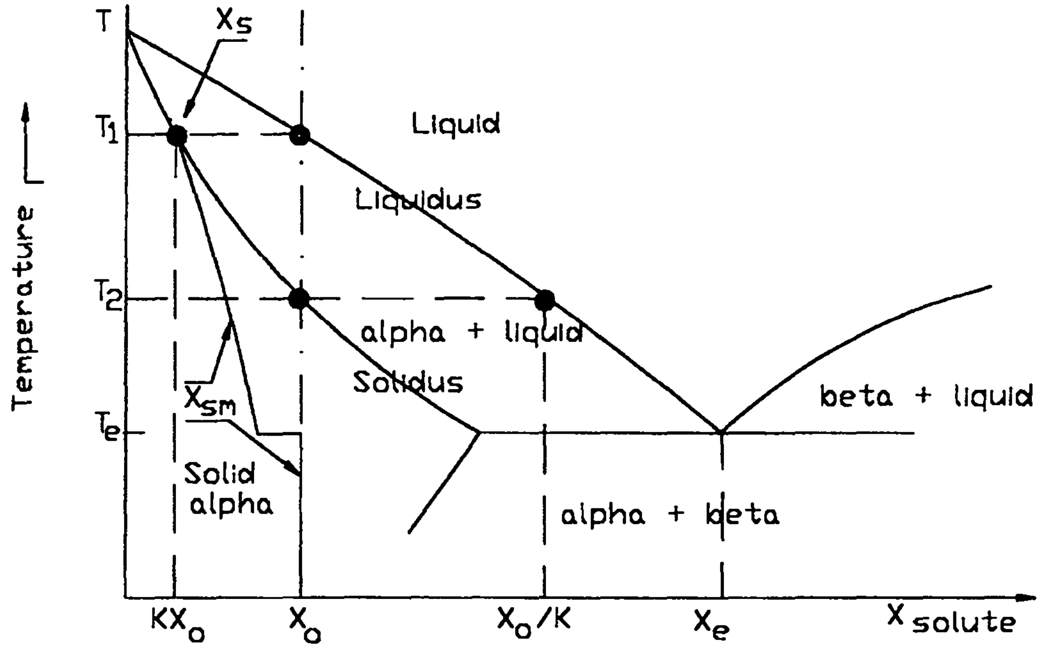

Figure 2. Hypothetical solid-liquid region of a eutectic-type phase diagram.

2.1.4. Solidification with No Diffusion in Solid, Diffusion in Liquid, No Stirring, (Case 4)

If there is no stirring or convection in the liquid phase, the solute rejected from the solid will only be transported away by diffusion. Cases of completely diffusion-dominated transport in the liquid are rare in practice, for metals at least. Hence, there will be a rapid build-up of solute ahead of the solid and a correspondingly rapid increase in the composition of the solid formed. If solidification is made to occur at a constant rate, it can be shown that a steady state is finally obtained when the solid-liquid interface temperature reaches T_2 in Figure 1. The liquid adjacent to the solid then has a composition X_o/K and the solid forms with the bulk composition X_o (3, 5).

2.1.5. Segregation During Normal Freezing

No segregation remains after equilibrium solidification because sufficient time is allowed for complete diffusion in the solid. In practice, solidification occurs fast enough that there is usually little or no diffusion in the solid and thus segregation results. The degree of segregation will depend on transport conditions in the liquid, as in cases 2, 3, and 4 discussed above. Since the equilibrium distribution coefficient K is the extreme value of the effective distribution coefficient K_e for a given system, freezing conditions for which the K_e is equal to K are those corresponding to maximum segregation.

A good approximation for the effective distribution coefficient K_e, that can be calculated from the following equation:

$$K_e = 2C_o/C_{max} \quad \text{if } K<1 \tag{2a}$$

or

$$K_e = 2C_o/C_{min} \quad \text{if } K>1 \tag{2b}$$

where C_o is the macroscopic composition of the material and C_{max} or C_{min} is either the maximum or minimum microscopic composition across the grains in the material. The C_{max} or C_{min} values are obtained using an electron microprobe. This equation is based on the theory that the solute is being rejected by C_o/K (liquidus line in Figure 1), but there usually are two major grain walls (dendrite-type structures), thus the need for a factor of two in the above equation. This theory is derived from work done by Self at the Colorado School of Mines (6).

2.2. The Theory of Single-Pass Zone Refining

Consider a rod of length L of the hypothetical alloy whose composition X_o is shown in Figure 1 and cause a molten zone of length l to traverse the rod slowly, as shown in Figure 3. Since $K < 1$, passing the zone through the ingot distributes the solute as shown in Figure 4. The curve has three distinct regions: an initial region starts with composition KX_o and ends with composition X_o at the start of the central region; the central region ends at the start

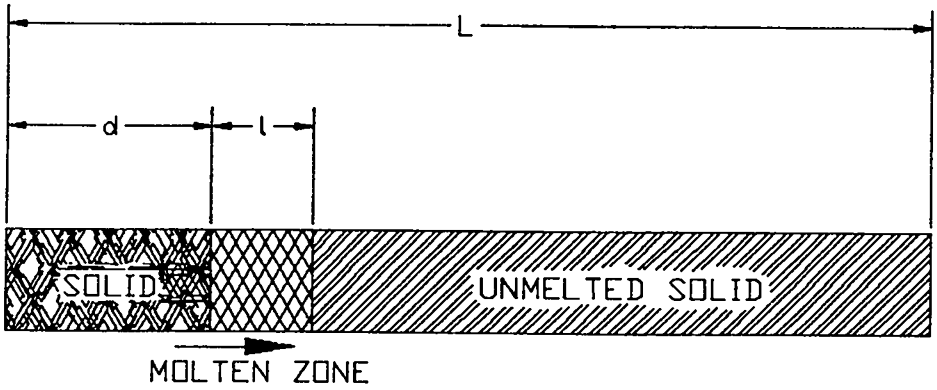

Figure 3. Molten zone traversing a rod.

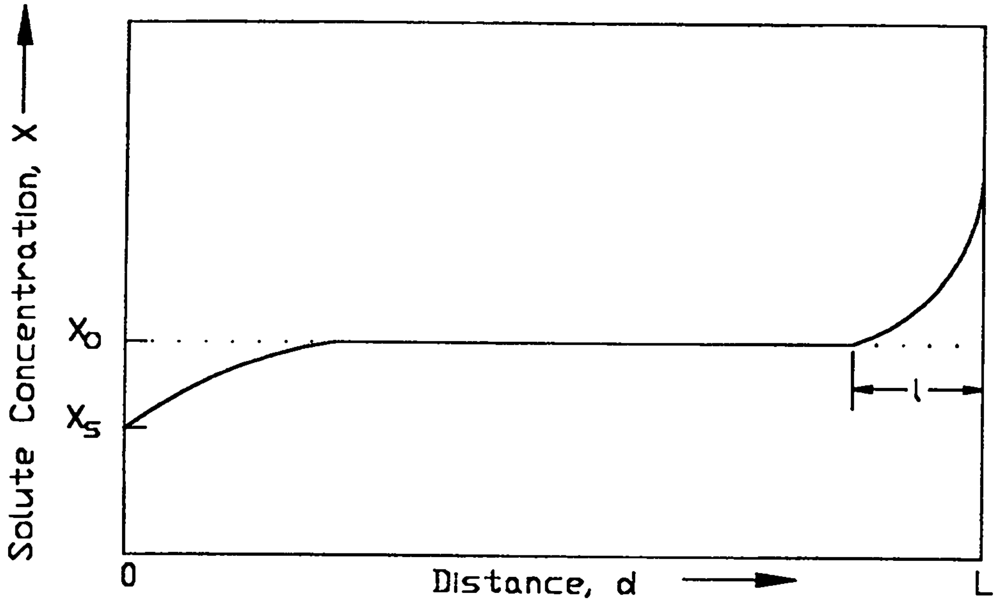

Figure 4. Variation of composition along a rod produced by zone melting after one pass.

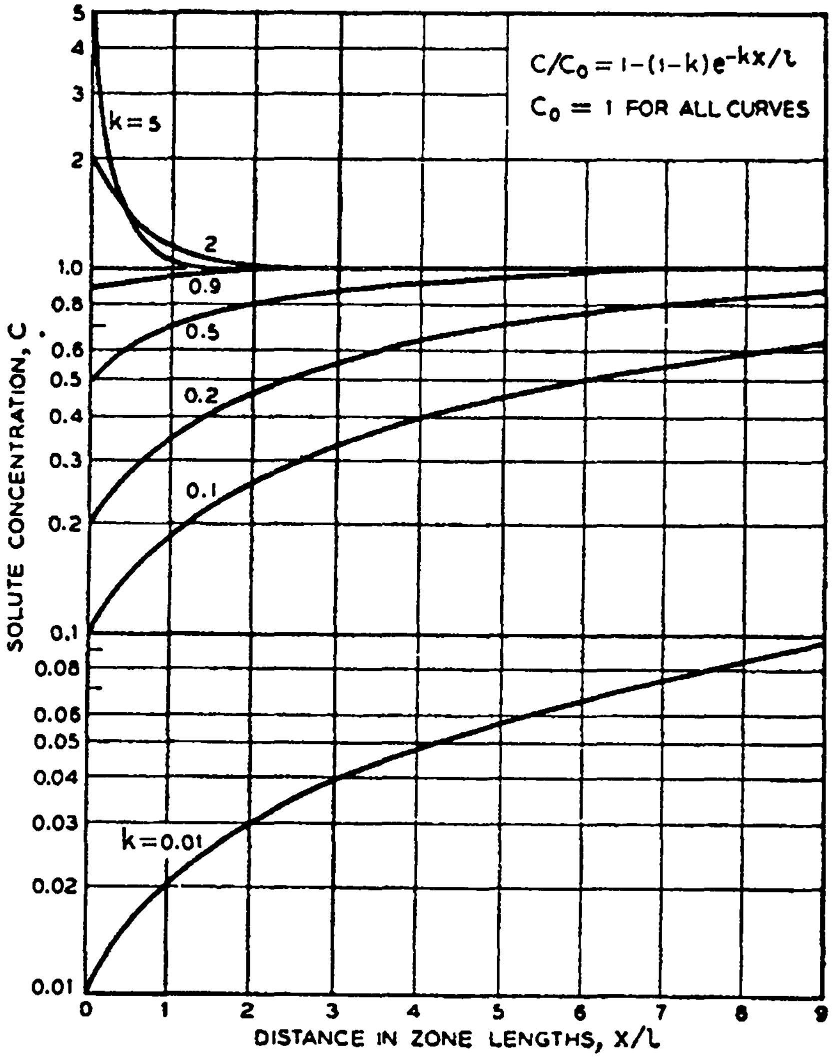

Figure 5. Curves for single-pass zone refining showing solute concentration in the solid versus distance in zone lengths from beginning of charge, for various values of K; taken from Pfann (3).

of the end region when the composition begins to increase above Xo; the end region is a short region of length *l* (molten zone width) where the solute has concentrated. The area below the X_0 line (Figure 4) for the initial region must equal the area above the X_0 line for the end region in order for mass to be conserved. After one pass of the zone through the rod, the concentration, X, at a distance, d, from the end at which the zone began, can be shown to be given by:

$$\frac{X}{X_o} = 1 - (1 - K)e^{-Kd/l} \tag{3}$$

The equation is valid in all but the last zone length. See Figure 5 for the curves for single-pass zone refining showing solute concentration in the solid versus distance in zone lengths from beginning of charge, for various distribution coefficients ranging from 0.01 to 5 (3).

2.3. Multiple Pass Zone Refining

The merits of zone refining become evident when multiple passes of a molten zone are made along a rod. During a second pass through the rod, the first solid to form is further depleted of solute, enriching the liquid in solute. In each successive pass, the first solid to form is increasingly depleted of solute and the total amount of solid depleted in solute also increases. The mathematics of multiple zone refining passes are beyond the scope of this paper but Pfann shows an good example of multiple pass results (Figure 6) (3). Upon examination of Figure 6., it must be noted that the distribution coefficient used in the figure (K = 0.9524) is considered poor for zone refining as can be seen in Figure 5.

2.4. Molten Zone Heating

The problem of producing and maintaining a molten zone amounts to establishing a temperature in the zone that is above the melting point of the solid, and establishing on either side of the zone a cool region whose temperature is below the melting point of the solid. If the zone length is to remain constant, this temperature profile must be held correspondingly constant (3).

The problem of moving a zone amounts to moving the heat source and heat sink, i. e., furnishing heat of fusion at the melting interface and removing heat of fusion at the freezing interface. Even at the low travel rates used in zone refining, the heats of fusion and freezing can markedly change the temperature profile when an established zone begins its travel (3).

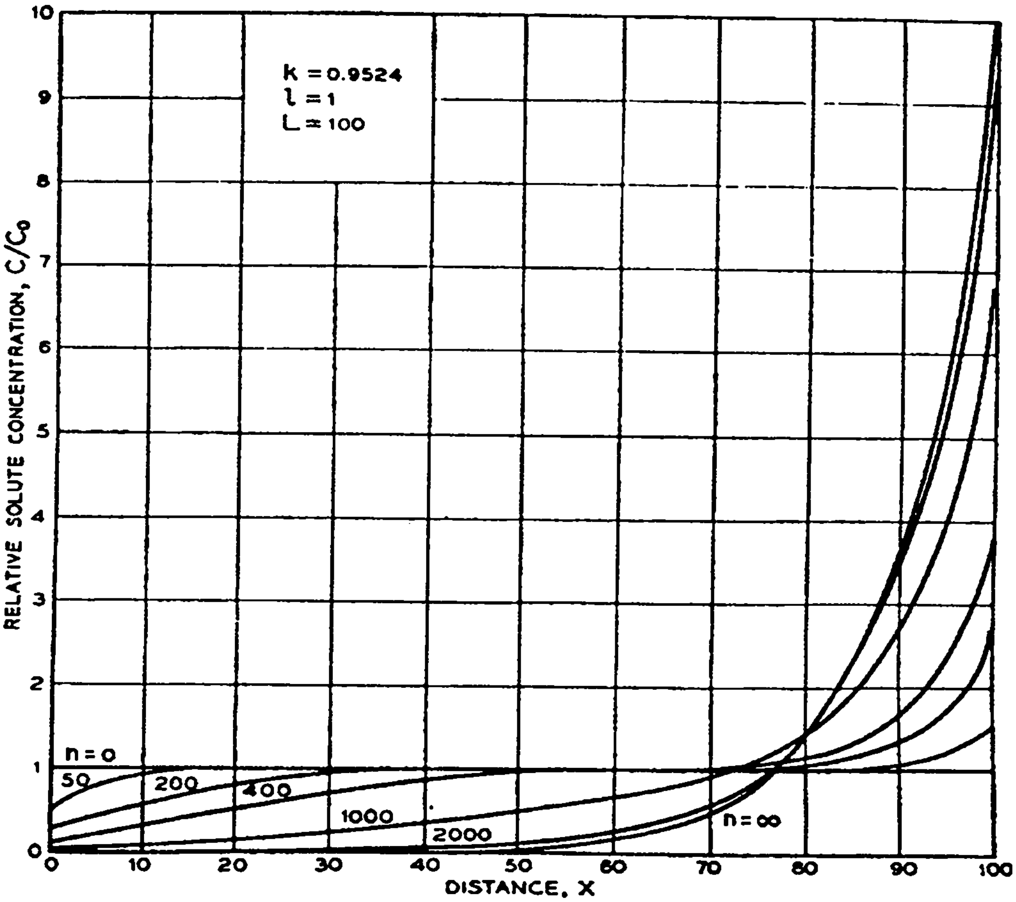

Figure 6. Relative solute concentration C/C_0 versus distance x with number of passes n as a parameter for K = 0.9524, l = 1, and L = 100; taken from Pfann (3).

2.4.1. Molten Zone Heating Techniques

Many techniques can be used for heating the molten zone, from the simple method of resistance heating to the more complex laser heating methods. An ideal heating method that has many advantages for zone refining is induction heating. Induction heating provides a means for precise heating of electrically conducting objects that is clean, fast, and reproducible. The heat can be generated within the charge itself, thus reducing contamination from the container material. The eddy currents produced by induction provide some degree of stirring in the liquid depending on the frequency used. Usually the molten zone length is shorter for the induction technique than that of other techniques such as resistance or conduction heating.

2.4.2. Induction Heating

The basis for induction heating lies in the ability to induce electric currents in electrical conductors. Resistance to the electric currents generated lead to heating of the conductor. Associated with the current, I, is a voltage drop, V, which, for a pure resistance, R, is given by Ohm's law (V = IR). When a drop in potential occurs, electrical energy is converted into thermal energy, (watts, W), ($W = VI = I^2R$), or heat (7).

In designing an induction heating system, the major consideration is the power supply frequency. Induction heating is efficient if certain basic relationships between the frequency of the magnetic field and the properties of the conductor produce a suitable degree of skin effect. Skin effect is the phenomenon by which the eddy currents flowing in a cylindrical conductor tend to be most intense at the surface, while currents at the center are nearly zero. There is no induction heating unless the power developed near the surface is larger than the power induced near the center of the conductor (7, 8).

The mathematics needed to explain the skin effect are beyond the scope of this discussion, but one of the most important benefits obtained from the solution of the differential equation describing induction heating is that it gives an "effective" depth of the current-carrying layers. This depth, which is known as the "skin depth," d, depends on frequency of the alternating current field and on the electrical resistivity and relative magnetic permeability of the workpiece. The skin depth is very useful in gauging the suitability of various materials for induction heating. The definition of d is:

$$d = 3160\sqrt{\frac{\rho}{\mu f}} \qquad (4)$$

where d is the skin depth, in inches; ρ is the resistivity of the workpiece, in ohm-inches; μ is the relative magnetic permeability of the workpiece (dimensionless); and f is the frequency of the coil, in hertz. The skin depth is defined as the distance from the surface of a given material at which the induced field strengths are reduced to 37% of their surface values. Ideally, for melting operations the skin depth should be three to four times the diameter of the workpiece. When using the skin depth concept for zone refining applications, the lower the frequency, the more stirring of the molten zone. The more stirring in the molten zone, the higher degree of purification per molten zone pass (7, 8).

CHAPTER 3

REVIEW OF THE LITERATURE

3.1. Zone Refining of Plutonium

Modest success in the zone refining of plutonium was reported by Tate and Anderson in 1958 (2). They made zone refining runs on five different plutonium rods (10 passes each) at five different speeds (0.23-1.3 in/h). The starting plutonium contained impurities averaging less than 100 ppm per impurity. They used a 450,000 Hz power supply to run a single-turn coil. This induction setup produced a large molten zone compared to rod diameter with little stirring in the molten zone. The results showed that the impurities cobalt, chromium, iron, manganese, nickel, silicon, and aluminum were moved in the direction as predicted by the respective binary constitutional phase diagrams. They also confirmed that the slower the molten zone speed, the greater the segregation . However, in most cases, a speed of 1.3 in/h had poor separation, a speed of 0.9 in/h had better separation, and slower speeds down to 0.23 in/h did not improve the separation. The elements beryllium, bismuth, boron, calcium, copper, lanthanum, lead, lithium, magnesium, silver, sodium, tin, and zinc did not appear to move. Three deficiencies with this study were that all five rods used had different compositions, the impurity levels were very low making it difficult to measure element movement, and the induction frequency was so high that there was very little induction stirring in the molten zone. Also, analytical chemistry techniques for plutonium were not as well developed in the 1950s as they are now.

3.2. Zone Refining of Similar Metals

As already discussed, plutonium is a unique metal. The closest naturally available metal to plutonium is uranium. The most obvious difference between uranium and plutonium is in the melting points, 1132 ^{o}C for uranium compared to 640 ^{o}C for plutonium. Modest success has been documented in zone refining of uranium metal. Both natural impurities and fission products have been segregated. There have been several studies on zone refining of uranium using many different techniques and with starting materials containing impurities ranging from 50 ppm to over 1000 ppm. In all cases, there was some degree of uranium purification (3, 9, 10, 11).

One of the best examples of uranium zone refining uranium with moderate impurity levels (1000 ppm) was by Bieber, Schreyer, and Williams(9). Using an electron beam zone refining technique, they purified uranium from 1000 ppm to about 50 ppm in 6 passes using different speeds (0.75-5.0 in/h). However, they determined that the oxide layer formed during each molten zone pass had to be removed before the next pass or poor zone refining resulted.

The most current uranium zone refining work is that of Suzuki, Shikama, and Ochiai (13). Using an induction zone refining technique under high vacuum, they have been able to obtain uranium purity of 99.99 weight percent (100 ppm total impurity content).

3.3. Plutonium Phase Diagrams

For this study, ten elements which commonly appear as impurities in plutonium metal were selected. These are gallium, aluminum, americium, cobalt, copper, chromium, iron, nickel, neptunium, and uranium. By examining their binary phase diagrams, predictions can be made whether each can be removed from plutonium metal by zone refining.

The plutonium binary constitutional diagram (the latest available version) for each of the ten selected impurities is presented in Figures 7a through j. For each element of interest, regions of each binary phase diagram were enlarged to estimate the equilibrium distribution coefficient at the appropriate concentration. This was accomplished by first drawing in the X_O concentration for each impurity on the enlarged plutonium-rich end of each phase diagram (10,000 ppm by weight for gallium and 1000 ppm by weight for the other nine elements), then drawing a line perpendicular to the X_O line at the intersection of the liquidus line (this line extends to the left if $K < 1$ and to the right if $K > 1$) to determine the point KX_O as is shown in Figure 1 (where K was greater than one in this case). Based on the phase diagrams, predictions were made of impurity (solute) movement direction and how well the impurity would move. It should be mentioned that with some of these systems the predictions made by the phase diagrams are only estimates because of the lack of available information. Because of this, a better estimate of the equilibrium distribution coefficient for plutonium metal impurities is to use the effective distribution coefficient determined by using a electron microprobe as is discussed in section 2.1.5. The effective distribution coefficients of impurities were reported in the cases where the effective distribution coefficients were determined in the Kristofova, Kuchar, and Wozniakova paper (12).

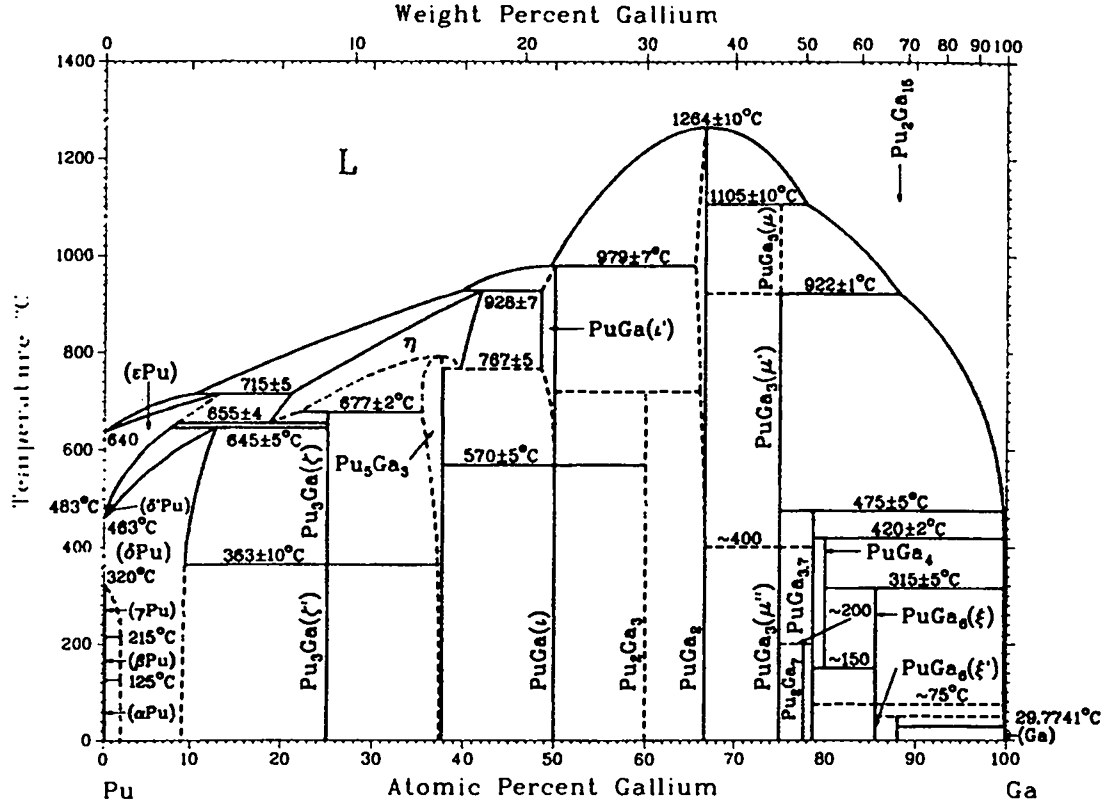

Figure 7a. Plutonium-gallium binary phase diagram; taken from Binary Alloy Phase Diagrams (13).

3.3.1. Plutonium-Gallium Phase Diagram

Figure 7a shows that adding gallium to plutonium raises the melting point of a plutonium-gallium alloy. Consequently, the distribution coefficient should be greater than one and gallium should move in the direction opposite to the molten zone when this alloy is zone refined. The equilibrium distribution coefficient for a plutonium alloy with 10,000 ppm gallium by weight (1 W/o or 3.4 A/o) is 1.4, which should result in a modest gallium segregation during zone refining.

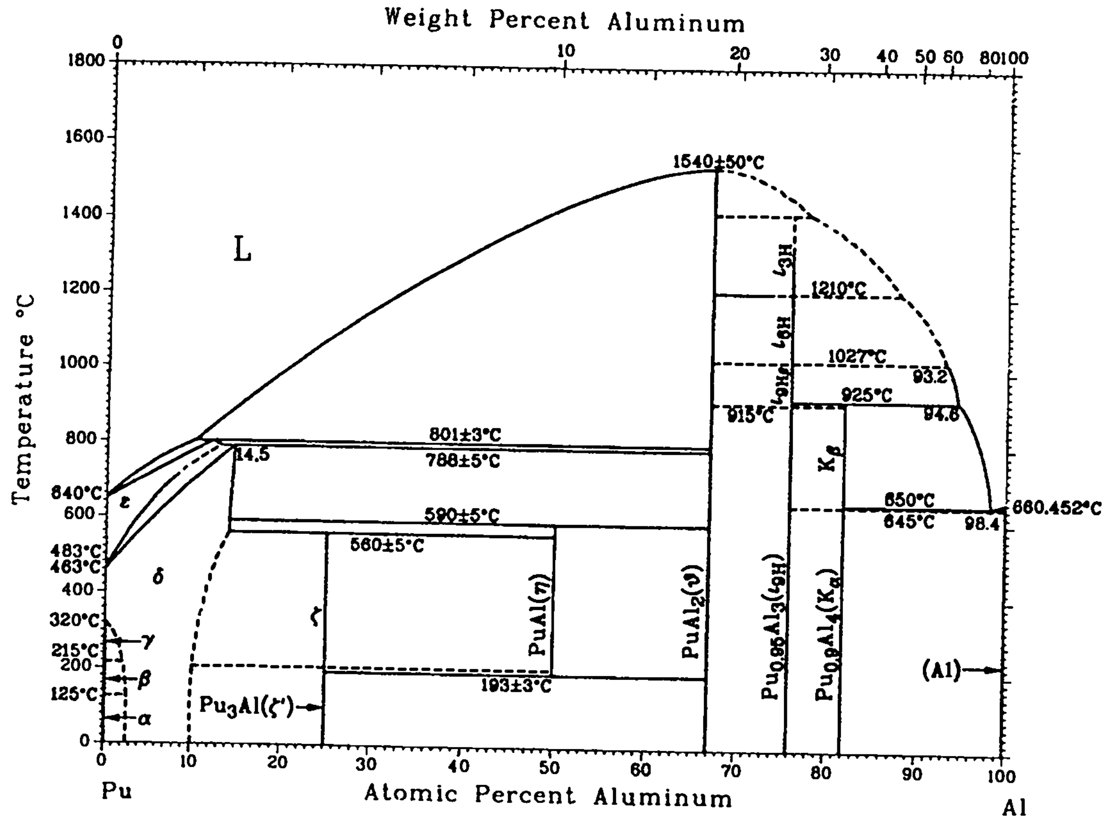

Figure 7b. Plutonium-aluminum binary phase diagram; taken from Binary Alloy Phase Diagrams (13).

3.3.2. Plutonium-Aluminum Phase Diagram

Figure 7b shows that adding aluminum to plutonium raises the melting point of a plutonium-aluminum alloy. Consequently, the distribution coefficient should be greater than one and aluminum should move a direction opposite to the molten zone when this alloy is zone refined. The equilibrium distribution coefficient for a plutonium alloy with 1000 ppm aluminum is approximately 1.4, which should result in a modest aluminum segregation during zone refining.

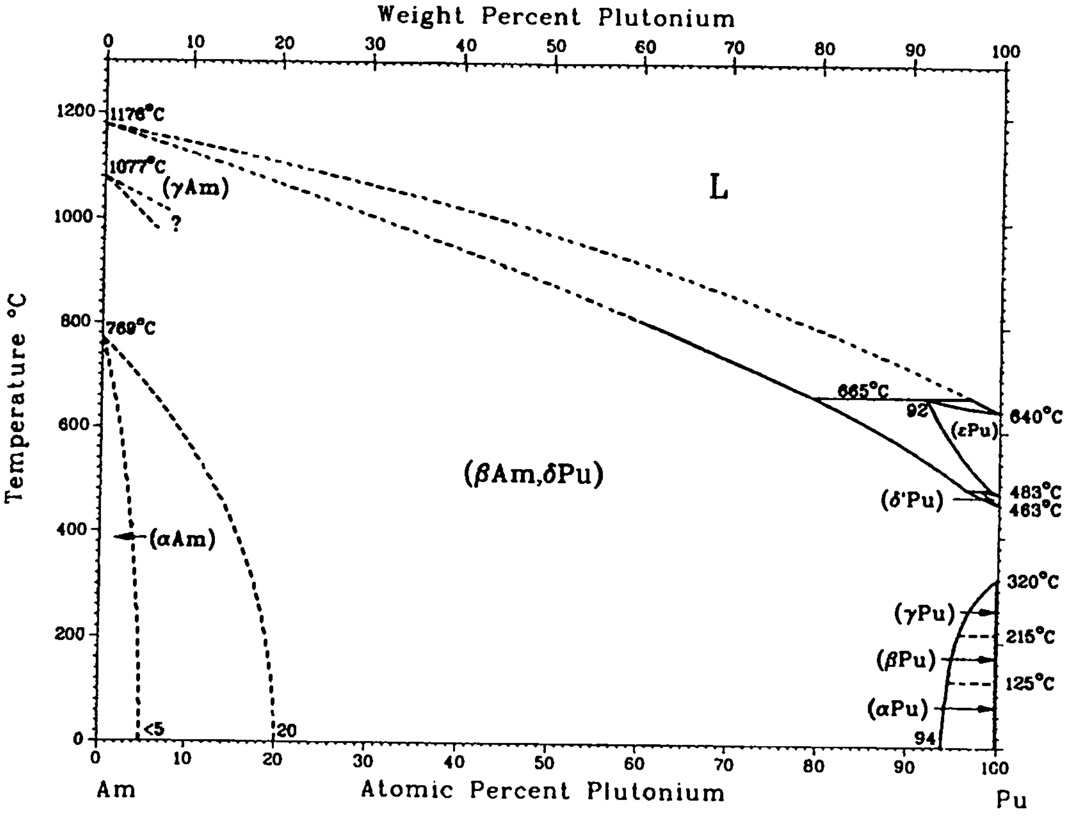

Figure 7c. Plutonium-americium binary phase diagram; taken from Binary Alloy Phase Diagrams (13).

3.3.3. Plutonium-Americium Phase Diagram

Figure 7c shows that adding americium to plutonium raises the melting point of a plutonium-americium alloy. Consequently, the distribution coefficient should be greater than one and americium should move a direction opposite to the molten zone when this alloy is zone refined. The equilibrium distribution coefficient for a plutonium alloy with 1000 ppm americium is approximately 2.7, which should result in a good americium segregation during zone refining.

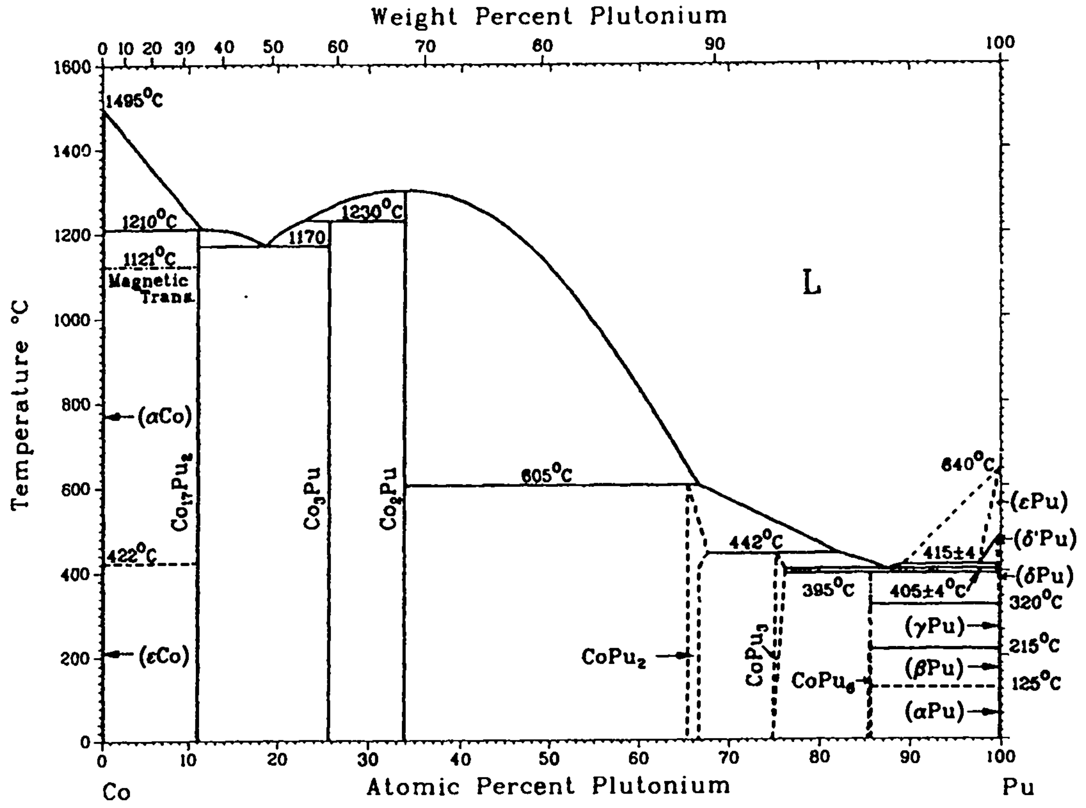

Figure 7d. Plutonium-cobalt binary phase diagram taken; from Binary Alloy Phase Diagrams (13).

3.3.4. Plutonium-Cobalt Phase Diagram

Figure 7d shows that adding cobalt to plutonium lowers the melting point of a plutonium-cobalt alloy. Consequently, the distribution coefficient should be less than one and cobalt should move in the same direction as the molten zone when this alloy is zone refined. The equilibrium distribution coefficient for a plutonium alloy with 1000 ppm cobalt is approximately 0.2, which should result in a high cobalt segregation during zone refining. However, the effective distribution coefficient from Kristofova, Kuchar, and Wozniakova was approximately 0.8 (12).

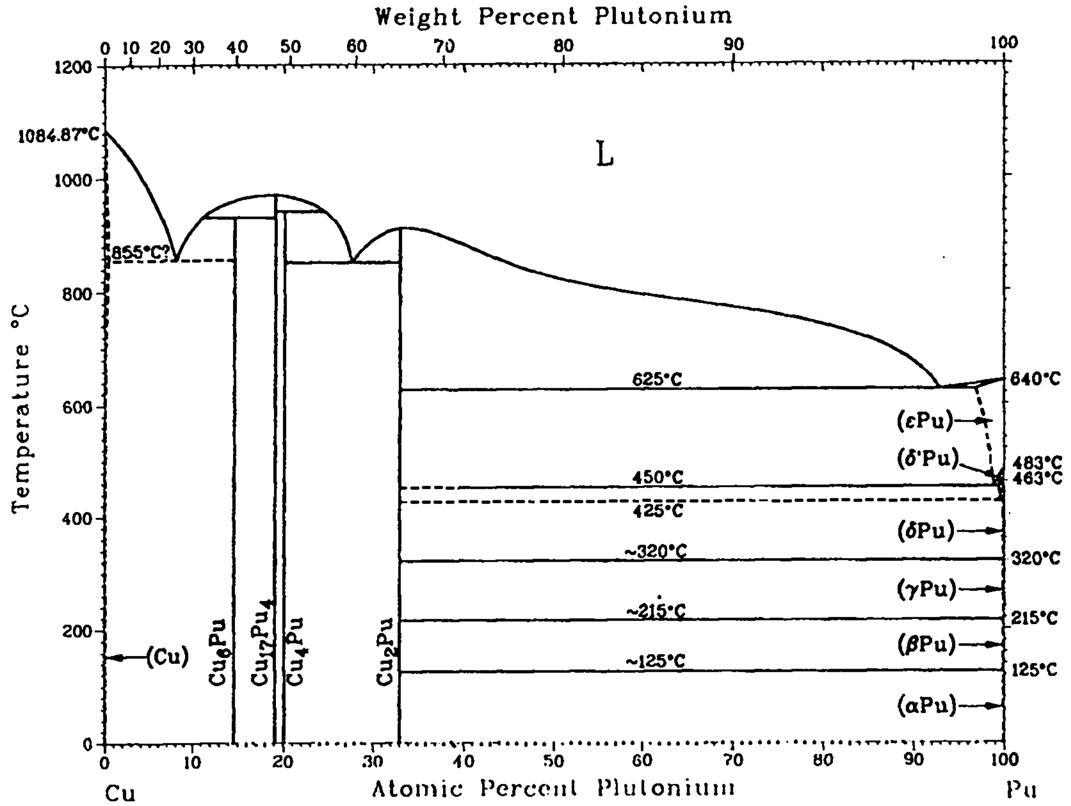

Figure 7e. Plutonium-copper binary phase diagram; taken from Binary Alloy Phase Diagrams (13).

3.3.5. Plutonium-Copper Phase Diagram

Figure 7e shows that adding copper to plutonium lowers the melting point of a plutonium-copper alloy. Consequently, the distribution coefficient should be less than one and copper should move in the same direction as the molten zone when this alloy is zone refined. The equilibrium distribution coefficient for a plutonium alloy with 1000 ppm copper is approximately 0.3, which should result in a great copper segregation during zone refining.

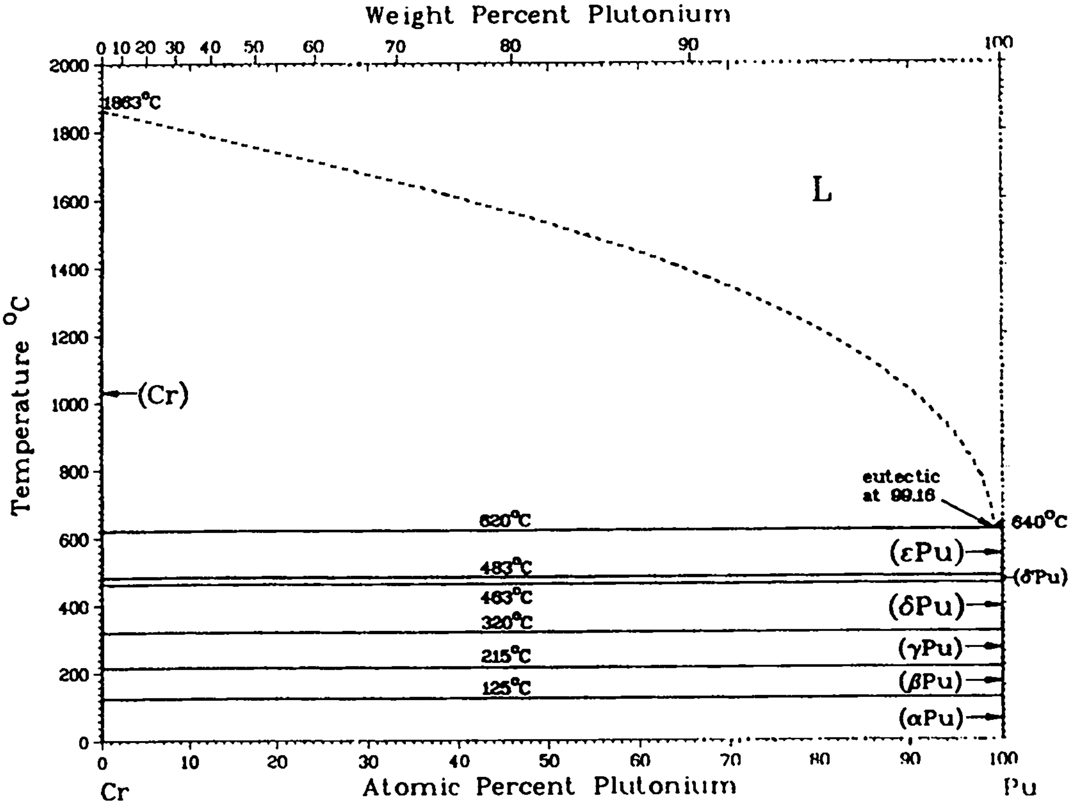

Figure 7f. Plutonium-chromium binary phase diagram taken; from Binary Alloy Phase Diagrams (13).

3.3.6. Plutonium-Chromium Phase Diagram

Figure 7f shows that adding chromium to plutonium lowers the melting point of a plutonium-chromium alloy that is less than 2000 ppm chromium by weight. Consequently, the distribution coefficient should be less than one and chromium should move in the same direction as the molten zone when this alloy is zone refined. The equilibrium distribution coefficient for a plutonium alloy with 1000 ppm chromium is approximately 0.2, which should result in a high chromium segregation during zone refining. The effective distribution coefficient from Kristofova, Kuchar, and Wozniakova was approximately 0.6 (12).

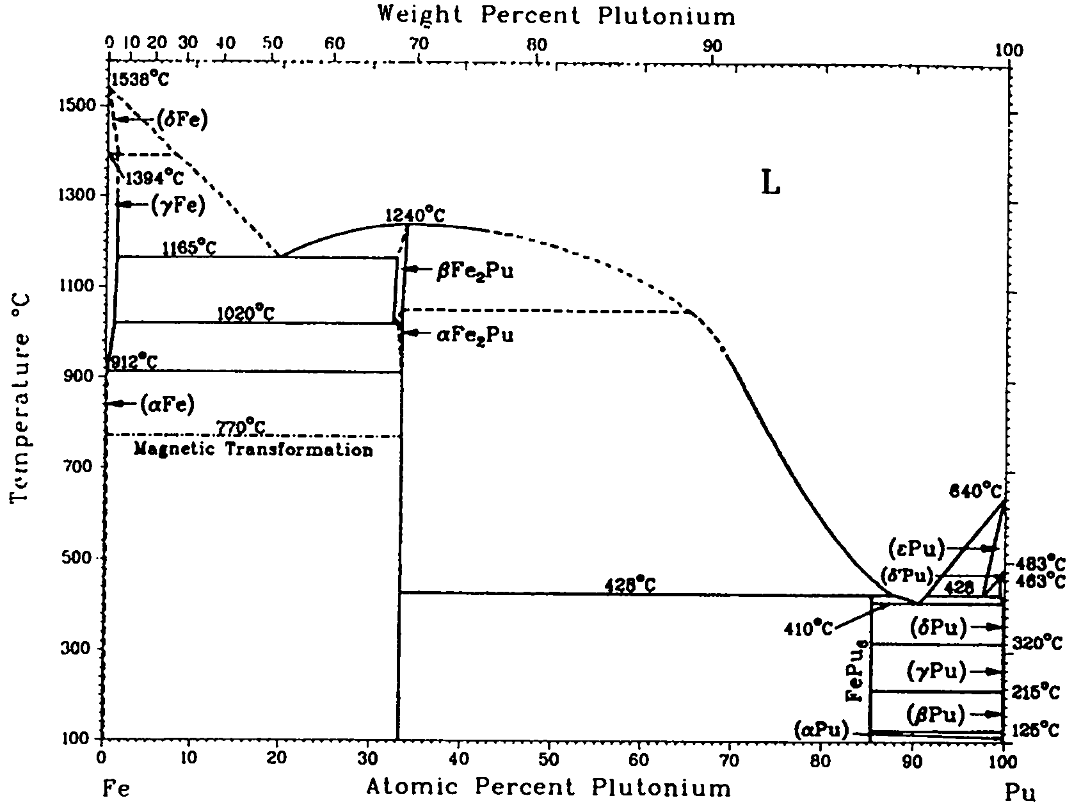

Figure 7g. Plutonium-iron binary phase diagram taken; from Binary Alloy Phase Diagrams (13).

3.3.7. Plutonium-Iron Phase Diagram

Figure 7g shows that adding iron to plutonium lowers the melting point of a plutonium-iron alloy. Consequently, the distribution coefficient should be less than one and iron should move in the same direction as the molten zone when this alloy is zone refined. The equilibrium distribution coefficient for a plutonium alloy with 1000 ppm iron is approximately 0.2, which should result in a high iron segregation during zone refining. The effective distribution coefficient from Kristofova, Kuchar, and Wozniakova was approximately 0.6 (12).

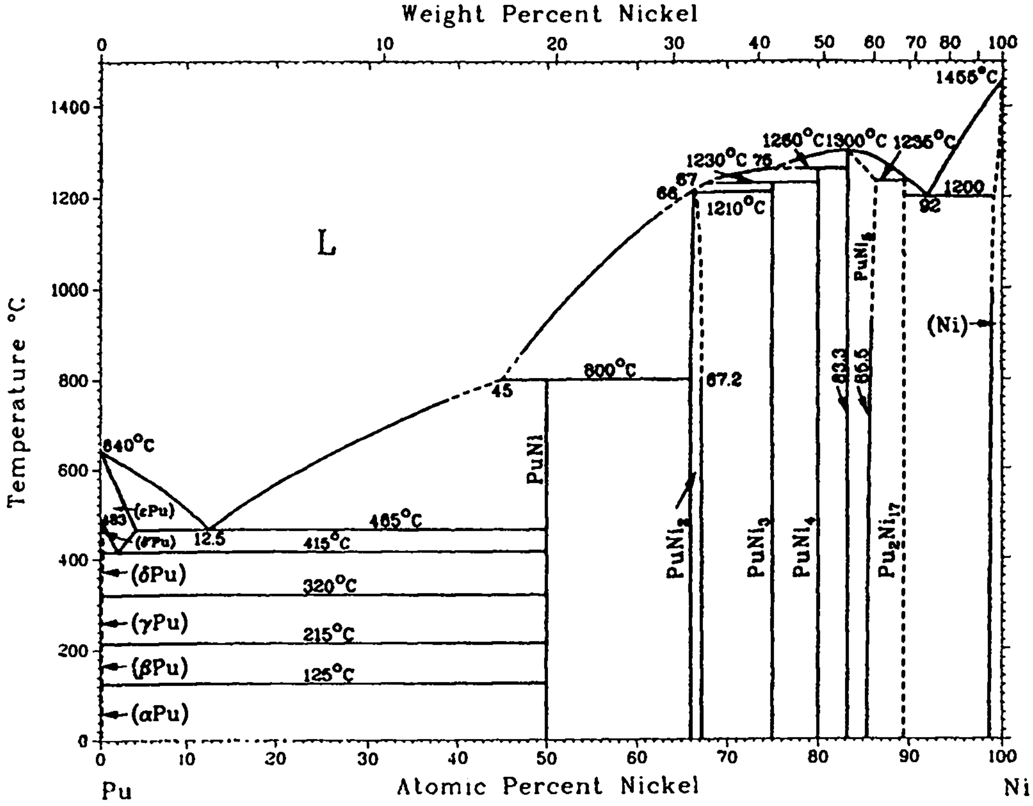

Figure 7h. Plutonium-nickel binary phase diagram taken; from <u>Binary Alloy Phase Diagrams</u> (13).

3.3.8. Plutonium-Nickel Phase Diagram

Figure 7h shows that adding nickel to plutonium lowers the melting point of a plutonium-nickel alloy. Consequently, the distribution coefficient should be less than one and nickel should move in the same direction as the molten zone when this alloy is zone refined. The equilibrium distribution coefficient for a plutonium alloy with 1000 ppm nickel is approximately 0.3, which should result in a high nickel segregation during zone refining. The effective distribution coefficient from Kristofova, Kuchar, and Wozniakova was approximately 0.7 (12).

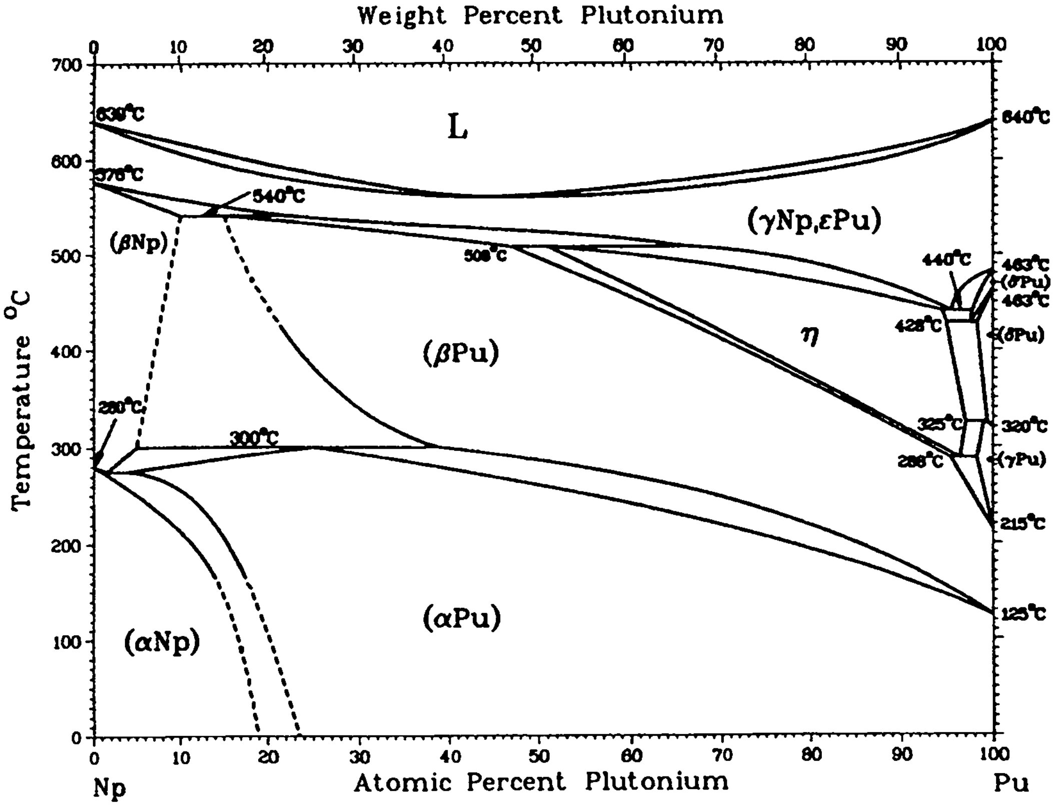

Figure 7i. Plutonium-neptunium binary phase diagram; taken from Binary Alloy Phase Diagrams (13).

3.3.9. Plutonium-Neptunium Phase Diagram

Figure 7i shows that adding neptunium to plutonium lowers the melting point of a plutonium-neptunium alloy. Consequently, the distribution coefficient should be less than one and neptunium should move in the same direction as the molten zone when this alloy is zone refined. The equilibrium distribution coefficient for a plutonium alloy with 1000 ppm neptunium is approximately 0.8, which should result in poor to moderate neptunium segregation during zone refining.

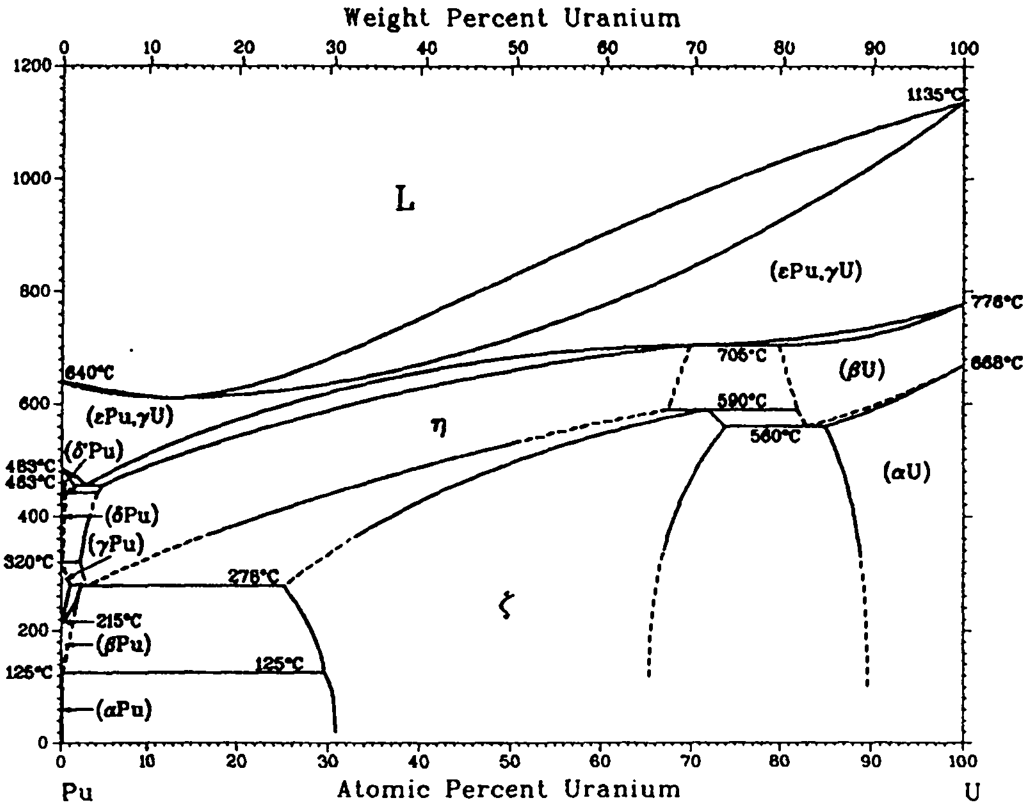

Figure 7j. Plutonium-uranium binary phase diagram; taken from <u>Binary Alloy Phase Diagrams</u> (13).

3.3.10. Plutonium-Uranium Phase Diagram

Figure 7j shows that adding uranium to plutonium lowers the melting point of a plutonium-uranium alloy. Consequently, the distribution coefficient should be less than one and uranium should move in the same direction as the molten zone when this alloy is zone refined. The equilibrium distribution coefficient for a plutonium alloy with 1000 ppm uranium is approximately 0.6, which should result in a moderate uranium segregation during zone refining.

3.4. Special Issues With Plutonium

Many challenges must be faced in order to process plutonium because of its toxicity, reactivity, pyrophoricity, and criticality hazards. Therefore, plutonium experimentation must be conducted inside gloveboxes, making even the simplest tasks difficult, time-consuming, and costly. The reactivity of molten plutonium severely limits the container that is suitable for experimenting with molten plutonium to either a few ceramics or refractory metals, or metals with certain coatings. Also, plutonium metal is highly pyrophoric when heated or finely divided and thus molten plutonium must be kept away from oxygen. Because of the criticality hazard, metallic plutonium experiments must be conducted using less than 6 kg batches.

3.4.1. Glovebox

The greatest health hazard from plutonium arises from the emission of alpha particles. Plutonium forms an extremely fine particulate oxide, which readily disperses in air and is easily respirable. Therefore gloveboxes are required to keep the plutonium contained. Shielding for the other types of radiation, such as beta, gamma, neutrons, and x-rays, must also be provided (14).

When a glovebox must be used for containing radioactive material, many compromises must be made. All hands-on tasks are done using lead-lined gloves attached by glove ports that may not always be in the best location for the particular experiment. This is especially true for research, because in many cases research gloveboxes must be designed for many different projects. In general, performing research-type tasks in a glovebox will take at least ten times longer than if they were performed in the open.

3.4.2. Reactivity

Molten plutonium metal is very reactive (it is a better oxygen-getter than titanium) and is also a very pyrophoric substance when finely divided. One of the best methods for containing molten plutonium is a tantalum crucible with a tantalum oxide coating. Furthermore, because of the reactivity of plutonium with the atmospheric gases at elevated temperatures, any operations conducted at elevated temperatures must be done in a protective atmosphere. High vacuum has been found to be the most practical environment in which to melt plutonium. But vacuum melting further increases the difficulty of zone refining plutonium because this now requires another air tight chamber within the glovebox to contain the zone refining apparatus. However, additional purification will arise from evaporation of volatile impurities from the molten zone when the zone refining is accomplished in a high vacuum. This is important because many impurities in plutonium metal have a higher vapor pressure than plutonium.

3.5. Molten Zone Speed

The optimum rate of zone travel during zone refining depends on many factors and cannot be reduced to a simple mathematical equation. One important factor is the amount of stirring in the molten zone. For example, to obtain the same level of separation during zone refining if there is no stirring in the molten zone compared to a case where there is vigorous stirring, the speed would need to be about one one-hundredth of the case with vigorous stirring. Furthermore, when several impurity solutes are involved, the travel rate is likely to be determined by the impurity whose K_e is closest to unity. Based upon the analysis by Kristofova, Kuchar, and Wozniakova (12), K_e for most of the impurity elements of interest in plutonium are 0.6 or higher for those elements for $K < 1$. Based upon Tate's (2) and Pfann's (3) work, an optimum rate should be less than 4 in/h From a engineering stand point, any rate lower than 1/2 in/h would be impractical.

3.6. Coil Design

For zone refining to work most efficiently, the length of the molten zone should be minimized (3). This may be accomplished by optimizing coil design. Fluxtrol Manufacturing, a manufacturer of flux field concentrators, has examined this engineering problem. They designed a water-cooled three-turn copper pancake coil with a proprietary Fluxtrol flux field concentrator. A pancake coil has a higher density of flux lines over a much smaller volume than a single turn coil such as the one used by Tate and Anderson (2).

The Fluxtrol flux field concentrator increases the flux density and reduces the flux field volume giving a smaller heated zone in the workpiece and a smaller molten zone. This can be seen by comparing the flux lines with and without a Fluxtrol flux field concentrator, shown in Figure 8a and b, respectively (15).

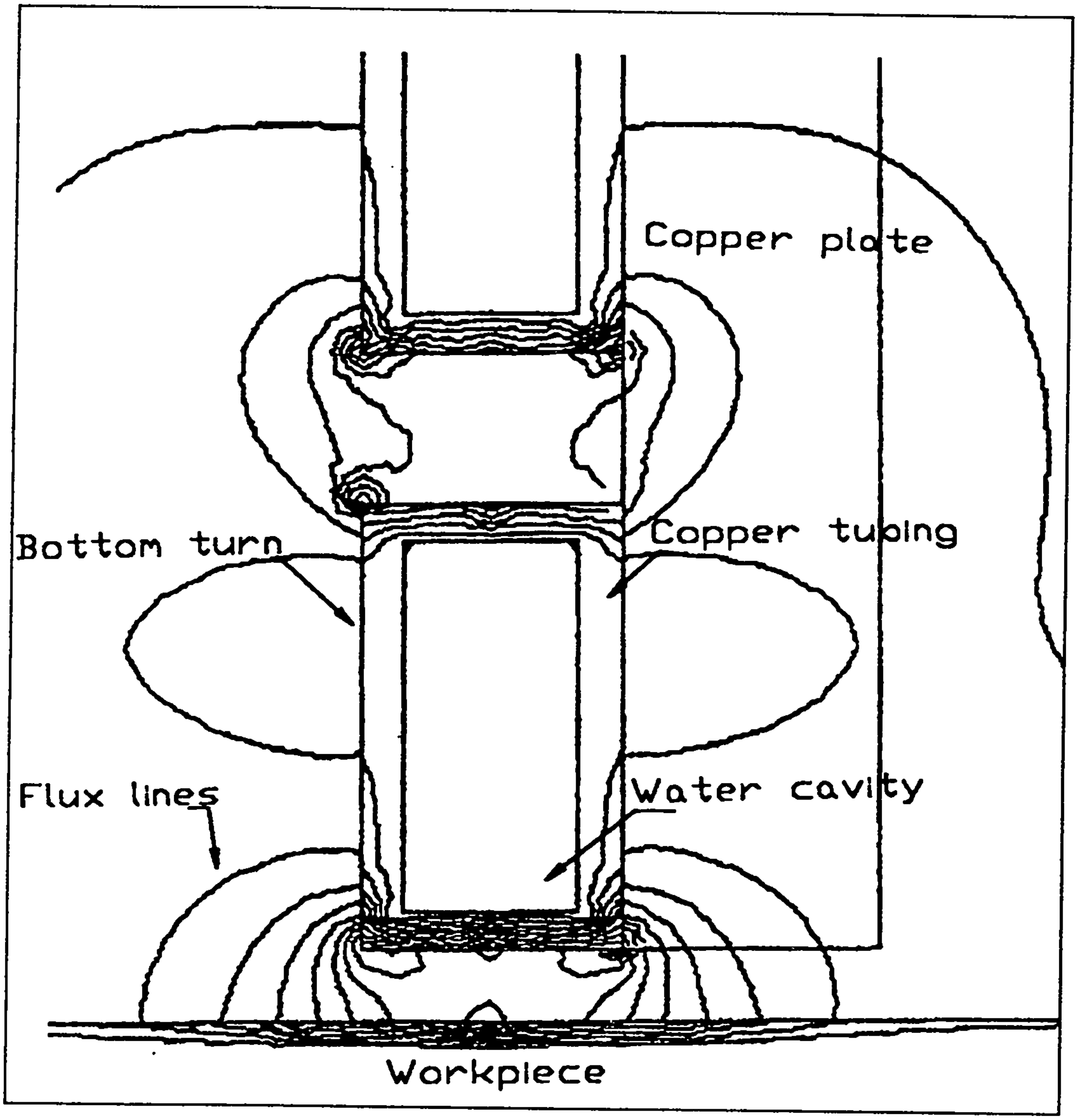

Figure 8a. Flux lines of a proposed three-turn pancake coil without Fluxtrol flux field concentrator. This figure was generated by Fluxtrol (15).

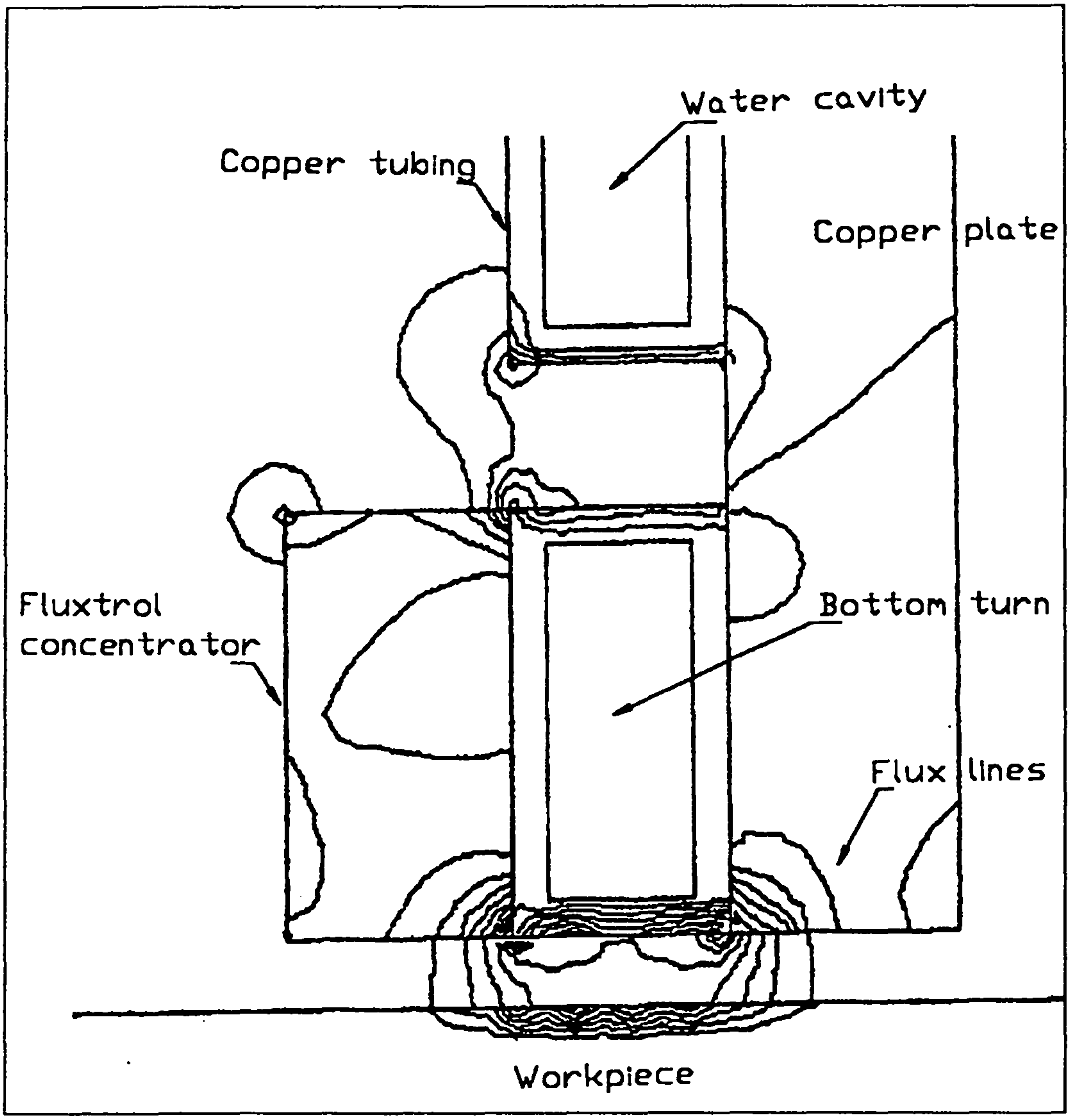

Figure 8b. Flux lines of proposed three-turn pancake coil with Fluxtrol flux field concentrator. This figure was generated by Fluxtrol (15).

Figure 8c shows the important components of the Fluxtrol coil and the positioning of the tantalum boat loaded with plutonium. On the right side of the coil is a heat sink to remove the heat of fusion as the induction coil passes along the boat (the boat moves from left to right during zone refining). This causes the boat first to be heated by induction, then cooled by the heat sink. The heat sink helps create a small molten zone as well as a platform for the boat to slide through the coil. The heat sink, copper plate, and coil turns all have cooling water flowing through them during zone refining runs to prevent heat damage to the coil turns or Fluxtrol concentrator.

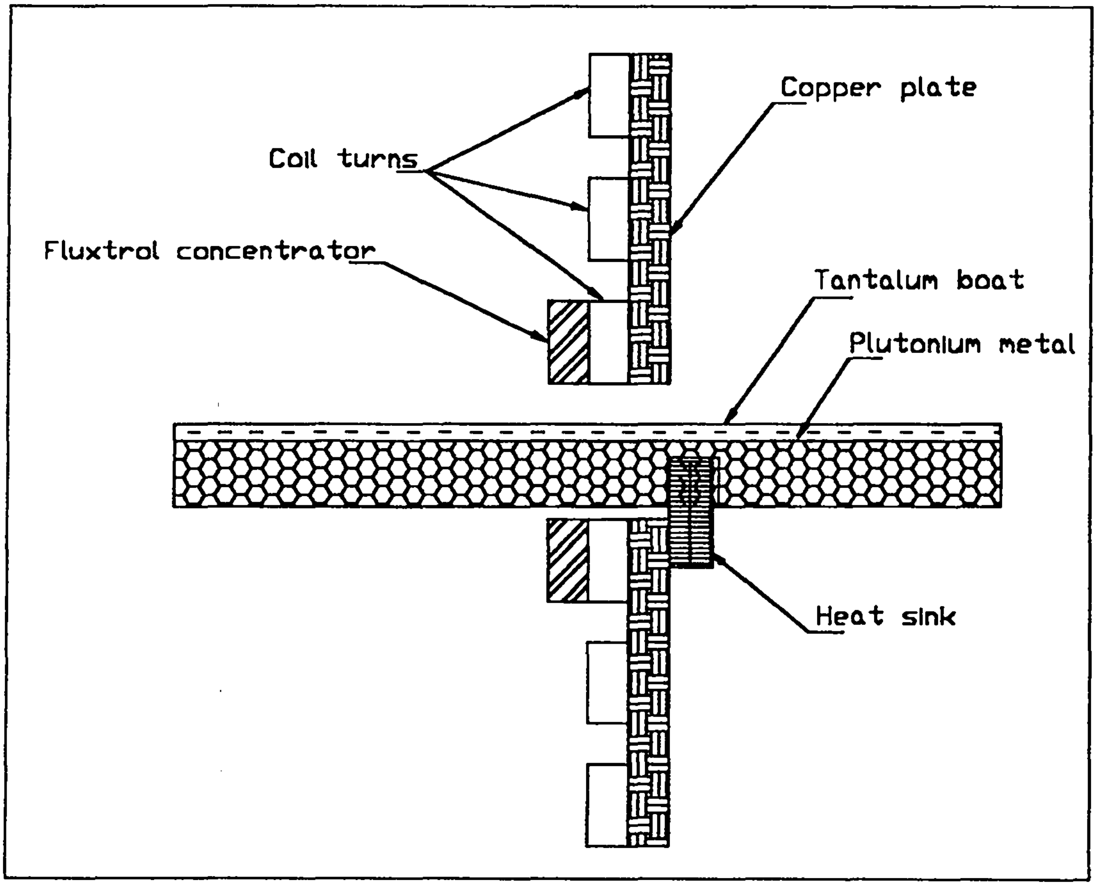

Figure 8c. Proposed three-turn pancake coil manufactured by Fluxtrol. The figure shows the three turns in the coil, copper cooling plate, Fluxtrol concentrator, heat sink, and tantalum boat loaded with plutonium metal.

3.7. Statistically Designed Experiments

The purpose of designing an experiment is to characterize a process. Purposeful selection of values for the variables of the process is the most important part of experimental design. Process efficiency is the added value provided by a statistical approach to experimentation. An efficient experiment is one that derives the required information with the least expenditure of resources (16).

3.7.1. Experimental Factorial Designs

A full factorial experiment is an experiment in which the response y is observed at all factor-level combinations of the independent variables. One approach for examining the effects of two or more factors on a response is called the "one-at a time approach". To examine the effect of a single variable, an experimenter changes the levels of this variable while holding the levels of the other independent variables fixed. This process is continued until the effect of each variable on the response has been examined while holding the other independent variables constant. If any of the independent variables interact, this approach will not work. Also, the inadequacies of the one-at-a-time approach are even more salient when trying to investigate the effects of more than two factors on a response. Factorial experiments are useful for examining the effects to two or more factors on a response y, whether or not interaction exists. Consequently, not only do we get information concerning factor interactions using a factorial experiment instead of the one-at-a-time approach, but also, when there are no interactions, we get the same amount of information about the effects of each individual factor using fewer observations (17).

3.7.2. Analysis of Variance for Experimental Factorial Designs

Thoroughly reviewing analysis of variance for experimental factorial designs is beyond the scope of this thesis. Here, those equations needed to do an analysis of variance for experimental factorial designs up to a three-factor factorial experiment with fixed effects and without replication will be presented. The following notation is used for the needed equations (17):

G: total for all sample observations (all y's added together)
n: total number of sample measurements
a: number of levels factor A is investigated at
b: number of levels factor B is investigated at
c: number of levels factor C is investigated at
n_A: number of observations at each level of factor A
n_B: number of observations at each level of factor B
n_C: number of observations at each level of factor C
A_i: sum of the n_A observations receiving the ith level of factor A
B_j: sum of the n_B observations receiving the jth level of factor B
C_k: sum of the n_C observations receiving the kth level of factor C
n_{AB}: number of observations at each combination of levels of factors A and B
n_{AC}: number of observations at each combination of levels of factors A and C
n_{BC}: number of observations at each combination of levels of factors B and C
$(AB)_{ij}$: sum of the n_{AB} observations receiving the ith level of A and jth level of B
$(AC)_{ik}$: sum of the n_{AC} observations receiving the ith level of A and jth level of C
$(BC)_{jk}$: sum of the n_{BC} observations receiving the ith level of B and jth level of C
n_{ABC}: number of observations at each combination of levels of the three factors A, B, and C
(ABC)ijk: sum of the n_{ABC} observations receiving the ith level of A, jth level of B, and kth level of C

The appropriate analysis of variance formulas for a k-factor factorial experiment with one observation per cell can be subdivided into sums of squares for main effects (variability between levels of a single factor), two-way interactions and three-way interactions, are shown below. The analysis of variance table for a three-factorial experiment without replication is shown in Table 1 (17).

The sums of squares for main effects are:

$$SSA = \sum_i \frac{A_i^2}{n_A} - \frac{G^2}{n} \qquad (5a)$$

$$SSB = \sum_j \frac{B_j^2}{n_B} - \frac{G^2}{n} \qquad (5b)$$

$$SSC = \sum_k \frac{C_k^2}{n_C} - \frac{G^2}{n} \qquad (5c)$$

The sums of squares for two-way interactions are:

$$SSAB = \sum_{ij} \frac{(AB)_{ij}^2}{n_{AB}} - SSA - SSB - \frac{G^2}{n} \tag{6a}$$

$$SSAC = \sum_{ik} \frac{(AC)_{ik}^2}{n_{AC}} - SSA - SSC - \frac{G^2}{n} \tag{6b}$$

$$SSBC = \sum_{jk} \frac{(BC)_{jk}^2}{n_{BC}} - SSB - SSC - \frac{G^2}{n} \tag{6c}$$

The sum of squares for a three-way interaction is:

$$SSABC = \sum_{ijk} \frac{(ABC)_{ijk}^2}{n_{ABC}} - SSAB - SSAC - SSBC - SSA - SSB - SSC - \frac{G^2}{n} \tag{7}$$

Total sum of squares is:

$$TSS = \sum y^2 - \frac{G^2}{n} \tag{8}$$

From Table 1 it can be seen that there is no source of variability designated as error because there are no degrees of freedom. This is because there are no replications to give more degrees of freedom. Thus, for the case with no replications, the error term becomes the higher-order interactions, which assumes that the higher-order interactions are negligible.

Once the analysis of variance table is complete, the calculated F values can be compared with values from the F distribution to conclude whether or not there are differences among the main effects and if there are interactions between the main effects (17).

For this thesis, experimental factorial designs are used because obtaining each datum point obtained is very expensive, and thus by using factorial designs the number of data points are greatly reduced. For this experiment, the response y will be impurity concentration

TABLE 1: ANALYSIS OF VARIANCE FOR A THREE-FACTORIAL EXPERIMENT WITH FIXED EFFECTS AND WITHOUT REPLICATION

Source	Sum of Squares (SS)	Degrees of Freedom (DF)	Mean Squares (MS) MS=SS/DF	F Value F= MS/MSABC
Main effects				
A	SSA	a-1	MSA	MSA/MSABC
B	SSB	b-1	MSB	MSB/MSABC
C	SSC	c-1	MSC	MSC/MSABC
Interactions				
AB	SSAB	(a-1)(b-1)	MSAB	MSAB/MSABC
AC	SSAC	(a-1)(c-1)	MSAC	MSAC/MSABC
BC	SSBC	(b-1)(c-1)	MSBC	MSBC/MSABC
ABC	SSABC	(a-1)(b-1)(c-1)	MSABC	
Totals	TSS	abc-1		

in the plutonium metal. The fixed effects will be zone refining passes, molten zone speed, power settings to the coil, and position along the rod where the sample was taken. In all cases, no more than three fixed effects will be used at once and without replication. Given the fact that the minimum number of data points will be used in each case, it will be difficult to obtain significant results from the analysis of variance because of the low number of degrees of freedom.

CHAPTER 4

EXPERIMENTAL PROCEDURES

4.1. Experimental Objective

The main objective of this experiment was to demonstrate the possibility of developing a zone refining process to purify plutonium metal. Thus, this experiment was designed to prove that the principles of zone refining apply to plutonium metal. Consequently, the main objective of this thesis was to see if passing molten zones along a plutonium metal rod in one direction would cause the selected impurities to move. The impurities were ten different elements that were added to the plutonium metal in order to make the different plutonium alloys. Minor objectives of this experiment were to observe the behavior of gallium during the zone melting process with and without other elements present in plutonium metal, and an examination of the effects of the number of passes, the molten zone speed, and the power settings.

4.2. Material Preparation

To achieve the objectives of this experiment, two plutonium alloys were prepared; a gallium alloy and an impurity alloy. The plutonium starting material was electrorefined (ER) plutonium metal, typically 99.9 percent pure by weight. The gallium alloy contained 1 W/o gallium, a stabilized δ-phase alloy. The impurity alloy was the same as the gallium alloy except that it additionally contained nine impurity elements at 1000 ppm each by weight. The impurity alloy was needed to prove most of the objectives of this experiment. Two microprobe samples were taken of the impurity alloy to determine the effective distribution coefficient of the cast material.

The best way to understand the experimental procedure is to follow the paths shown in the experimental procedure flow diagram (Figure 9).

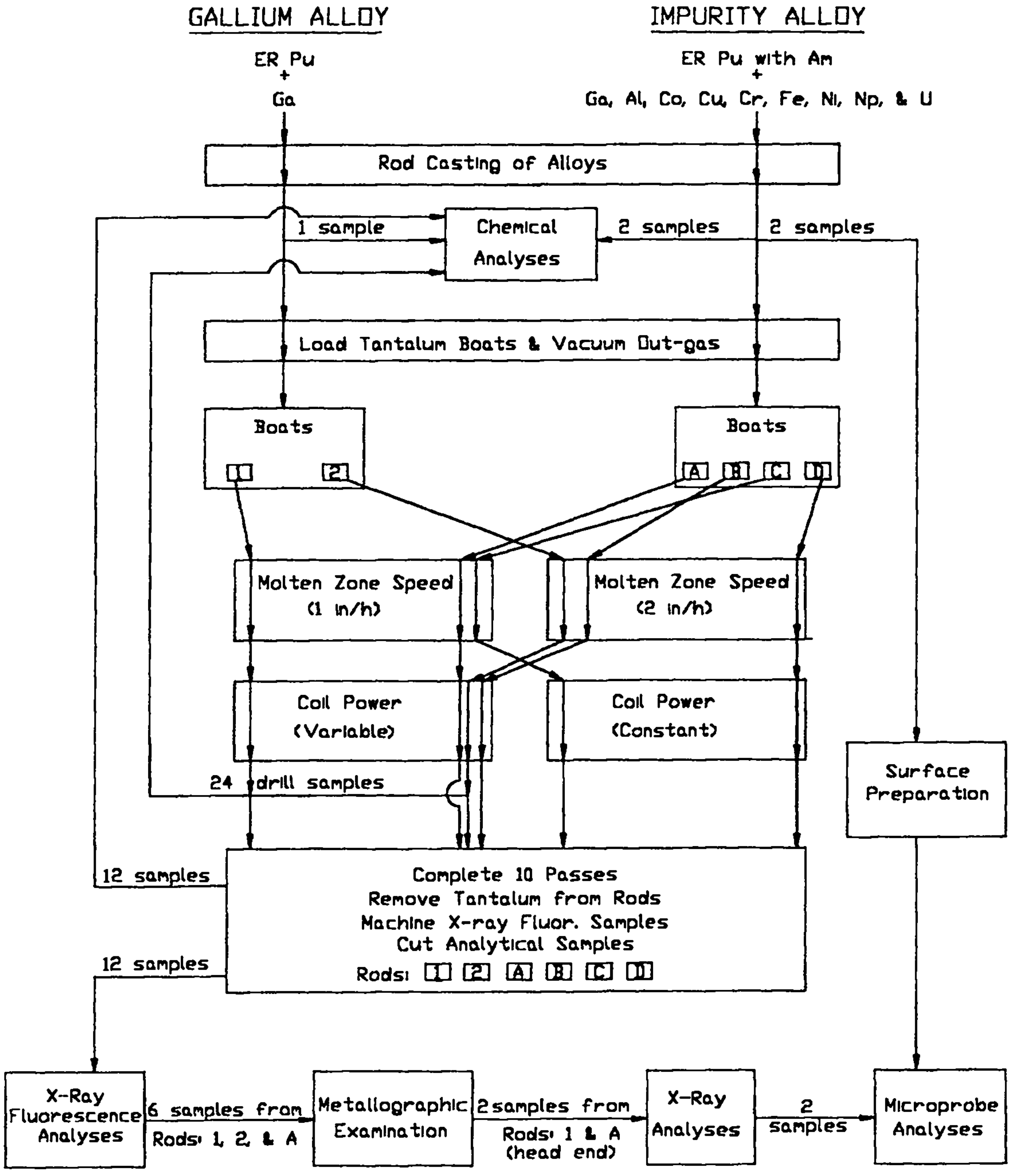

Figure 9. Experimental procedure flow diagram.

4.2.1. Gallium Alloy

This alloy was fabricated using the following procedure:

- High purity electrorefined plutonium metal was used.
- Gallium was added to this material to produce a nominally 1 W/o alloy (approximately 3.4 A/o).
- The charge was vacuum cast to 5/8 inch rods using the following schedule:
    - The charge was heated to 900 ^{o}C and held for 20 minutes with constant stirring under a vacuum of about 5 X 10^{-3} torr.
    - The charge was bottom poured into a rod mold made of titanium.
    - A 5 g sample was taken from the middle of one rod for chemical analyses.

4.2.2. Impurity Alloy

This alloy was fabricated using the following procedure:

- High purity electrorefined plutonium metal that contained 2000 ppm (0.2 W/o) americium was used.
- Gallium was added to this material to produce a nominally 1 W/o of alloy (approximately 3.4 A/o)
- Amounts of aluminum, cobalt, copper, chromium, iron, nickel, neptunium, and uranium were added to produce an alloy containing 1000 ppm (0.1 W/o) each element.
- The charge was vacuum cast to 5/8 inch rods using the following schedule:
    - The charge was heated to 900 ^{o}C and held for 20 minutes with constant stirring under a vacuum of about 5 X 10^{-3} torr.
    - The charge was bottom poured into a rod mold made of titanium.
    - A 5 g sample was taken from the bottom and top of one of the rods for chemical analyses.
    - A second 5 g sample was taken from the bottom and top of rod for microprobe analyses.

4.2.3. Tantalum Zone Refining Boats

The tantalum boats were fabricated from 0.020-in thick tantalum tubing stock with a 1 in outside diameter and 4 ft. long. The tubes were laser cut in half longitudinally and then cut into 9 in long sections. Each section was cut such that a 5 in trough was left. Tantalum ends were then welded on each trough end to form a 5 in cavity. The boats were heat-treated for 6 h at 450 °C in air to form a protective tantalum oxide coating. The tantalum oxide layer decreases the reaction of the molten plutonium with the tantalum metal.

4.2.4. Loading of Zone Refining Boats

Two boats were each loaded with gallium alloy (Boats 1 and 2) and 4 boats were each loaded with impurity alloy (Boats A, B, C, and D). All 6 boats were loaded with approximately the same amount of plutonium metal alloy. The boats were then placed in a vacuum furnace, placed under a vacuum of 1 X 10 $^{-7}$ torr, heated to 700 °C and held at temperature for 1 h The high vacuum step was used to out-gas the plutonium metal. Figure 10 shows one of the loaded tantalum boats after the high-vacuum melting step.

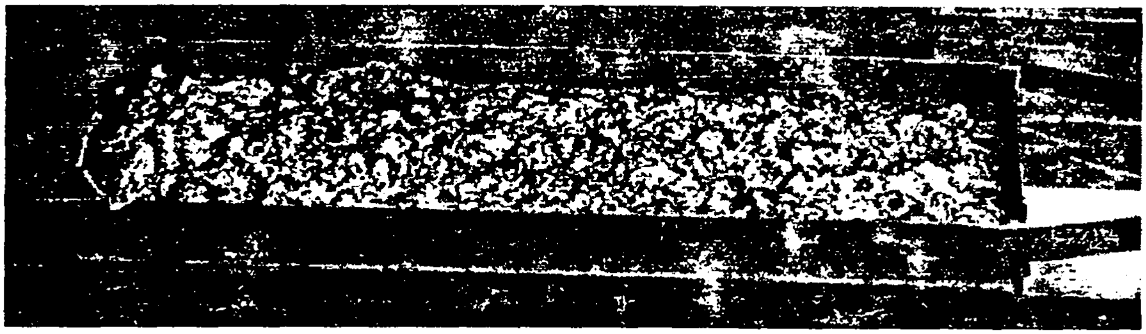

Figure 10. Tantalum boat loaded with plutonium metal.

4.3. Zone Refining Apparatus

The zone refining equipment was built specifically for this experiment. An existing glovebox and power supply were adapted for the experiment. The power supply was a 75 kW Inductotherm unit that operated at about 2.5 kHz. Based on the skin depth equation (Eq. 4, p. 13) the workpiece diameter was required to be about 1 in for this power supply to induce heating in a plutonium metal rod.

To move the plutonium rod at a very slow controlled speed (1 or 2 in/h) through the induction coil, a linear precision table was designed and built by Micro Kinetics Corporation. The zone refining speeds were selected based on results obtained from Tate and Anderson (2). The linear precision table consisted of a single-axis translation table with 9-in of travel, a single-axis motor controller and a hand-held remote computer (HHRC) for the motor controller. The induction coil was designed and built by the Fluxtrol Manufacturing. The coil consisted of a water-cooled copper three-turn pancake coil with a Fluxtrol flux field concentrator, and a water-cooled copper backing plate and heat sink for the tantalum boat to slide across. Two separate water cooling lines enter the coil, one to cool the coil, the other to cool the copper cooling plate and heat sink (Figure 8c). This design minimizes the size of the molten zone. A vacuum chamber was designed and built at Los Alamos that would contain the entire zone refining apparatus and fit inside the glovebox. This apparatus is shown in Figures 11a and b.

The zone refining apparatus and an enlargement of the coil area are shown in Figures 11a and b, respectively. A copper cooling line on the lid keeps the vacuum chamber cool during processing. The O-ring seal on top of the vacuum chamber makes the chamber vacuum tight. The induction pass-through into the chamber is on the back side of the chamber. This feed-through supplies both the induction power and water cooling to the induction coil. The inlet and outlet water cooling lines (the two cooper lines in Figure 11b) on the left side of the chamber that cool the copper plate and heat sink components in the left side of the coil assembly. The Fluxtrol concentrator the right side of the coil. The coil assembly is mostly surrounded in a green- colored insulating material called G-10. The

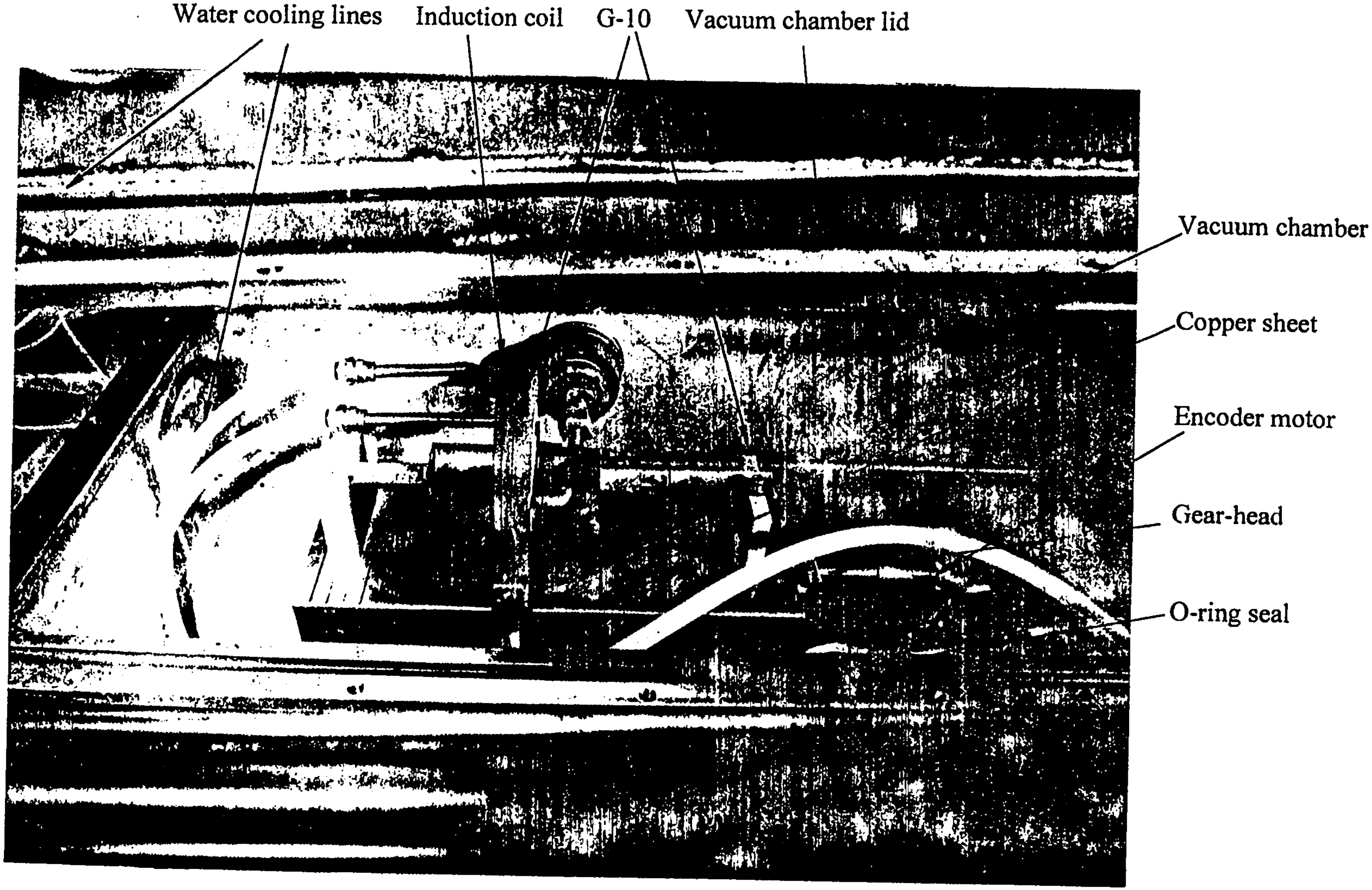

Figure 11a. Zone refining apparatus.

Figure 11b. Zone refining apparatus (induction coil).

zone refining boat holder and part of the induction pass-through is also made of G-10. G-10 is used in this apparatus because the induction current must not make electrical contact with the chamber or make a short circuit and G-10 does not have an effect on the vacuum. The translation table cannot be seen because it is covered by a thin copper sheet that is required to insulate the translation table from the induction field produced by the coil. The encoder motor and gear-head assembly are visible on the right side of the chamber.

The front and back of the glovebox that contains the vacuum chamber is shown in Figures 12a and b, respectively The glovebox is constructed of 304 stainless steel and is lead-lined. The glove ports in the middle and near the top of the glovebox are fitted with lead-lined gloves. A pressure gauge (inches of water) near the top of the glovebox monitors the difference between the internal glovebox pressure and room pressure. This is important because the pressure in the glovebox must be less than the room pressure, so that if there is a breach in the glovebox, air will flow in instead of contamination flowing out of the glovebox. Below the glovebox are insulated water cooling lines and the water interlocks. The water interlocks monitor water flow and water temperature. If either gets out of the desired range, the interlock shuts off power to the zone refining coil. The top of the vacuum chamber lid and the electric hoist used to raise the vacuum chamber lid appears on the left inside the glovebox.

Figure 12b shows the back side of the zone refining glovebox. The induction power leads for the zone refiner are below the glovebox in the center. On the left side, also below the glovebox, is the cryo-pump temperature gauge. This temperature is very important because the cryo-pump will not work well if the temperature is above 20 degrees Kelvin In Figure 12b, the zone refining apparatus view port in the vacuum chamber lid appears on the right. To the left of this glovebox window is the HHRC. Left of the HHRC is the plutonium hand monitor probe used to check one's self for plutonium contamination each time one removes his hands from the gloves.

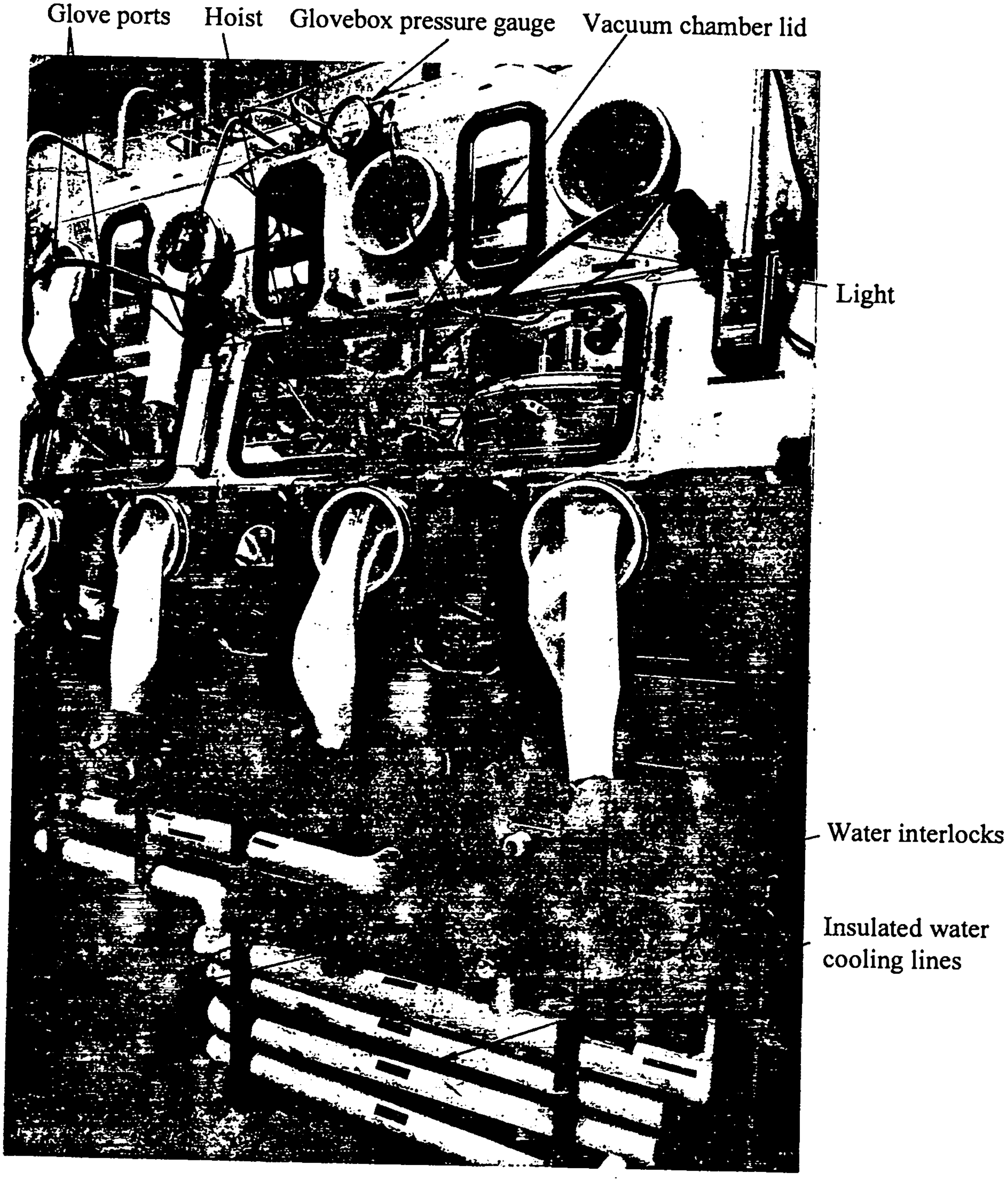

Figure 12a. Front Side of Zone Refining Glovebox.

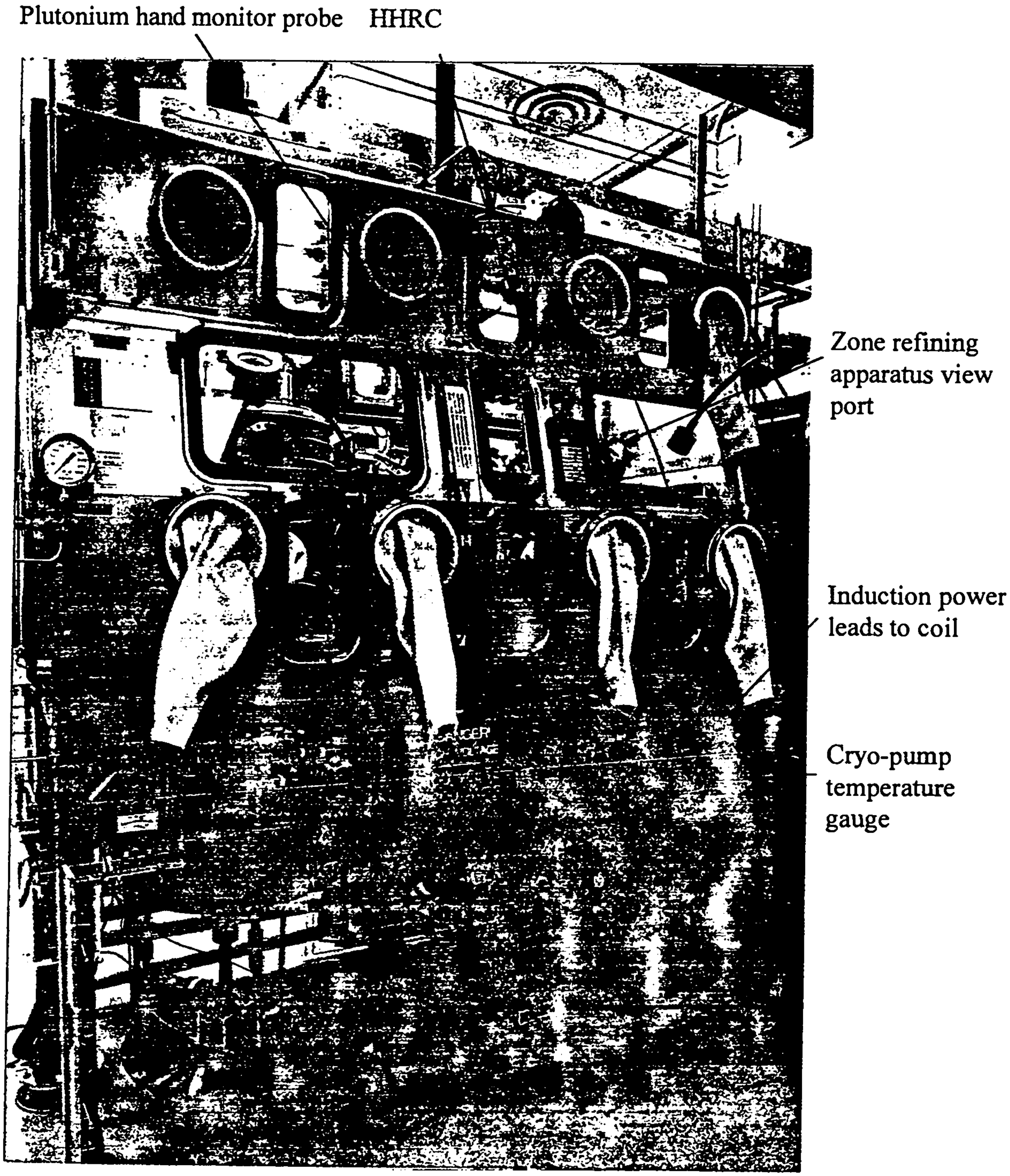

Figure 12b. Back side of zone refining glovebox.

4.4. Zone Refining Runs

For this project, a run was made using 6 boats (2 boats with gallium alloy and 4 boats with impurity alloy as shown in Figure 9). Each boat contained about the same amount of plutonium metal. Ten passes were made for each run. Each pass started at the front of the boat (or rod) which will be defined as the head end. Also, the end of each boat (or rod) will be defined as the tail end. All experimental runs were done in a vacuum of $1X10^{-4}$ torr or better.

The width of the molten zone can be made as small as possible by manually varying the power to the coil. With constant power to the coil, a wider molten zone results, but with constant power to the coil, the process is much easier to control.

To make these power changes requires visual observation of the molten zone. The molten zone is clearly visible during the first few passes because a plutonium oxide layer builds up on the surface of the charge. A similar phenomenon was observed with uranium by Bieber, Schreyer, and Williams (9). Power changes to the coil can be made by using an infrared pyrometer and the molten zone temperature readings recorded during the first pass. This method becomes less accurate as the oxide layer becomes thicker with each pass because the oxide layer decreases the amount of energy that is detected by the infrared pyrometer, thus causing the infrared pyrometer reading to be low. Additionally, the infrared pyrometer readings have less meaning (melting point of the plutonium in the molten zone) with each pass because as the impurities in the plutonium metal move along the rod, the change in the concentration causes the alloy's melting point to change. The constant versus variable power trade-off was examined by making identical runs using the impurities alloys at a speed of 1 and 2 in/h with variable power to the coil (Boats A and B) and constant power to the coil (Boats C and D) with everything else being the same (Figure 9).

4.4.1. Gallium Alloy with Variable Power (Boats 1 and 2)

These two runs were made using the following procedure:

- The tantalum boat was loaded into the apparatus and aligned so that the back of the coil was positioned at the back of the boat (tail end)
- The vacuum chamber lid was put in place and closed.
- The vacuum chamber was evacuated and back-filled 3 times with high purity argon.
- The roughing vacuum valve to vacuum chamber was opened for 1 h, then closed.
- The cryo-pump valve opened if the vacuum chamber pressure was less than 0.05 torr and the cryo-pump temperature was less than 20 degrees Kelvin
- The desired speed (1 in/h for Boat 1 and 2 in/h for Boat 2) and the distance the boat would travel (4 in) was set using the HHRC.
- Cooling water was supplied to the apparatus.
- The first pass was started with the power supply and set at 10 kW.
- Once a molten zone was established, the boat travel was begun. Coil power was decreased in 500 watt amounts until the molten zone was observed to be as narrow as possible. The correct speed was confirmed with the HHRC display. The speed was monitored by timing the travel of the boat for the first 1 min period, then for a 1 h period.
- The power was adjusted every 10 min to keep the molten zone as narrow as possible and temperature readings were taken on the molten zone using the infrared pyrometer.
- After the first pass was complete, the power to the coil was turned off and the boat returned to its original position with the HHRC and then the process equipment was turned off.
- The vacuum chamber was opened after the apparatus has cooled for at least 5 h and the boat removed and sent to a drill-press glovebox for sampling.

- Three 1 g samples were drilled from the plutonium metal in the boat. The 3 samples are taken along the centerline of the plutonium-filled boat approximately a 1/4 in from each end of the boat and in the center of the boat about 1/10 in below the surface of the plutonium metal as shown in Figure 13.

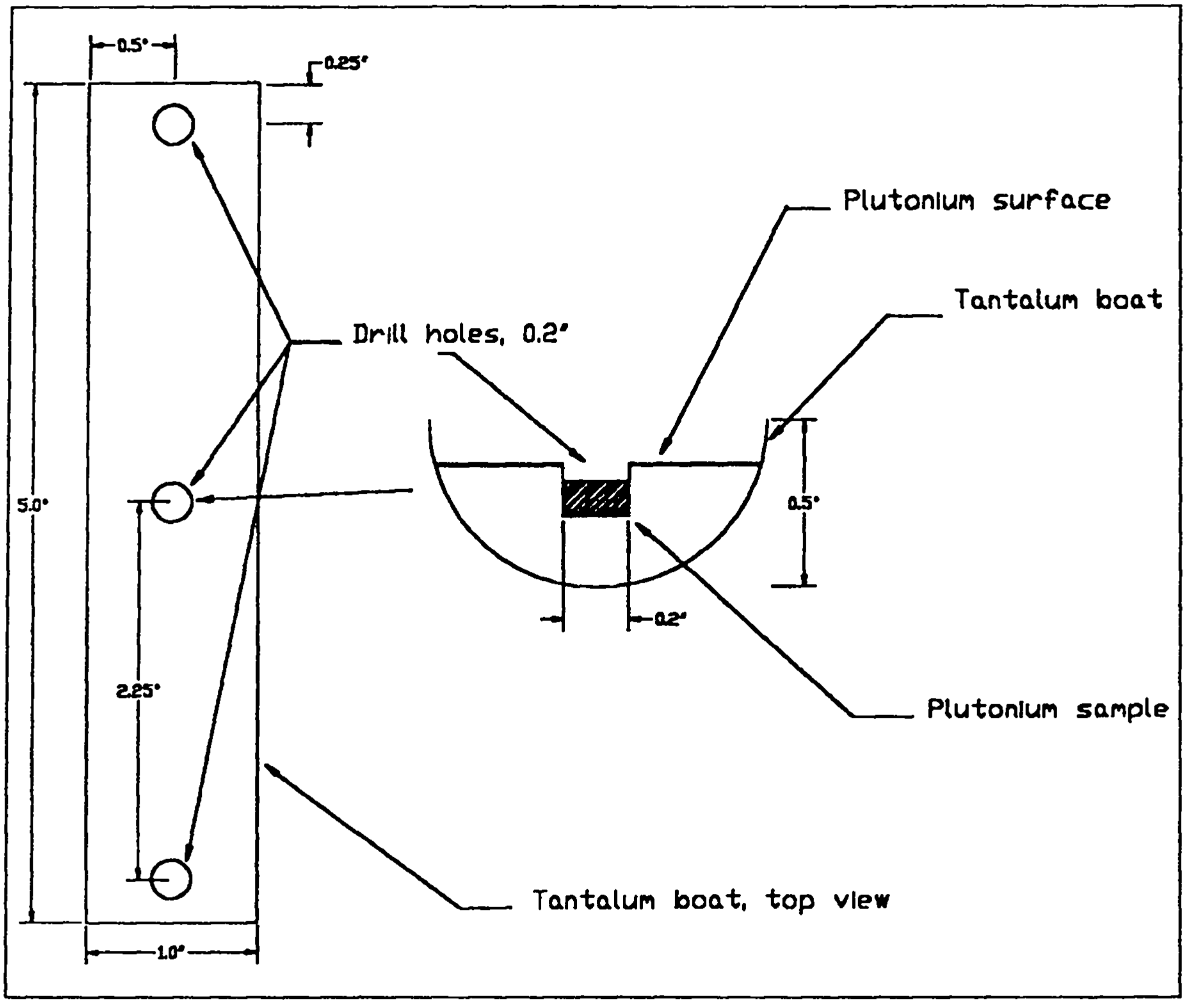

Figure 13. Plutonium drill samples taken from tantalum boat.

- The boat was put back in the zone refining apparatus and the second pass was completed as the first pass, except the power to the coil was adjusted using the infrared pyrometer and based on the infrared pyrometer values recorded during the first pass.
- The third and fourth passes were completed by following the same procedure as the second pass.
- The fifth pass was done the same as the second pass except the drill samples were not taken.
- The sixth through the tenth pass was done the same as the fifth pass.

4.4.2. Impurity Alloy with Variable Power (Boats A and B)

These two runs were done the same as the gallium alloy except that the boat was not removed from apparatus after passes one through four for taking analytical samples. Boat A was run at a speed of 1 in/h, and Boat B was run at a speed of 2 in/h (Figure 9).

4.4.3. Impurity Alloy with Constant Power (Boats C and D)

The same procedure was followed as with the impurity alloy with variable power except that the power was always kept at 8 kW other than in the beginning of the run when it was 10 Kw. Boat C was run at a speed of 1 in/h and Boat D was run at a speed of 2 in/h (Figure 9).

4.4.4. Removal of Samples From Boats After Runs Complete

After completion of 10 passes, the six alloys and their tantalum boats were removed for sampling. The tantalum boats were cut from the plutonium metal rod, taking care not to cut the glovebox gloves which would cause a breach in the glovebox integrity.

X-ray fluorescence analyses samples were taken from both ends of the six rods. The samples were taken by machining two longitudinal cuts 1/8 in apart perpendicular to the end of the rod in the center of the rod end. A third cut was made parallel to the end of the rod one-inch from the end to remove the sample, as shown in Figure 14. Two 1 g analytical chemistry samples were cut from both ends of each rod using the rectangular pieces produced when the x-ray fluorescence samples were machined as shown in Figure 14.

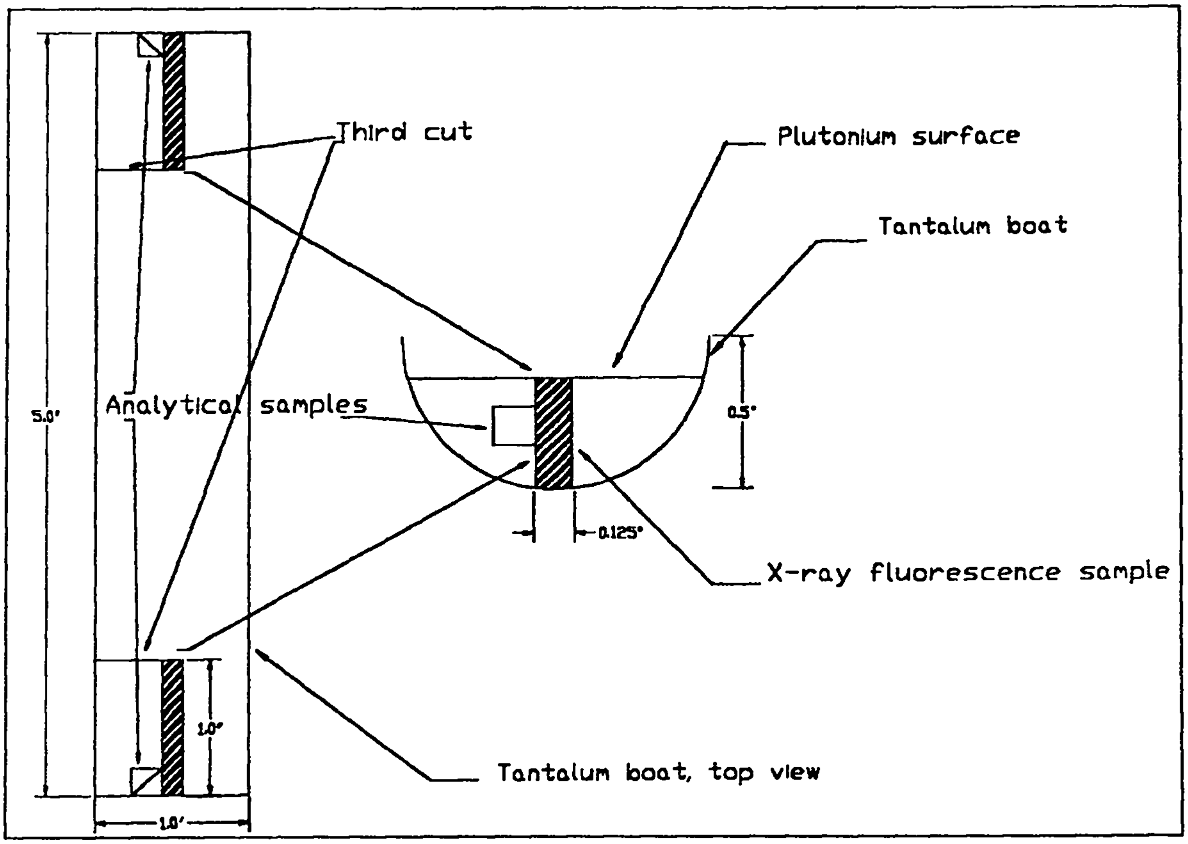

Figure 14. X-ray fluorescence and analytical samples taken from each rod.

4.5. Chemical Analysis, Microprobe Analysis, Metallography, and X-Ray Analysis

The concentrations of gallium and all other impurities in each alloy were determined using the best technique available. Analyses were performed by the analytical chemistry group at the Los Alamos National Laboratory.

Analytical samples were taken as shown in Figure 9 and as follows:

- from each of the as-cast alloys (3 samples);
- from the head end, middle, and tail end of the 2 gallium alloys after each of the first 4 passes (24 samples);

- from the head and tail ends of the gallium alloys at the end of each run of 10 passes (4 samples);
- from the head and tail ends of the impurity alloys at the completion of each run of 10 passes (8 samples).

4.5.1. Impurity Element Analysis

Emission spectroscopy was used to determine the concentrations of the impurity elements. Each sample was dissolved in concentrated HCl. The resulting solution served as the analyte for an inductively coupled plasma atomic emission spectrograph.

4.5.2. Gallium Analysis

Gallium was analyzed using x-ray fluorescence. Gallium was selectively removed from the above analytes (section 4.5.1.) by an ion exchange resin The resin was subsequently stripped of the gallium, and the resulting solution was analyzed for that element (18).

4.5.3. Impurity Element Distribution

The as-cast impurity alloy was analyzed to determine how well the added impurity elements were distributed in the alloys. The head end of zone refined Rods 1 and A were also analyzed to determine the gallium distribution across the microstructure. The surface preparation of the 2 samples cut from the upper and lower end of one of the as-cast rods was the same as that used for the 2 samples taken from Rods 1 and A (see Metallography, section 4.5.5.). A 50 keV MBX Cameca electron beam microanalyzer (microprobe) was used for this purpose.

The maximum and minimum concentration of each of the 10 elements was determined by making a scan across the sample using the microprobe. Each scan was approximately 70 to 220 microns (the finer the microstructure, the shorter the scan length and the distance between data points) depending on how fine the microstructure was, as observed in a backscattered electron image. For the impurity alloy, one scan was made in the center of each sample. For the samples from the zone refined rods, one scan was made near the rod center and one near the rod edge.

4.5.4. Elemental Mapping

Samples taken from the head and tail ends of the impurity alloys after the completion of each run (10 passes) were used to map the distribution of the impurity elements. An Omicron Micro-Fluorescence instrument was used for this analysis. The scan began at the head end of the rod and moved toward the middle of the rod along the centerline of the sample. The spot size was 500 microns. Concentrations were determined every 500 microns for the first 1/4 in, and then every 2000 microns for the remaining 3/4 in of the sample.

4.5.5. Metallography

After the above fluorescence analysis was complete, the samples were prepared for metallographic observation. Their surfaces were prepared using the following standard procedures:

- samples were mounted into 1-1/4 in molds and cast in Epon 815 epoxy;
- samples were first ground (beginning with 180 grit papers, then taken through 240, 320, 400, 600 grit and finally 600 soft) using PF-5060 Performance Fluid as a lubricant and coolant;
- samples were polished on nylon cloth, flat with 6 μ-m diamond and finally with 1 μ-m using De-Slov-It (a mineral oil base lubricant);
- samples were then etched at 4 volts DC in a solution of 10 part of nitric acid and 90 parts of dimethlyformamide.
- The samples were photographed on a Leco 300 Metallograph using bright field illumination.

4.5.6. X-Ray Analysis

After metallographic observations were complete on the two head end samples from Rods 1 and A, they went for x-ray analyses. This was accomplished using a Scintag XDS 2000 (45 Kev) x-ray diffractometer. For each sample, 1 analysis was done near the center of the sample to determine the plutonium phases present.

CHAPTER 5

RESULTS AND DISCUSSIONS

5.1. Analyses of As-Cast Alloys

The results of chemical analyses for the gallium as-cast (one sample taken) and impurity as-cast alloys (two samples taken) are shown in Table 2. These results show that the gallium alloy was of modest purity with a total impurity of 0.054 W/o, not counting the added gallium or americium. The impurity element americium forms continuously from radioactive decay of ^{241}Pu. This is why two values for americium are provided. The estimated americium concentration is much higher than what was originally determined by analytical chemistry (Table 2). There was a long time period (12 months for gallium alloy and 29 months for impurity alloy) between submission of analytical samples and zone refining.

The results from the two samples taken from the impurity alloy show that it is of modest purity with a total impurity of 0.023 W/o, exclusive of americium and the added elements. Most of the added elements in the impurity alloy are very close to the targeted levels, except chromium and uranium. One possible explanation was that uranium and chromium were partly held up in the crucible slag during the casting process.

The results of the microprobe analysis taken from the as-cast impurity alloy were about the same for both samples (microprobe Samples 1 and 2). Optical microscopic examination before microprobe analysis revealed that both samples had a similar fine microstructure throughout with no evidence of dendrites. Some results from the microprobe analysis of Sample 2 are shown in Figures 15a through i. Figure 15a shows the backscattered electron image for Sample 2, revealing areas of elements with atomic numbers different than that of the matrix material (plutonium). Two-dimensional mapping for the 10 elements of interest revealed segregation of iron, nickel, cobalt, copper, gallium, and uranium (see x-ray images in Figure 15b through h). Chromium inclusions were visible in both samples (Figure 15b) and when this figure is compared to chromium-plutonium microstructures shown in

TABLE 2: CHEMICAL ANALYSES OF AS-CAST ALLOYS
Concentration in ppm by weight (3 sig. figs. max)

Element	Gallium Alloy	Impurity Alloy, Sample 1	Impurity Alloy, Sample 2
Gallium	9,940	9,900	9,800
Aluminum	160	1,100	1,140
Americium	338, 710**	1,180, 2079**	1,170, 2069**
Cobalt	30	1,100	1,090
Copper	20	1,100	1,110
Chromium	46	500	540
Iron	80	1,100	1,100
Nickel	28	1,100	1,140
Neptunium	*	965	959
Uranium	*	210	285
Beryllium	5	4	4
Calcium	5	3	7
Carbon	36	56	45
Lithium	11	8	8
Magnesium	5	5	8
Manganese	5	6	6
Potassium	50	68	*
Silicon	*	*	30
Sodium	*	*	*
Strontium	5	*	*
Titanium	22	5	5
Tungsten	29	70	103
Zinc	6	4	6

* Below limit of detection

** Estimated americium, including americium formed from decay

Cramer and Bergin (19) it can be concluded that theses inclusions are a chromium solid solution. When Figures 15a and b are compared the chromium inclusions can also be observed in the backscattered electron image (Figure 15a). In the case of gallium (Figure 15g), it is hard to see the significant segregation from the two-dimensional mapping without also examining the quantitative scan for gallium (Figure 15i). The quantitative scans showed

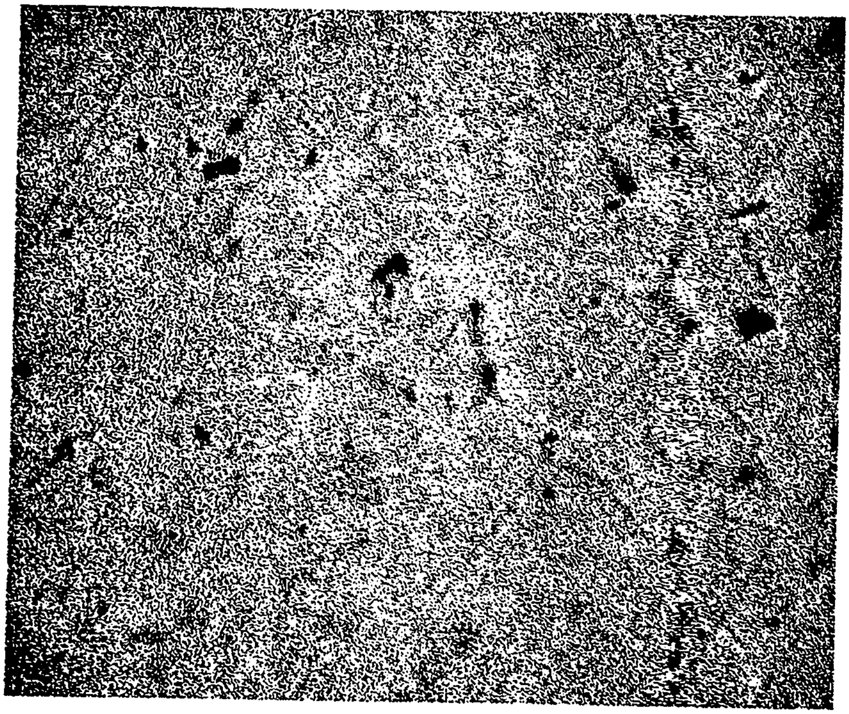

Figure 15a. Backscattered electron image for Sample 2 of the impurity alloy (2000X).

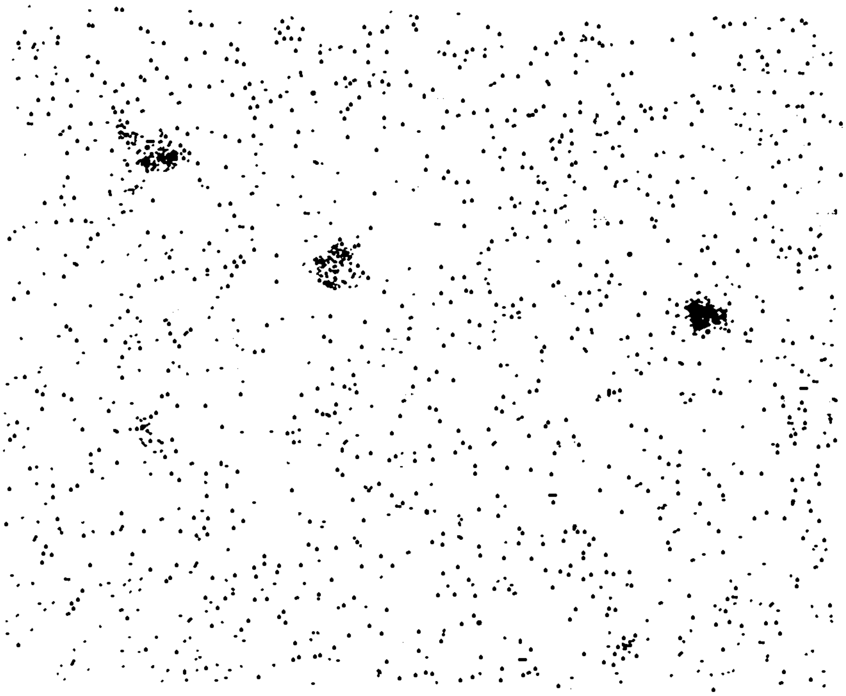

Figure 15b. X-ray image from two-dimensional mapping of chromium in plutonium for Sample 2 of the impurity alloy (2000X).

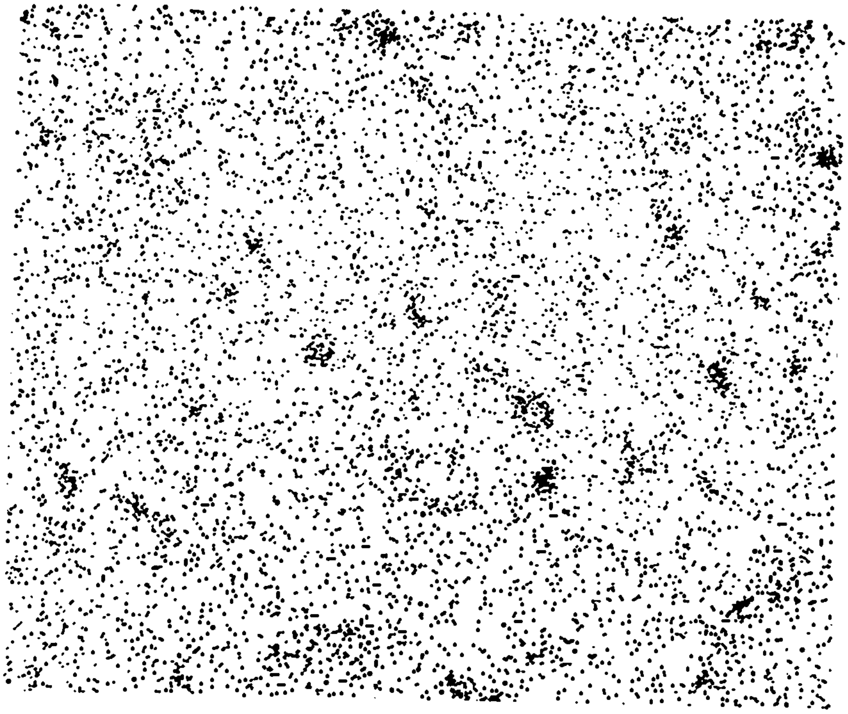

Figure 15c. X-ray image from two-dimensional mapping of iron in plutonium for Sample 2 of the impurity alloy (2000X).

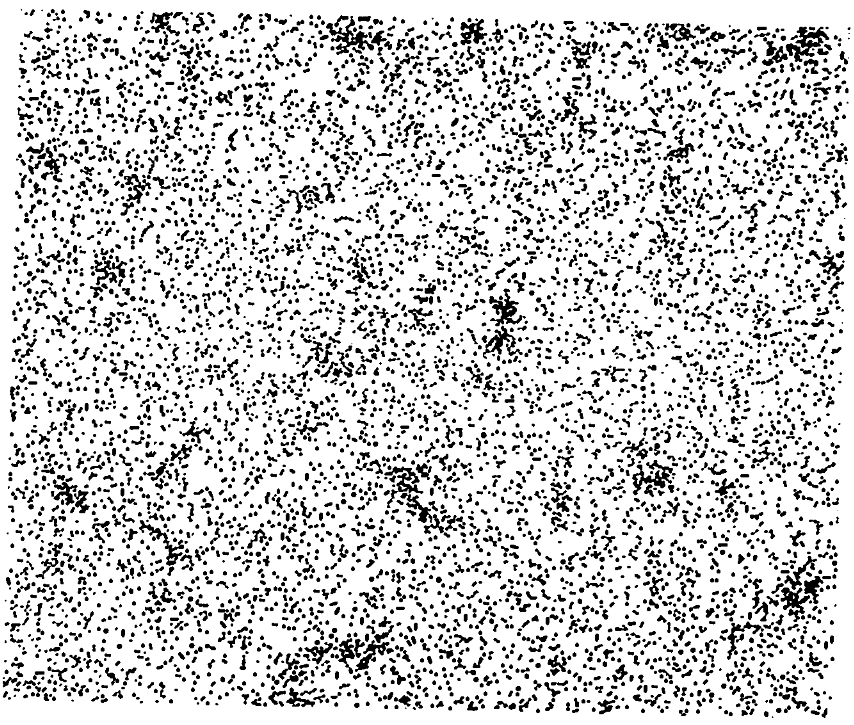

Figure 15d. X-ray image from two-dimensional mapping of nickel in plutonium for Sample 2 of the impurity alloy (2000X).

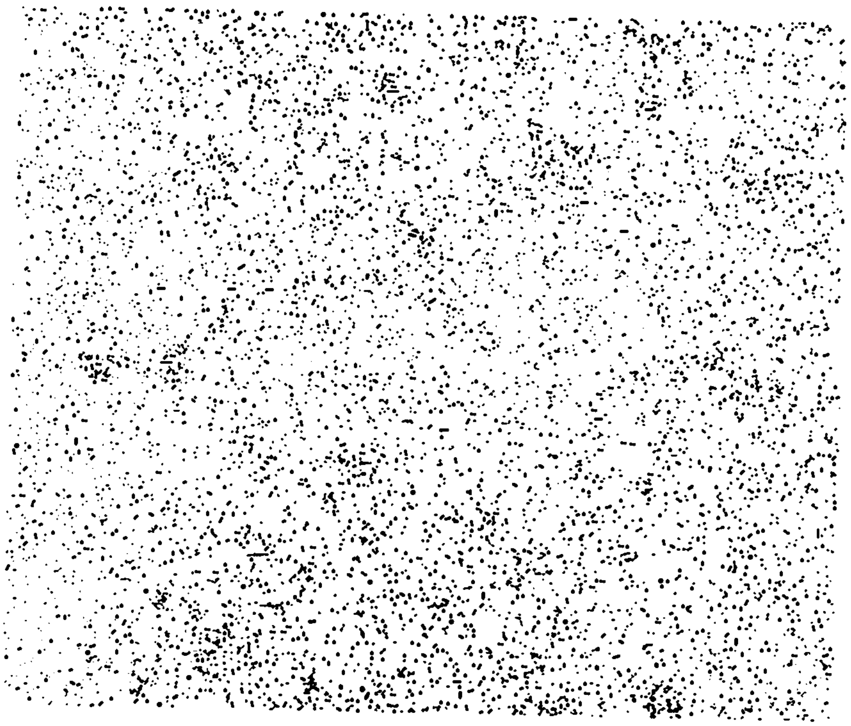

Figure 15e. X-ray image from two-dimensional mapping of cobalt in plutonium for Sample 2 of the impurity alloy (2000X).

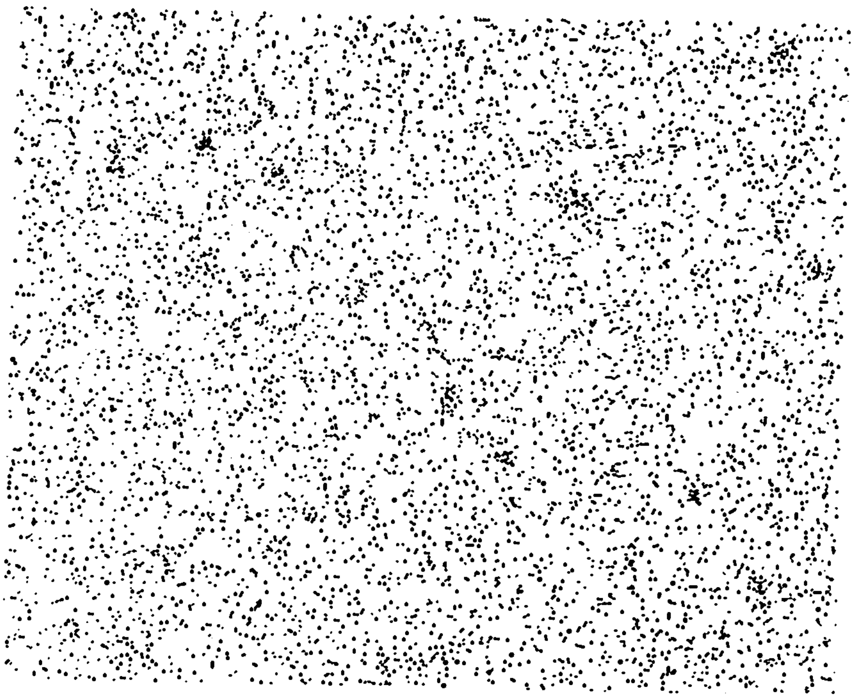

Figure 15f. X-ray image from two-dimensional mapping of copper in plutonium for Sample 2 of the impurity alloy (2000X).

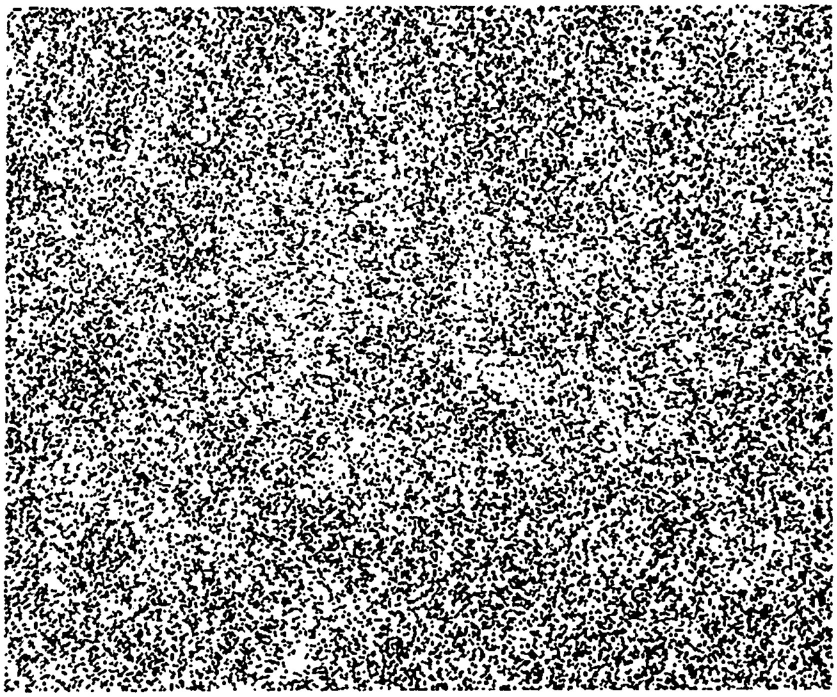

Figure 15g. X-ray image from two-dimensional mapping of gallium in plutonium for Sample 2 of the impurity alloy (2000X).

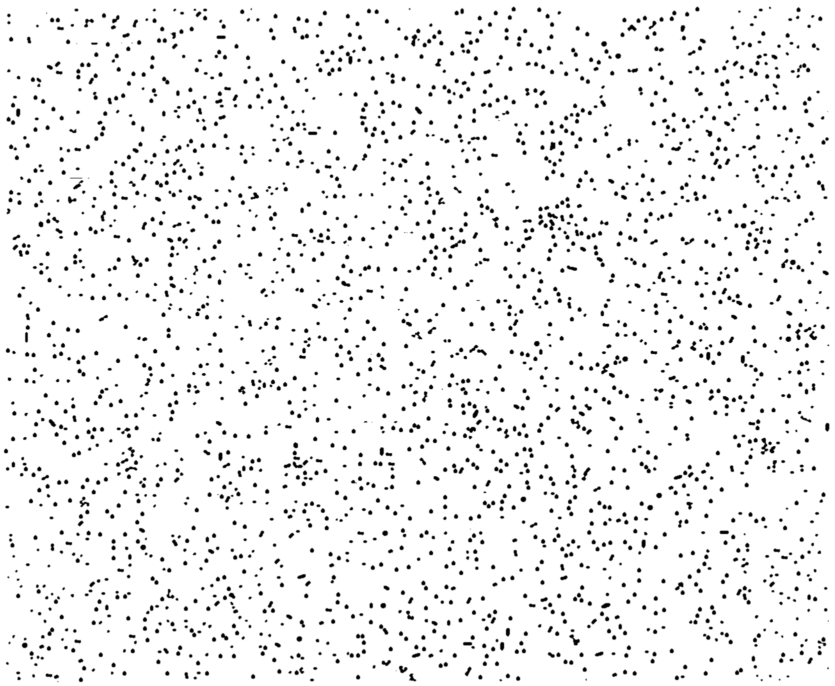

Figure 15h. X-ray image from two-dimensional mapping of uranium in plutonium for Sample 2 of the impurity alloy (2000X).

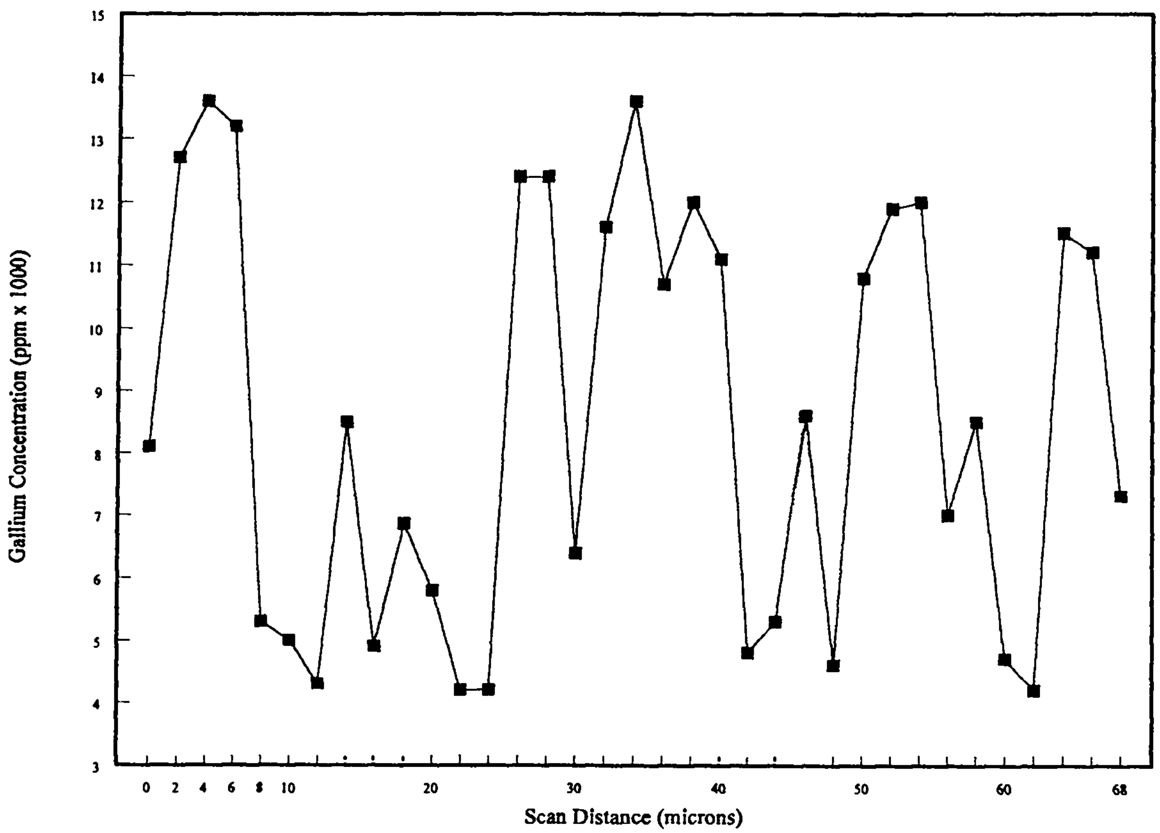

Figure 15i. Microprobe quantitative scan of Sample 2 of the impurity alloy for gallium.

TABLE 3: SEGREGATION OF IMPURITY ALLOY
Average Maximum and Minimum Microscopic Concentration in ppm by weight (3 sig. figs. max)

Element	Sample 1		Sample 2	
	Maximum	Minimum	Maximum	Minimum
Gallium	11,200	5,700	12,700	4,320
Aluminum	1,400	370	1,700	640
Americium	0	0	1,200	220
Cobalt	3,300	840	7,800	250
Copper	2,400	390	5,700	320
Chromium	1,300	210	3,600	260
Iron	2,300	390	4,800	290
Nickel	3,400	530	8,700	110
Neptunium	0	0	1,240	370
Uranium	2,800	610	3,800	740

segregation for the 10 elements in the impurity alloy of both samples. The average maximum and minimum microscopic composition across the grains for the two samples are shown in Table 3. Microprobe analysis was discussed briefly as a method for estimating effective distribution coefficients in section 2.1.5. on page 8. The microprobe data in Table 3 and the following equations from section 2.1.5. were used to calculate an approximate K_e, presented in Table 4.

$$K_e = 2C_o/C_{max} \quad \text{if } K<1 \tag{2a}$$

or

$$K_e = 2C_o/C_{min} \quad \text{if } K>1 \tag{2b}$$

Taking $C_o = 9900$ for gallium in impurity alloy Sample 1 and $C_{min} = 5700$ gives $K_e = 3.5$. These results are shown in the second and third columns of Table 4 for samples 1 and 2 taken from the impurity alloy. The fourth column in Table 4 gives K estimated from the binary phase diagrams. For a few elements, K_e from the Kristofova, Kuchar, and Wozniakova data (12) are given.

Comparing the two different K_e's (columns 2 and 3, Table 4) calculated from two different samples of the same alloy implies the microprobe method is not very consistent. However, in the four cases where K_e was determined by Kristofova, Kuchar, and Wozniakova (12) using experimental zone refining results, the microprobe method seems to give much better results than those obtained from the phase diagram method.

TABLE 4: DISTRIBUTION COEFFICIENTS OF IMPURITY ELEMENTS

	K_e (a)		K (b)	K_e (c)
Element	**Sample 1**	**Sample 2**		
Ga	3.5	4.0	1.4	
Al	6.0	3.6	1.4	
Am	(d)	10.4	19	
Co	0.67	0.28	0.2	0.8
Cu	0.92	0.39	0.3	
Cr	0.77	0.30	0.2	0.6
Fe	0.96	0.46	0.2	0.6
Ni	0.65	0.26	0.3	0.7
Np	(d)	1.6 (<1) (e)	0.8	
U	0.15	0.15	0.6	

(a) calculated from chemical analysis
(b) determined from phase diagrams
(c) from Kristofova, Kuchar, and Wozniakova data (12)
(d) Undefined, can't divide by 0
(e) K_e must be less than 1 for Np.

5.2. Zone Refining of the Gallium Alloy

5.2.1. Zone Refining Runs

As each pass of the two runs was made, Boat 1 at 1 in/h and Boat 2 at 2 in/h, there was little difference in appearance of the molten zone. On the first pass of each run, a visible molten zone width of about 1/2 in was clearly visible. Within this molten zone there was a large amount of turbulence of the molten metal was caused by the out-gassing of the plutonium metal. The average power to the coil was about 7 kW for the first pass. On the second pass of each run, the molten zone was not as clearly visible because the molten plutonium was not as turbulent due to reduced out-gassing. In addition, a thin oxide layer was forming that prevented the molten zone from forming at the rod surface. During subsequent passes, no turbulence could be observed, as the molten zone was difficult to discern visually in the molten zone. However, the molten zone could be partially discerned by measuring a temperate profile along the bar axis with the infrared pyrometer. The zone could also be seen by observing its color in near darkness. The average power to the coil was about 8 kW for passes 2 through 10. The gallium analytical chemistry results of samples taken after each of the first four passes of each run are shown in Table 5.

TABLE 5: RESULTS OF CHEMICAL ANALYSES ON RODS 1 AND 2
Gallium concentration in ppm by weight (3 sig. figs. max)

	Rod 1 (1 in/h)			Rod 2 (2 in/h)		
Pass	Head end	Middle	Tail end	Head end	Middle	Tail end
0	9,850	9,850	9,850	9,850	9,850	9,850
1	9,700	11,100	9,700	10,700	10,100	11,100
2	10,100	9,700	8,700	10,200	9,300	9,100
3	10,400	9,500	9,200	9,800	8,900	8,900
4	8,000	7,700	7,900	10,100	8,500	8,000

5.2.2. Examination of Drill Sample Results

The data in Table 5 are plotted in Figures 16a through c. The plots in Figures 16a and b indicate a general trend in the change in gallium concentration from the head end of the rod, where the concentration is the greatest, to the tail end, where it is the least. Exceptions to this trend are evident in pass 1 for both rods and in pass 4 for Rod 1. These anomalous results may represent transients in the zone melting process itself or in sampling errors. The latter may account in part for lower gallium concentration values at the head end and higher values at the tail end of the rods, since samples had to be taken about 1/4 in from each end to avoid damaging the tantalum boats. The anomalous results of pass 4 for rod may represent the end of the zone melting effect (gallium movements may stop after the fourth pass) with this experimental setup for plutonium as will be discussed below. Also, the plots in Figures 16a and b, denote a trend in the change in gallium concentration at the middle and tail end of the rod, where the concentration decreases with each pass. The only exception to this trend is evident in pass 3 for Rod 1.

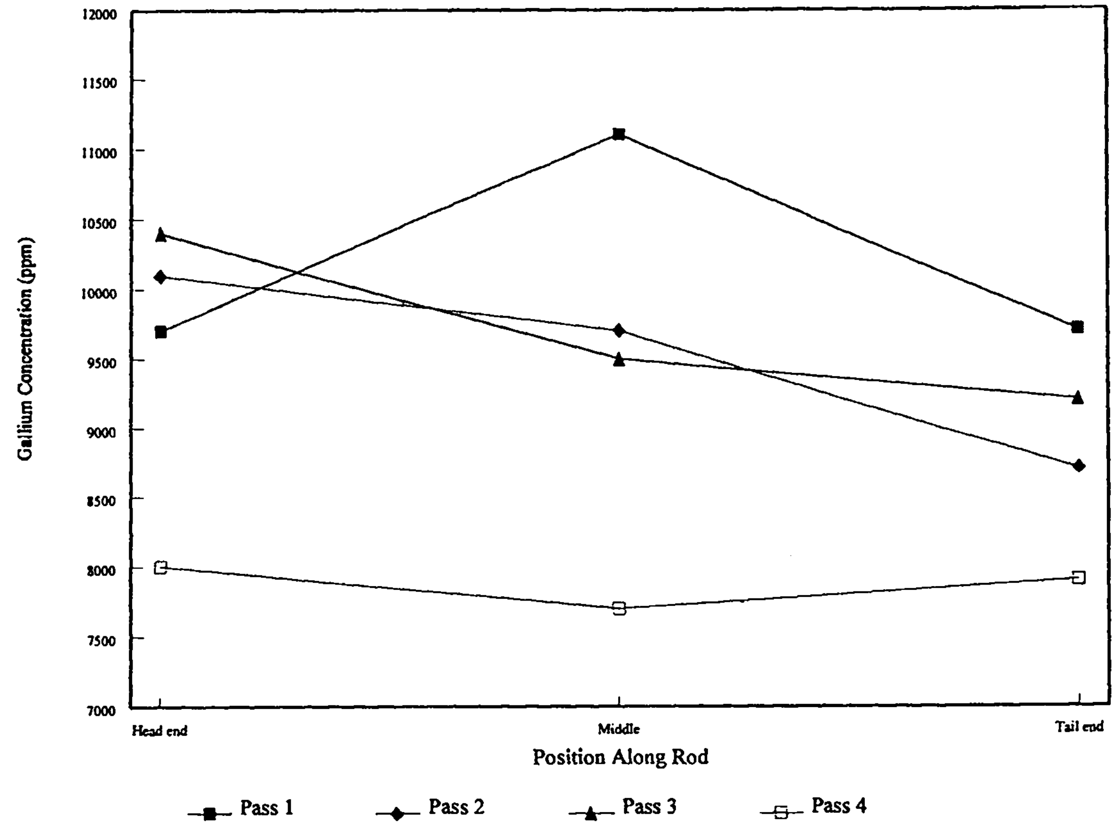

Figure 16a. Change in gallium concentration with position along Rod 1 for each pass (0, 1, 2, 3, or 4) at a molten zone speed of 1 in/h.

All the data in Table 5 are plotted in Figure 16c. From this plot, one can see the same trends as discussed above. Also, from Figure 16c, one can closely examine the effect of each pass on each rod position. After the first pass, the gallium concentration tended to increase for all rod positions, which disagrees with expectations based on the distribution coefficients for gallium. However, one possible explanation for this inconsistency is that gallium vaporizes up through the rod due to the high vapor pressure of gallium compared to plutonium. This possibility is supported by results that will be discussed below. After the

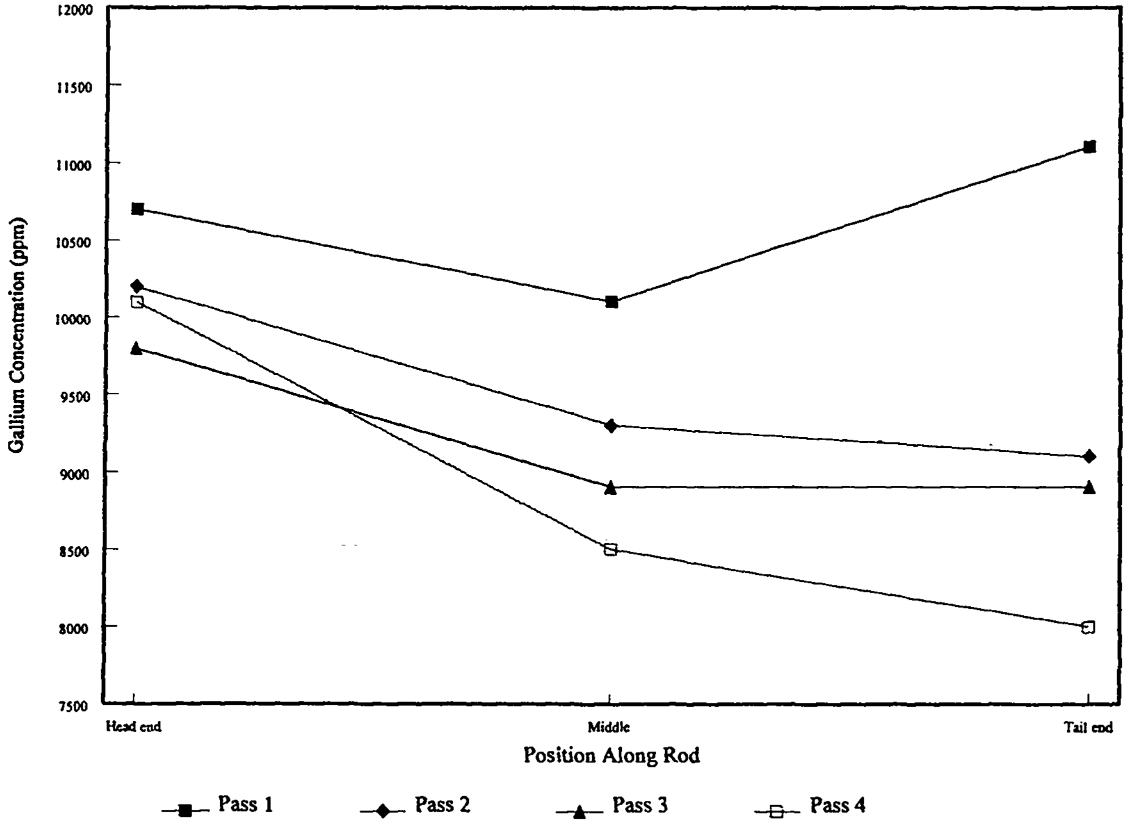

Figure 16b. Change in gallium concentration with position along Rod 2 for each pass (0, 1, 2, 3, or 4) at a molten zone speed of 2 in/h.

second pass, the gallium concentration dropped at all rod positions relative to pass 1 except the head end of Rod 1. This trend is expected based on the distribution coefficient for gallium. The trend after the third pass was about the same as the second pass. After the fourth pass, all data points agree with expectations based on the distribution coefficient for gallium except for the head end of Rod 1. But, this datum point could be affected by the sampling error already discussed above.

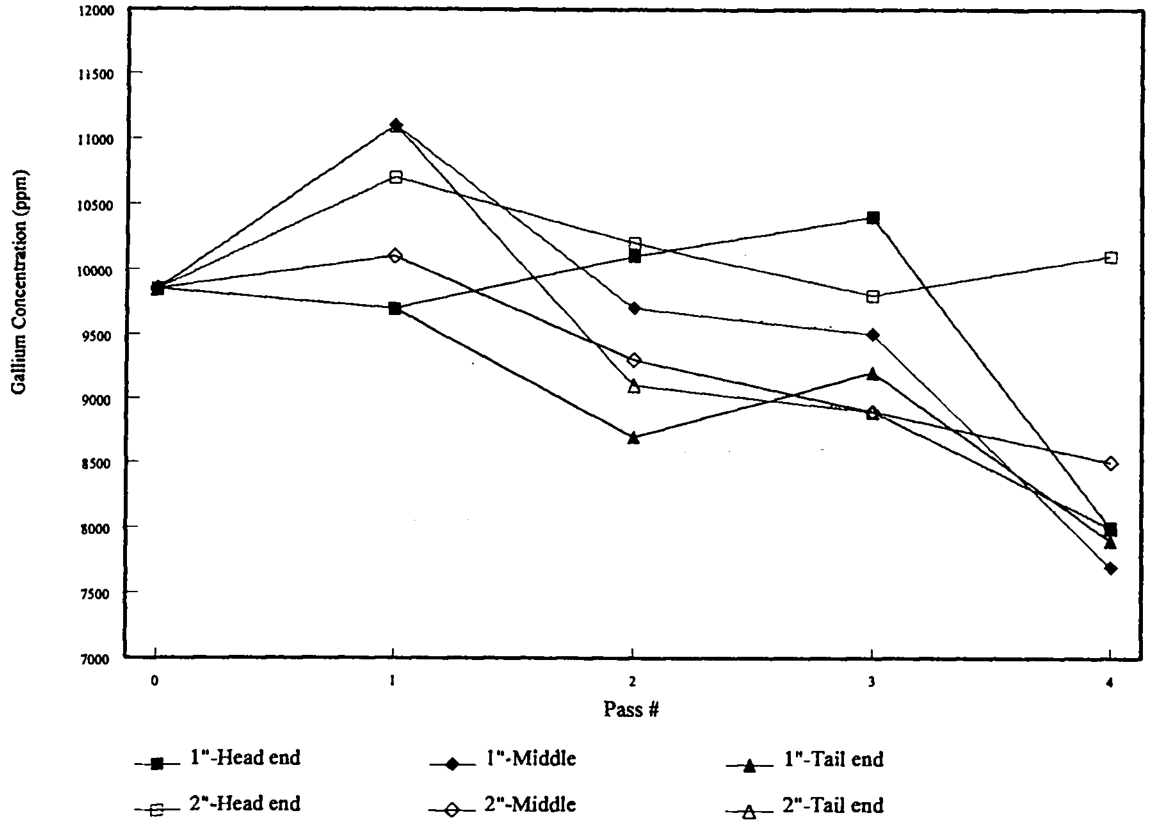

Figure 16c. Change in gallium concentration with each molten zone pass. Each data point corresponds to a pass (0, 1, 2, 3, or 4), a rod position (head end, middle, or tail end), and a molten zone speed (1 or 2 in/h). Pass 0 is the gallium concentration before any zone refining passes are made.

From Figures 16a through c, there appears to be no difference in the change in gallium concentration as a result of a lower molten zone speed. However, a molten zone speed of 1 in/h may be too great to permit the necessary mixing in the zone required to achieve the desired movement of the solute.

5.2.3. Analysis of Variance

An analysis of variance was performed using the data in Table 5 . It was an analysis of variance for a three-factor factorial experiment without replication, using three fixed effects. The fixed effects were: A, number of passes (1 through 4); B, molten zone speed (1 or 2 in/h); and C, sample position (head end, middle, or tail end). The results of running this analysis of variance using equations 5 through 8 and Table 1 in section 3.7.2 are shown in Table 6.

TABLE 6: ANALYSIS OF VARIANCE FOR GALLIUM ALLOY AFTER FIRST FOUR PASSES ON RODS 1 AND 2
(3 sig. figs. max)

Source	Sum of Squares (SS)	Degrees of Freedom (DF)	Mean Squares (MS) MS=SS/DF	F Value F= MS/MSABC
Main effects				
A, pass	12,476,667	3	4,158,888	13.09
B, speed	375,000	1	375,000	1.18
C, position	2,643,333	2	1,321,667	4.16
Interactions				
AB	1,828,333	3	609,444	1.92
AC	1,793,333	6	298,889	0.94
BC	970,000	2	485,000	1.53
ABC (error)	1,906,667	6	317,778	
Totals	21,993,333	23		

Since, there were no replications of any of the experiments, the error term is the ABC interaction term. For 3 degrees of freedom with an error term of 6 degrees of freedom requires an higher F value greater than 2.42 for the probability of no significance to be 0.25. From Table 6, one can see that there were no interactions between the fixed effects; all F values are below 2.42 (1.92, 0.94, 1.53). Since there were no interactions between the fixed effects, the analysis of variance was run again incorporating this fact. Results are shown in Table 7.

TABLE 7: ANALYSIS OF VARIANCE FOR GALLIUM ALLOY AFTER FIRST FOUR PASSES ON RODS 1 AND 2 (3 sig. figs. max)

Source	Sum of Squares (SS)	Degrees of Freedom (DF)	Mean Squares (MS) MS=SS/DF	F Value F= MS/MSABC
Main effects				
A, pass	12,476,667	3	4,158,888	10.88
B, speed	375,000	1	375,000	0.98
C, position	2,643,333	2	1,321,667	3.46
Error	6,498,333	17	382,254	
Totals	21,993,333	23		

The significance of the main effects is shown in Table 7. For the number of passes to be significant, with the degrees of freedom 3 and 17, the F value would have to be greater than 8.7 for the probability of no significance to be 0.001. Since the F value is well above this value (10.88), one can conclude that there are significant differences among the gallium concentrations with each molten zone pass. For the speed to be significant, given that the degrees of freedom are 1 and 17, the F value would have to be greater than 1.4 for the probability of no significance to be 0.25. Since the F value is below this value (0.98), one can not conclude that there are differences among the gallium concentrations with different molten zone speeds. For the sample position to be significant, given that the degrees of freedom are 2 and 17, the F value would have to be greater than 3.6 for the probability of no significance to be 0.05 or greater than 2.6 for the probability of no significance to be 0.1. Since the F value is 3.46, one can conclude that there are significant differences among the gallium concentrations at the different rod positions. Based on significant effects for number of passed and position, we can once again conclude that zone refining produces significant movement of gallium in plutonium.

5.2.4. X-ray Fluorescence Analyses

The x-ray fluorescence samples were machined after Rods 1 and 2 had each completed 10 molten zone passes (runs complete). During the machining of the x-ray fluorescence analysis samples from Rods 1 and 2, the machinists noted that the head end of each rod was ductile (malleable) and that the tail end of each rod was brittle when the machining cuts were made. This infers that delta-phase plutonium was present in the head end of each rod and that the .α-phase plutonium was present at the tail end of each rod. One can rationalize this phenomenon by assuming that gallium had moved in a direction opposite to the direction of motion of the molten zone, as predicted by the distribution coefficient for gallium.

The results of x-ray fluorescence analyses on the four samples from Rods 1 (1 in/h) and 2 (2 in/h) are shown in Table 8. The values are corrected for background readings. The last column again shows the trend that the change in gallium concentration is greater in the head end compared to the tail end of Rods 1 (30% greater) and 2 (28% greater). This trend can be seen in Figure 17, which is a plot of the data from columns 2 and 3 in Table 8. Table 8 and Figure 17 provide more evidence to conclude that gallium moved in a direction opposite to the direction of motion of the molten zone as predicted by the distribution coefficient for gallium, and that molten zone speed did not have an effect.

TABLE 8: RESULTS OF X-RAY FLUORESCENCE ON RODS 1 AND 2
Gallium intensity (counts per second)

Sample	Head end	Tail end	Head-tail change (%)
Rod 1,	43	30	-30%
1 in from end	41	33	
Rod 2	39	28	-28%
1 in from end	35	31	

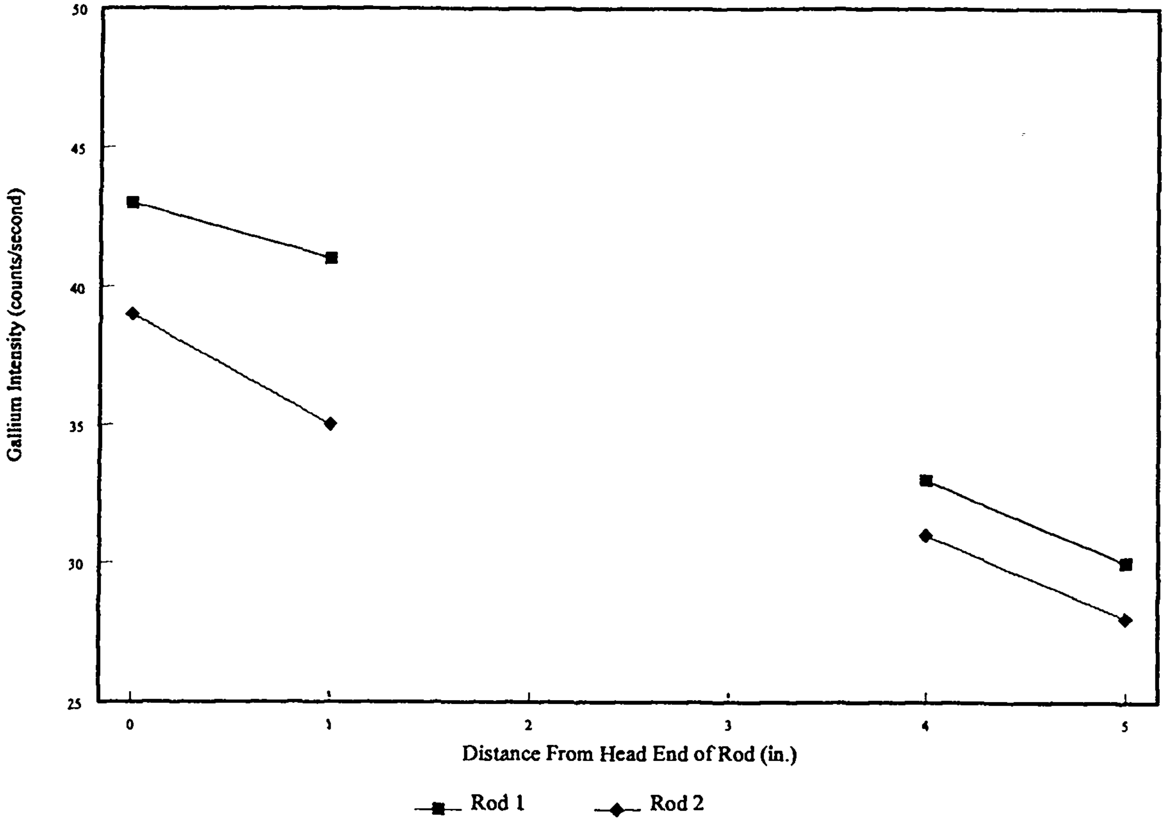

Figure 17. Results of x-ray fluorescence on Rods 1 and 2 (gallium alloy).

5.2.5. Metallographic Examination of X-Ray Fluorescence Samples

Metallographic examination of the zone refined gallium alloy rods revealed the commonly observed structure of as-cast plutonium with 10,000 ppm of gallium, a α-phase plutonium interspersed in δ-phase plutonium (19). Microstructure examples from the four samples taken from Rods 1 and 2 are shown in Figures 18 and 19. Figure 18a shows the head end of Rod 1 at a magnification of 10. From this figure, there appear to be large grains (approximately 2 mm in diameter). Figure 18b shows a portion of Figure 18a at a magnification of 50 where one can clearly see grain boundaries. Inside each grain in this figure are acicular cored plutonium grains with a average diameter of approximately 0.003 mm. These acicular grains appear as a classic Widmanstatten structure (4). Figure 18c then

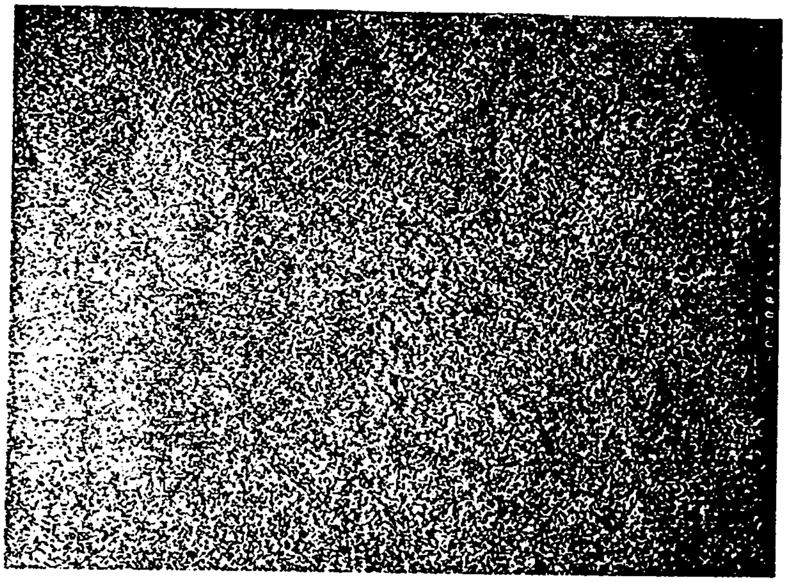

Figure 18a. Rod 1 microstructure at the head end of the rod (10X).

Figure 18b. Rod 1 microstructure at the head end of the rod (50X).

Figure 18c. Rod 1 microstructure at the head end of the rod (500X).

Figure 18d. Rod 1 microstructure at the tail end of the rod (250X).

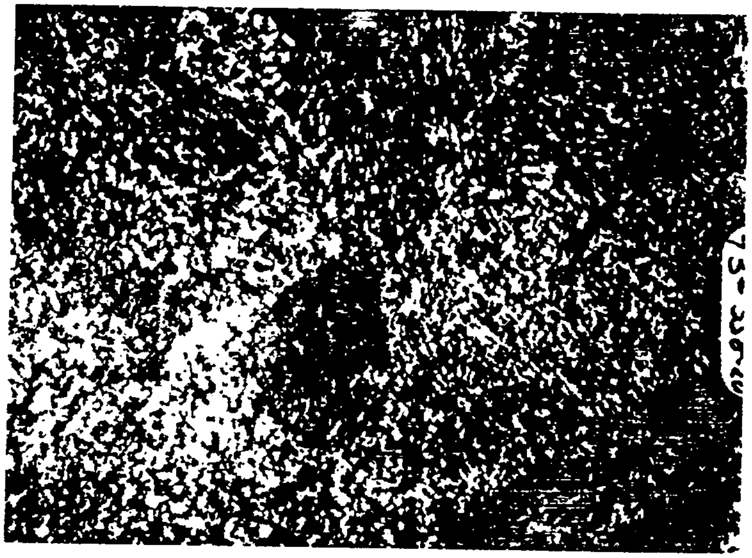

Figure 19a. Rod 2 microstructure at the head end of the rod (10X).

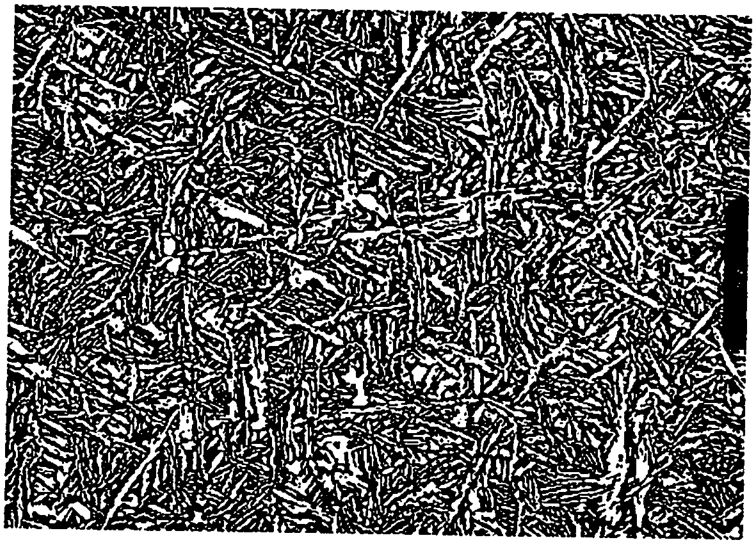

Figure 19b. Rod 2 microstructure at the head end of the rod (50X).

Figure 19c. Rod 2 microstructure at the head end of the rod (500X).

Figure 19d. Rod 2 microstructure at the tail end of the rod (200X).

shows a portion of Figure 18a at a magnification of 500. Figure 18c clearly shows the δ-phase plutonium (dark) and the small amount of α-phase plutonium (white). Figure 18d shows the tail end of Rod 1 at a magnification of 250. From this figure, one can see the microstructure is similar to that in Figure 18c except that the acicular grains are larger (approximately 0.007 mm in diameter). The same examination done with Rod 1 is done with Rod 2 (Figures 19a through d). From these figures, the only difference in microstructure between Rod 1 (1 in/h) and Rod 2 (2 in/h) was that the acicular cored grains were larger (approximate acicular grain diameter: 0.004 mm head end and 0.010 mm tail end).

To interpret the microstructures shown in Figures 18 and 19, one must examine them in terms of the gallium-plutonium phase diagram (Figure 7a, page 18). As this alloy solidifies in the $\varepsilon + l$ phase field and then cools through the ε-phase field, the large grains shown in Figures 18a and b are formed. The core of these ε-phase grains will have the highest gallium concentration (first to solidify) and the lowest gallium concentration at the grain edge (last to solidify) thus forming a cored ε-phase grain. The alloy then enters the $\varepsilon + \delta$ phase field, at which point the δ-phase begins to precipitate on preferred planes in the ε-phase forming the Widmanstatten structure seen in Figure 18b. The core (first to form) of these δ-phase grains will have the highest gallium concentration because the higher the gallium concentration the higher the temperature at which the δ-phase is reached on cooling (Figure 7a). As this alloy cools further, it enters the δ phase field where the last ε-phase is low in gallium. These gallium-poor areas form α-phase upon cooling to ambient temperature, as seen by the white areas in Figures 18 and 19. The fact that α-and δ-phases are both present in Figures 18 and 19 is proven by x-ray diffraction discussed below.

5.2.6. Final Analysis of Rods 1 and 2

Table 9 shows the results of the chemical analyses for gallium and americium on Rods 1 and 2, after 10 passes along with initial values from Table 2, and values after 4 passes from table 5. The most striking information from Table 9 is that it appears there was little movement of gallium during zone refining passes 5 through 10 on Rods 1 and 2. This lack of movement could possibly be tied to the oxide layer formation that occurred with each molten zone pass. Bieber, Schreyer, and Williams (9) discovered that during the zone refining of uranium metal the formation of a uranium oxide layer had a strong negative effect. Since plutonium metal forms an oxide layer more easily than uranium metal, it is possible that a plutonium oxide layer would have a negative effect on plutonium zone refining. One possible reason for the oxide layer slowing down the zone refining effect is that the oxide layer prevent out-gassing, which greatly decreases the amount of stirring in the molten zone. Table 9 also shows the trend that gallium moved in the predicted direction according to the distribution coefficient. Furthermore, Table 9 shows that americium moved towards the head end of the rod as expected on the basis of the distribution coefficient for the plutonium-americium system. Table 9 gives the first indication that the slower the zone refining speed the better segregation obtained. The low americium values are the result of americium vaporizing from molten plutonium under vacuum conditions.

TABLE 9: CHEMICAL ANALYSIS OF RODS 1 AND 2
Concentration in ppm by weight (3 sig. figs. max)

Rod and impurity	As-cast	Head end (4 passes)	Tail end (4 passes)	Head end (10 passes)	Tail end (10 passes)
Rod 1, Ga	9,940	8,000	7,900	10,200	7,200
Rod 1, Am	710			487	371
Rod 2, Ga	9,940	10,100	8,000	8,500	8,100
Rod 2, Am	710			415	394

Rod 1 (1 in/h)
Rod 2 (2 in/h)

Results of x-ray diffraction analysis on the sample from Rod 1 revealed the presence of a small amount of α-phase in δ-phase.

The microprobe quantitative scans of the sample from Rod 1 were about the same at both the center and edge of the sample. Figure 20 shows the quantitative scan for the center of the sample. The figure also shows that the plutonium α-phase was present (low gallium concentration) and the gallium segregation (coring). The peaks in Figure 20 correspond to the center of the acicular grains shown in Figures 18 and 19. The valleys in Figure 20 correspond to the white α-phase areas on the acicular grain edges shown in Figures 18 and 19.

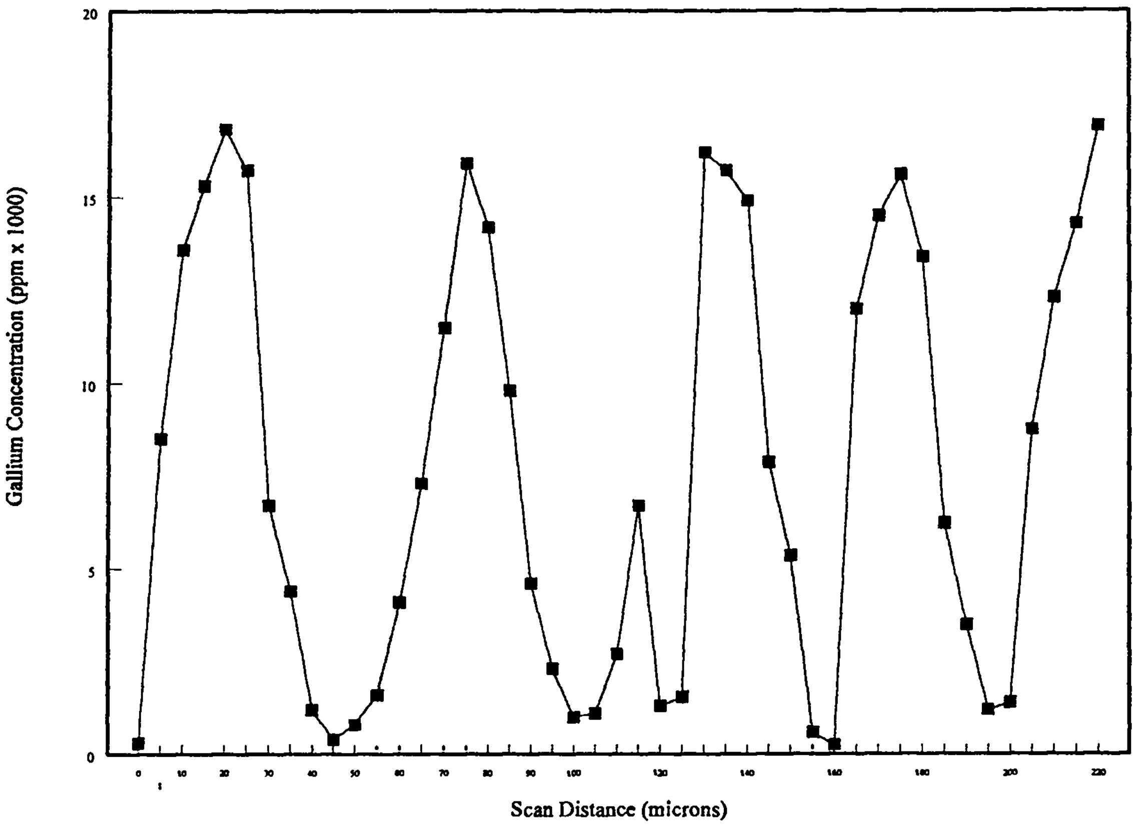

Figure 20. Microprobe quantitative scan of sample from Rod 1 for gallium.

5.3. Zone Refining of the Impurity Alloy

5.3.1. Zone Refining Runs

Boats A, B, C, and D loaded with the impurity alloy were zone refined (10 molten zone passes per boat per run) in the same way as Boats 1 and 2, except Boats C and D were zone refined using constant voltage to the coil. As was also observed during the zone refining of the gallium alloy (section 5.2.1.), turbulence in the molten zone was caused by the out-gassing of the plutonium metal. Two differences between these runs and the runs with the gallium alloy were observed. First, Boats C and D had a wider molten zone (approximately 3/4 in instead of 1/2 in) than Boats 1, 2, A, and B during the first pass of each run. Second, when the first pass was completed for each run (Boats A, B, C, and D), a crystalline layer had formed on the top surface of the rods. Evidence for this crystalline layer was the appearance of crystalline facets (below the oxide layer) approximately 1.0 mm x 0.5 mm can be seen in Figures 21 and 22. This crystalline layer was more clearly defined at the head end of the boats that were run at 2 in/h (Boats B and D) than those run at 1 in/h (Boats A and C). On the second pass of each run, the molten zone was not as clearly defined because the molten plutonium was not as turbulent. The crystalline layer became larger and was capped by a thin skull layer. Little out-gassing was observed in the molten zone in this and subsequent passes. The crystals appeared to grow larger, especially at the front of the boat.

Figure 21 shows plutonium Rods A and C after they were removed from their tantalum boats. Figures 22a though c show magnified views of the top surface area of Rod B, after it was removed from its boat. Rod B contained the largest crystals observed; they were located at the rod's head end (Figure 22a).

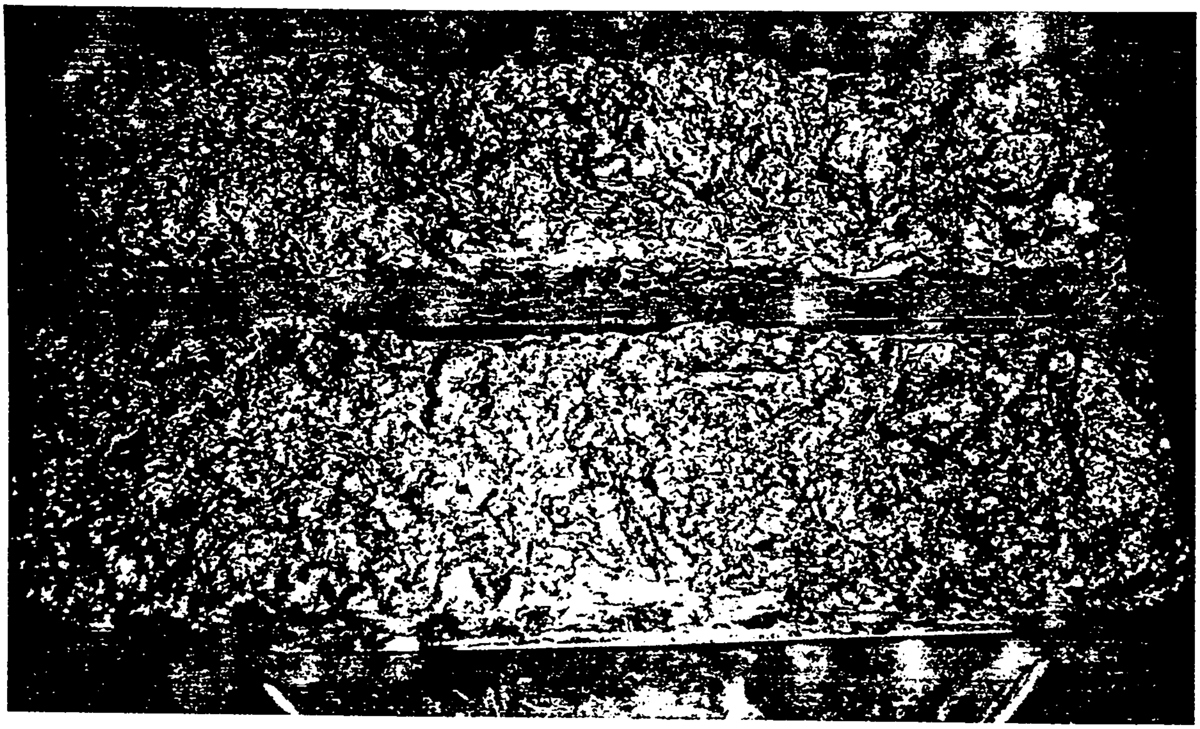

Figure 21. Zone refined plutonium Rods A (bottom) and C (top).

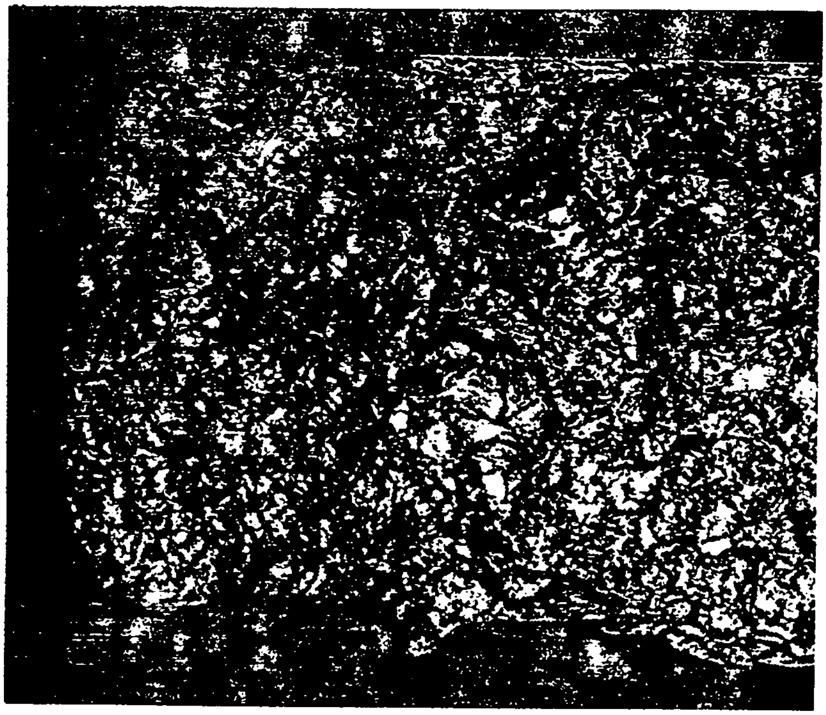

Figure 22a. Head end section of zone refined plutonium metal Rod B.

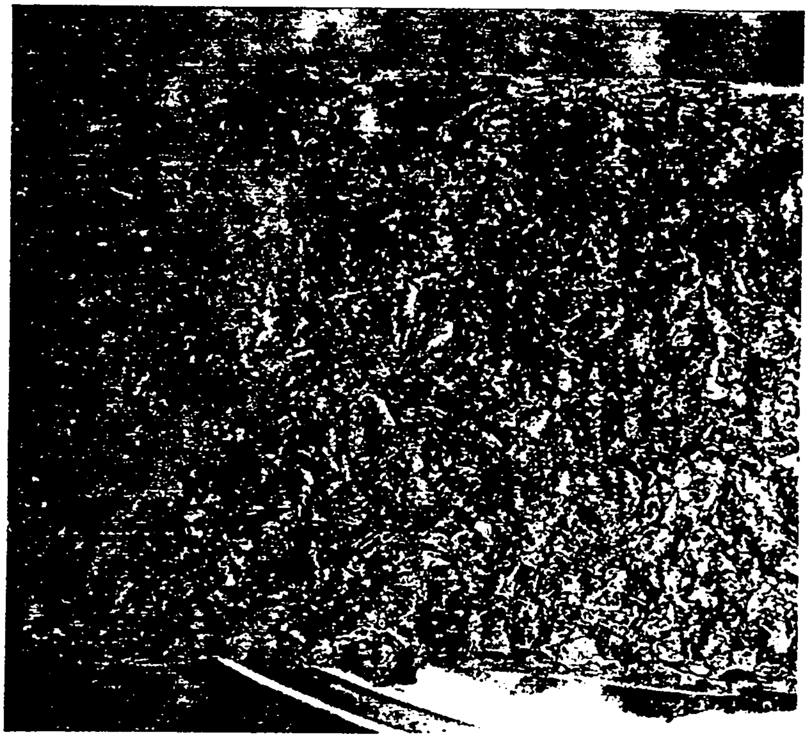

Figure 22b. Middle section of zone refined plutonium metal Rod B.

Figure 22c. Tail end section of zone refined plutonium metal Rod B.

5.3.2. X-Ray Fluorescence Analyses

When the x-ray fluorescence samples were machined from Rods A through D, they were also malleable at the head end and brittle at the tail end. This again infers that δ-phase plutonium was present in the head end of each rod and α-phase plutonium was present in the tail end of each rod, leading to the conclusion that gallium had moved in the opposite direction to the molten zone as predicted by the distribution coefficient for the plutonium-gallium system.

Although the x-ray fluorescence samples were prepared, x-ray fluorescence analyses were not done because of complications in operating the x-ray fluorescence equipment.

5.3.3. Metallographic Examination of X-Ray Fluorescence Analysis Samples

The metallographic examination of the samples taken from impurity alloy Rod A revealed more heterogeneous microstructures than the samples from Rods 1 and 2. Figures 23a through d show some of the plutonium microstructures from Rod A (1 in/h). Metallographic examination of the Rod A samples revealed α-phase plutonium in δ-phase plutonium (acicular cored plutonium grains), which was a fine structure in the rod center and a coarse structure at the rod edge (Figure 23a and b). This structure became coarser from the head end to the tail end of the rod (Figure 23c and d). In general, the acicular cored plutonium grains in Rod A were less acicular than the ones in Rods 1 and 2 (compare Figures 18d and 19d to 22d). What appears to be impurities can be seen at the acicular grain boundaries (Figure 23c and d).

Figure 23a. Rod A microstructure at the head end (center) of the rod (50X).

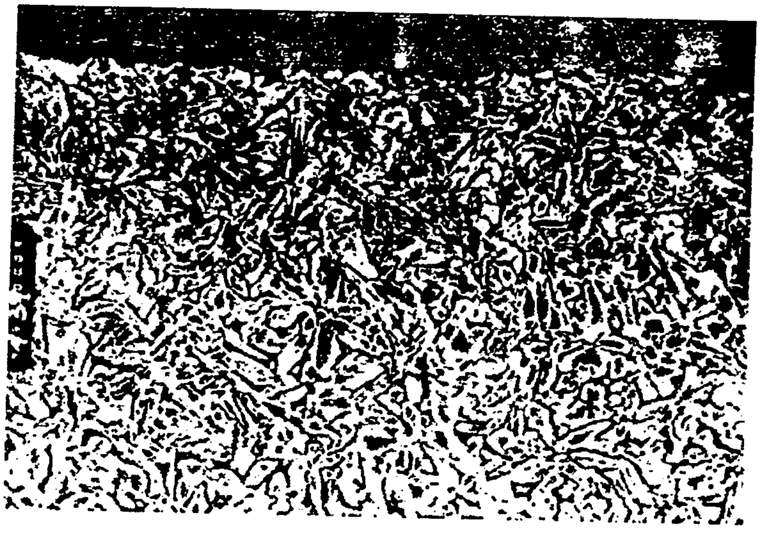

Figure 23b. Rod A microstructure at the head end (edge) of the rod (50X).

Figure 23c. Rod A microstructure at the head end of the rod (500X).

Figure 23d. Rod A microstructure at the tail end of the rod (250X).

5.3.4. Chemical Analysis of Rods A-D

Table 10 shows the results of the chemical analyses on Rods A through D after each run was complete (10 molten zone passes made along each rod). In Table 10, the first row for each rod gives the as-cast concentration or calculated average as-cast concentration from Table 2 (columns 2, 3 and 4, respectively) for each impurity element. The second and third rows for each rod give the head end and tail end concentration for each impurity, respectively. The fourth row for each rod gives the head end to tail end change in concentration for each impurity. The last row for each rod (row 5) gives a crude approximation of the loss due to some vaporization mechanism of impurity element concentration. Row 5 for each rod is calculated from the change in the average impurity concentration (average of the head and tail end concentrations) and the as-cast concentration (row 1) for each impurity.

Row 4 contains the most important data for determining the main objective of this project, namely to demonstrate that plutonium metal can be zone refined. The direction that each impurity moved in each rod can be seen by examining the data in this row. A positive per cent change indicates the impurity moved in the direction of molten zone travel; a negative per cent change indicates the reverse.

From an examination of the results for uranium, Rods A, B, and C (six samples), it is clear that this element moved in the same direction as the molten zone. The amount of uranium in Rod D was below the detectable limit in both the head end and tail end samples. Except for the anomalous results for uranium in Rod D and copper in Rod C, all the impurities listed in Table 10 moved in the direction predicted by their respective distribution coefficients.

TABLE 10: RESULTS OF CHEMICAL ANALYSIS OF RODS A, B, C, D
Concentration in ppm by weight (3 sig. figs. max)

Rod		Element Concentration									
		Ga	Al	Am	Co	Cu	Cr	Fe	Ni	Np	U
A	**As-cast**	9,850	1,120	2,074	1,095	1,105	520	1,100	1,120	962	248
	Head end	9,100	503	1,466	100	700	230	510	650	825	50
	Tail end	7,110	456	1,246	230	760	480	1,050	1,220	863	430
	% change										
	Head-tail	-22	-9	-15	130	9	109	106	88	5	760
	Loss	-18	-57	-35	-85	-34	-32	-29	-17	-12	-3
B	**As-cast**	9,850	1,120	2,074	1,095	1,105	520	1,100	1,120	962	248
	Head end	8,590	462	1,499	110	640	75	365	620	770	<5
	Tail end	7,360	387	1,463	240	820	500	1,140	1,280	857	30
	% change										
	Head-tail	-14	-16	-2.4	118	28	567	212	107	11	500
	Loss	-19	-62	-29	-84	-34	-45	-32	-15	-15	-93
C	**As-cast**	9,850	1,120	2,074	1,095	1,105	520	1,100	1,120	962	248
	Head end	8,800	448	1,550	80	610	180	360	520	775	<5
	Tail end	5,440	374	1,260	170	600	290	590	840	898	90
	% change										
	Head-tail	-38	-17	-19	113	-2	61	64	62	16	1700
	Loss	-28	-63	-32	-89	-45	-55	-57	-39	-13	-81
D	**As-cast**	9,850	1,120	2,074	1,095	1,105	520	1,100	1,120	962	248
	Head end	9,610	441	1,600	1,200	580	140	270	420	829	<5
	Tail end	6,750	372	1,200	60	690	186	880	1,120	966	<5
	% change										
	Head-tail	-30	-16	-25	250	19	186	226	167	17	
	Loss	-17	-64	-33	-88	-43	-43	-48	-31	-7	-98

Upon examination of the data in Table 10, there appears to be a mass balance problem because ideally the loss of each impurity (row 5) should be approximately zero. However, using the average of the head end and tail end concentrations as an approximation of the average impurity concentration of the rod may be a very poor approximation, depending on factors such as impurity distribution coefficients, impurity solubility, etc. The problem of using this approximation for the average impurity of the rod can be seen by examining Figure

6. From Figure 6, the average of the head end and tail end deviates further from the bulk concentration as the number of passes are increased. Furthermore, the distribution coefficient of 0.9524 causes very little impurity movement compared to the distribution coefficients of most of the impurities examined. Assuming the losses are true losses (given the small amount of data, only two points per rod), one can assume from Table 10 that a certain amount of each impurity element was lost through one or more different vaporization mechanisms.

5.3.5. Analysis of Variance

An analysis of variance was performed using the data in Table 10 for each impurity element for a three-factor factorial experiment without replication using fixed effects and assuming no interaction between the effects. The fixed effects were power setting (constant or variable); molten zone speed (1 or 2 in/h); and sample location (head end or tail end). This gave each effect 1 degree of freedom with an error term having 4 degrees of freedom.

The results of this analysis using equations 5 through 8 and Table 1 in section 3.7.2. are shown in Table 11. In this case, an F value greater than 8.85 is needed for the probability of no significance to be less than 0.25. Molten zone speed appears to have the least significance of the three effects, an unexpected result. Usually, when a material is zone refined, the effectiveness of zone refining in redistributing solute increases with the lower the molten zone speed. The results obtained by Tate and Anderson (2) showed that decreasing the molten zone speed increased the zone refining effectiveness. In this experiment, the effect of molten zone speed could have been reduced as a result of oxide layer. As already speculated, the oxide layer stops the out-gassing of the molten zone which then reduces the amount of stirring in the molten zone. From the F values calculated for the significance of whether the power to the coil was constant or continuously varied did not have much

TABLE 11: ANALYSES OF VARIANCE FOR IMPURITY ALLOY AFTER TEN PASSES ON RODS A, B, C, AND D FOR EACH IMPURITY ELEMENT
Calculated F values

Elements	Effects: Power	Speed	Position
Ga	0.60	0.85	21.8
Al	9.8	4.6	22.9
Am	0.05	0.66	10.3
Co	13.5	0.84	131.6
Cu	9.6	0.18	5.7
Cr	1.3	0.07	18.1
Fe	5.4	0.12	26.9
Ni	8.2	0.48	54.5
Np	1.7	0.26	10.4
U	1.4	2.3	1.9

An F value of greater than 8.58 gives a probability of no significance to be 0.25.
An F value of greater than 55.83 gives a probability of no significance to be 0.10.

significance as shown in the second column of Table 11. As can be seen in the last column in Table 11, there was significance for position for most impurity elements. This means there was consistent movement of the atoms in each rod for impurities other than uranium and copper.

5.4. Gallium Behavior With and Without Impurities Present

The effectiveness of zone melting in redistributing gallium cannot be determined from the results of this work. Table 12 contains the results of chemical analysis for gallium of Rods 1 and 2 (gallium alloy) and Rods A and B (impurity alloy). These results are too scattered to make any inferences concerning the effects of impurities on the behavior of gallium in zone refining.

5.5. X-Ray Analysis of Rod A

X-ray diffraction analysis of the sample taken from Rod A indicate that the sample contained mostly δ-phase plutonium with some α-phase plutonium. This result compares favorably with the results of x-ray analysis of Rod 1 (section 5.2.6.). Based on the x-ray diffraction analysis of the rod A sample, the plutonium crystals are δ-phase.

TABLE 12: RESULTS OF GALLIUM CHEMICAL ANALYSIS OF RODS 1, 2, A, AND B
Concentration in ppm by weight, taken from Tables 9 and 10
(3 sig. figs. max)

Rod # & speed	Rod front	Rod end	% change
Rod 1, 1 in/h	8,500	8,100	-5
Rod 2, 2 in/h	10,200	7,200	-29
Rod A, 1 in/h	9,100	7,110	-22
Rod B, 2 in/h	8,590	7,360	-14

5.6. Microprobe Analysis of Rod A

The results of microprobe quantitative scans of the sample from rod A are shown in Figures 24a and b. From Figures 24a (sample edge) and b (sample center), there is a visible difference with the larger cored acicular grains (Figure 24a). Figures 24a and b also show that the plutonium α-phase was present (low gallium concentration) and that there was gallium segregation. The peaks in Figures 24a and b correspond to the center of the acicular grains shown in Figures 23c and d. The valleys in Figures 24a and b correspond to the white α-phase areas on the acicular grain edges shown in Figures 23c and d.

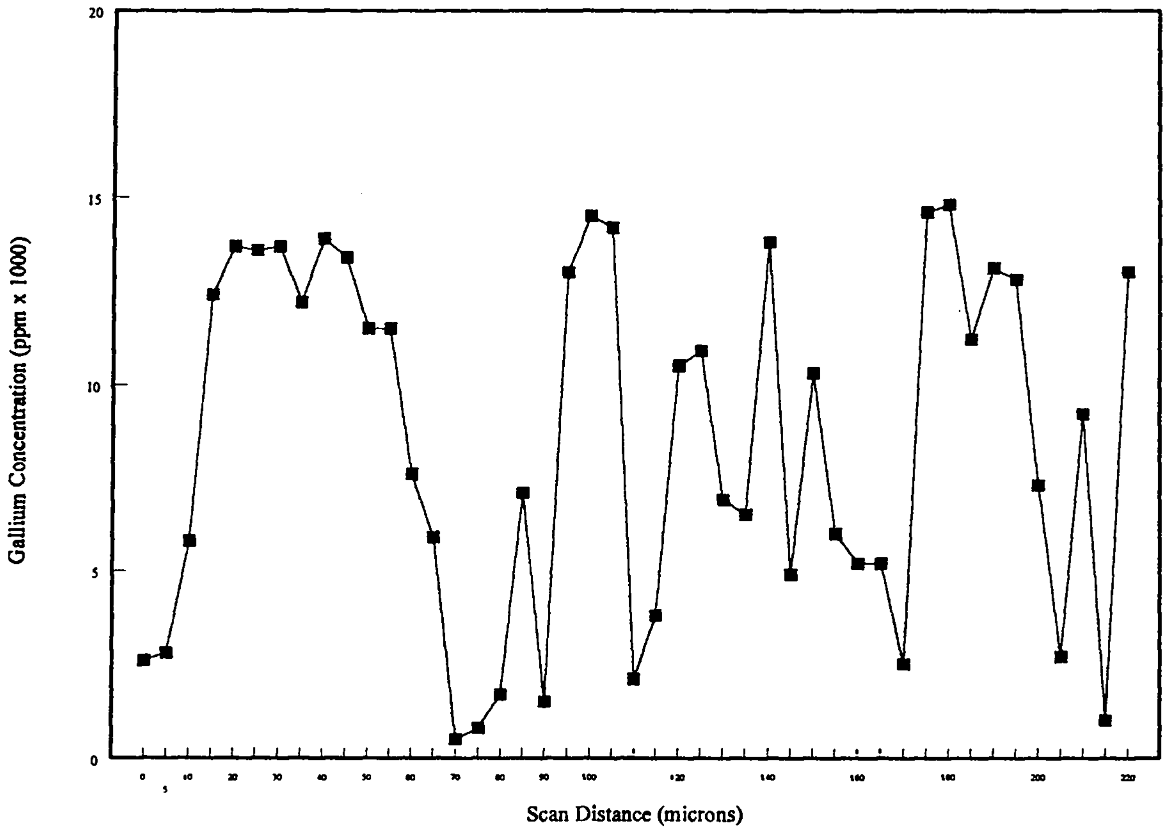

Figure 24a. Microprobe quantitative scan of sample from Rod A (edge) for gallium.

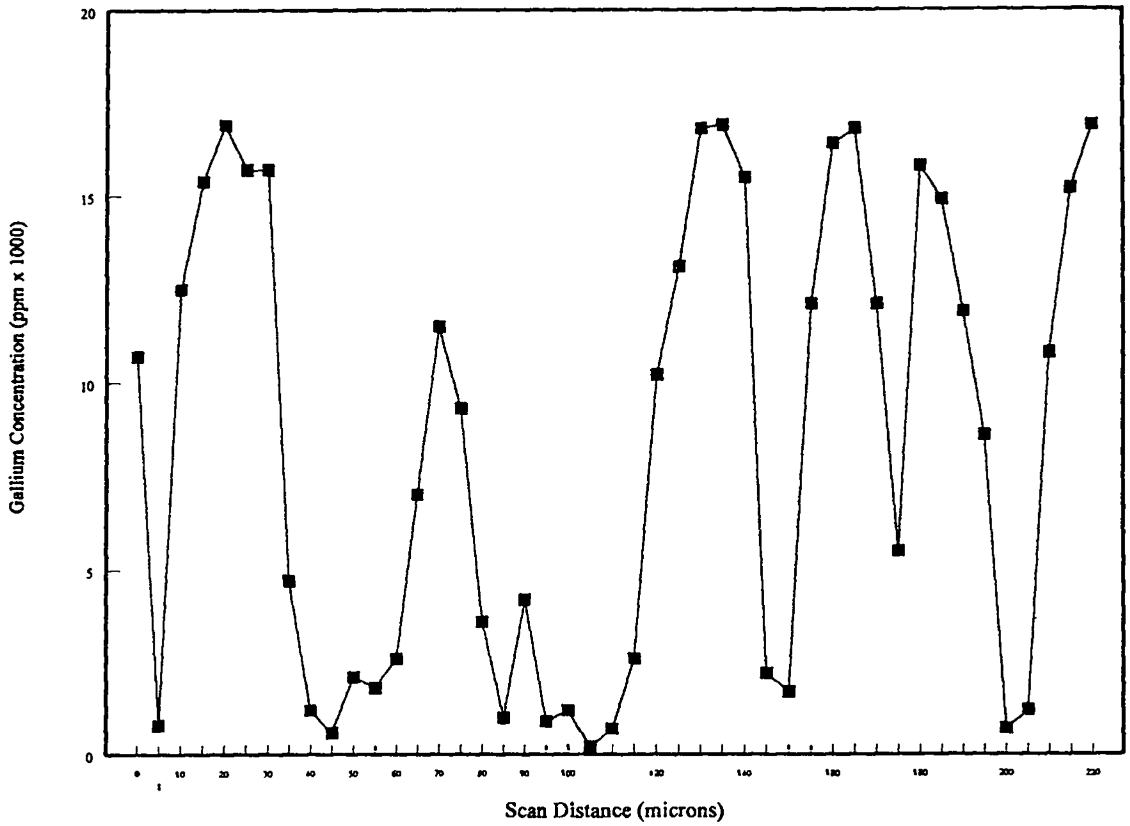

Figure 24b. Microprobe quantitative scan of sample from Rod A (center) for gallium.

5.7. Distribution Coefficients and Zone Refining Results

In section 5.1, the effective distribution coefficients for the impurity elements were calculated using the microprobe technique. Table 13 lists the average K_e and the average impurity per cent change from head end to tail end for each rod calculated from the values given in Table 4 and 10 respectively. Table 13 is divided into two parts, impurity elements with a $K > 1$ and $K < 1$. The impurity elements are listed in decreasing zone refining efficiency (amount of impurity movement according to theory) based upon the calculated K_e. Zone refining theory of impurities predicts the largest changes will occur in impurities with K most different than 1 as long as there are no interactions between the impurities. For the elements with $K > 1$, the zone refining results and K_e do not follow this trend. In the case of elements with a $K < 1$, the zone refining results do have some correlation. The best example of this is with uranium and neptunium. However, the point must be raised that the use of distribution coefficients for the prediction of how well impurities will move in plutonium is based on the assumption that each impurity behaves completely independently of the other impurities present. This assumption for plutonium probably does not work well given the unique phase properties of plutonium.

Table 13: DISTRIBUTION COEFFICIENTS AND ZONE REFINING RESULTS

Impurity element	Ave. K_e (Table 4)	% change (head-tail, Table 10)
Am	10	-15.4
Al	5	-14.5
Ga	4	-26.0
U	0.15	987
Ni	0.46	106
Co	0.48	153
Cr	0.54	231
Cu	0.66	13.5
Fe	0.71	152
Np	0.99	12.3

CHAPTER 6

SUMMARY AND CONCLUDING REMARKS

This study shows that after 10 passes of a molten zone in a zone refining operation through a bar of plutonium metal, moderate movement of certain elements was achieved. Cobalt, copper, chromium, iron, nickel, neptunium, and uranium moved in the direction of zone travel. Aluminum, americium, and gallium moved in the opposite direction. These results are in accord with anticipated element movement based on the distribution coefficient determined from the binary phase diagram of each element, with plutonium.

Although systematic analysis of the full length of each bar was not feasible so that a complete mass balance could be carried out, there is indication that vaporization of the impurities may have occurred. All experimental work was carried out in vacuum.

Alloys containing 10 impurities exhibited facets on their surfaces exposed to the vacuum chamber atmosphere. Metallographic examination below the surface revealed large grains. X-ray diffraction analysis proved the large grains to be δ-phase plutonium. The cause of the formation of these facets has not been demonstrated, but is assumed related to the presence of one or more of the impurities and to solidification in the zone melting process.

The movement of gallium seems to be unaffected by the presence of other impurities although this was not conclusively demonstrated.

The microstructures observed after zone melting of both alloys were in most part acicular grains of δ-plutonium and α-plutonium. This structure appears the be the classic Widmanstatten structure.

Molten zone speeds of 1 or 2 in/h had no effect on impurity element movement. Likewise, applying constant or variable (continuously adjusted manually) power to the coil had no effect on the movement of the impurities.

This study has demonstrated that zone melting caused redistribution of the 10 impurity elements investigated and implies that development of a zone refining process to purify plutonium is feasible. Development of a purification process will be hampered by two factors. First, the effect on impurity element redistribution of the oxide layer that formed on the exposed surface of the study material, and its relation, if any, to the underlying plutonium metal grain structure is not understood. Second, the tantalum container material is not inert in the presence of plutonium.

To alleviate the latter and possibly the former, another study will be carried out. In place of the tantalum boat, a so-called "cold" boat will be used to contain the plutonium metal. The cold boat is made from copper and gold, and is water cooled. The cold boat is designed to provide a levitation force to the plutonium metal. The levitation force serves to suspend the hot and molten material so that it will not come into contact with the cold boat. Because the boat is cold, any molten material that contacts the boat surface solidifies before it can react with the boat surface.

An additional advantage of using the cold boat is that it permits higher temperatures to be used in the material being purified. Higher temperatures in the molten zone will result in greater mixing and greater release of impurities by vaporization. It may also affect the formation of the skin on the exposed surface of the test material. Higher vacuum levels are desirable for the next study.

REFERENCES

1. Plutonium Handbook, A Guide to the Technology, O. J. Wick, ed., Gordon and Breach, New York, NY, 1967.

2. R. E. Tate and R. W. Anderson, Some Experiments in Zone Refining Plutonium, Los Alamos National Laboratory, Los Alamos NM, 1958.

3. W. G. Pfann, Zone Melting, Robert E. Krieger Publishing Company, Huntington, NY, 1978.

4. J. D. Verhoeven, Fundamentals of Physical Metallurgy, John Wiley & Sons, New York, NY, 1975

5. D. A. Porter and K. E. Easterling, Phase Transformations in Metals and Alloys, Van Nostrand Reinhold (UK) Co. Ltd., 1981.

6. J. A. Self, Effects of Composition Upon the Martensite Transformation Temperature of Austenitic Steel Welds, T-3144, Colorado School of Mines, Boulder, CO, 1987.

7. S. L. Semiatin and D. E. Stutz, Induction Heat Treatment of Steel, American Society for Metals, Metals Park, OH, Carnes Publication Services, Inc., 1986.

8. C. A. Tudbury, Basics of Induction Heating, vol. 1, Forging Industries Association, Cleveland, OH, 1960.

9. J. L. Bieber, J. M. Schreyer, and E. L. Williams, Purification of Uranium by Zone-Refining Techniques, Y-1564, Oak Ridge National Laboratory, Oak Ridge, TN, 1967.

10. K. Suzuki, T. Shikama, and A. Ochiai, Purification of Uranium Metal, Physical Properties of Actinde and Rare Earth Compounds, JJAP Series 8 (1993), pp15-19.

11. V. G. Kas'yanov and P. E. Gajvoronskii, Crucibleless Zone Melting of Uranium, Radiokhimiya, Vol. 23:1, 1981, pp 135-138.

12. D. Kristofova, L. Kuchar, and B. Wozniakova, Effective Distribution Coefficients of Admixtures in Plutonium, SB VER PR VYS Banske Ostrave Rada Hutn, Vol. 26, 1980.

13. T. B. Massalski, chief ed., H. Okamoto, P. R. Subramanian, and L. Kacprzak, ed. Binary Alloy Phase Diagrams, ASM International, 1990.

14. J. D. Olivas and F. W. Schonfeld, A Survey of Metallurgical Research on Several Actinides, LA-UR-93-3628, Los Alamos National Laboratory, Los Alamos, NM, 1993.

15. R. Madera, Correspondence with Fluxtrol Manufacturing, Inc., on plutonium zone refining, 4/7/93.

16. T. B. Barker, Quality by Experimental Design, Marcel Dekker, Rochester, NY, 1985.

17. L. Ott, An Introduction to Statistical Methods and Data Analysis, 3rd. Ed., PWS-Kent, 1988.

18. C. J. Martell and J. M. Hansel, Determining Gallium from Plutonium Using Anion Exchange and X-Ray Fluorescence, LA-11435, Los Alamos National Laboratory, Los Alamos, NM, 1988.

19. E. M. Cramer and J. B. Bergin, Plutonium Microstructures Part 2, UCRL-53174-2, Lawrence Livermore National Laboratory, Livermore, CA, 1983.